



Time and Frequency Resolved Pump Probe Spectroscopy and Growth of Near Surface Quantum Confined Semiconductors Coupled to Metallic Nanostructures

Item type	text; Electronic Dissertation
Authors	Olitzky, Joshua D.
Publisher	The University of Arizona.
Rights	Copyright © is held by the author. Digital access to this material is made possible by the University Libraries, University of Arizona. Further transmission, reproduction or presentation (such as public display or performance) of protected items is prohibited except with permission of the author.
Downloaded	6-Apr-2016 19:47:51
Link to item	http://hdl.handle.net/10150/595980

TIME AND FREQUENCY RESOLVED PUMP PROBE SPECTROSCOPY AND GROWTH
OF NEAR SURFACE QUANTUM CONFINED SEMICONDUCTORS COUPLED TO
METALLIC NANOSTRUCTURES.

by

Joshua D. Olitzky

A Dissertation Submitted to the Faculty of the

DEPARTMENT OF OPTICAL SCIENCES

In Partial Fulfillment of the Requirements

For the Degree of

DOCTOR OF PHILOSOPHY

In the Graduate College

THE UNIVERSITY OF ARIZONA

2016

THE UNIVERSITY OF ARIZONA
GRADUATE COLLEGE

As members of the Dissertation Committee, we certify that we have read the dissertation prepared by Joshua D. Olitzky, titled *Time and Frequency Resolved Pump Probe Spectroscopy and Growth of Near Surface Quantum Confined Semiconductors Coupled to Metallic Nanostructures* and recommend that it be accepted as fulfilling the dissertation requirement for the Degree of Doctor of Philosophy.

_____ Date: (12/14/15)
Galina Khitrova

_____ Date: (12/14/15)
Robert Norwood

_____ Date: (12/14/15)
Nasser Peyghambarian

Final approval and acceptance of this dissertation is contingent upon the candidate's submission of the final copies of the dissertation to the Graduate College.

I hereby certify that I have read this dissertation prepared under my direction and recommend that it be accepted as fulfilling the dissertation requirement.

_____ Date: (12/14/15)
Dissertation Director: Galina Khitrova

STATEMENT BY AUTHOR

This dissertation has been submitted in partial fulfillment of the requirements for an advanced degree at the University of Arizona and is deposited in the University Library to be made available to borrowers under rules of the Library.

Brief quotations from this dissertation are allowable without special permission, provided that an accurate acknowledgement of the source is made. Requests for permission for extended quotation from or reproduction of this manuscript in whole or in part may be granted by the head of the major department or the Dean of the Graduate College when in his or her judgment the proposed use of the material is in the interests of scholarship. In all other instances, however, permission must be obtained from the author.

SIGNED: Joshua D. Olitzky

ACKNOWLEDGMENTS

Firstly, I'd like to express my great appreciation to my advisor Galina Khitrova and unofficial advisor Hyatt Gibbs. The time spent in their labs and conversations had throughout the years have been invaluable to my pursuit of knowledge and career. I will cherish the time spent in the lab, at many conferences and wonderful social gatherings with Galina and Hyatt.

I would also like to thank professor's Lazlo Ujj and Chandra Sekar Prayaga who always encouraged me to pursue my interests in physics. The experiences I had under their guidance most certainly forged the path for my pursuit of a graduate degree in the sciences.

I couldn't have hoped for a more astute and friendly group of graduate students to work with during my time in graduate school. I'd like to thank them: Josh Hendrickson, Benjamin Richards, Julian Sweet, Michael Ghel, Ricky Gibson, and Sander Zandbergen.

I would not have been able to achieve any of this without the love, encouragement and support from my parents Earl and Mary, and my wife Marisa.

DEDICATION

This dissertation is dedicated to my incredibly loving and intelligent wife, Marisa Olitzky,
and to my ever supportive parents Earl and Mary Olitzky.

Contents

ABSTRACT	9
1 INTRODUCTION: QUANTUM CONFINED III-V MATERIALS, SPLIT RING RESONATORS, AND METALLIC NANO-ANTENNAES	10
1.1 MOTIVATION FOR USE OF III-V MATERIALS	10
1.1.1 <i>Direct Bandgap Bulk Semiconductor</i>	12
1.1.2 <i>Indirect Bandgap Bulk Semiconductor</i>	13
1.1.3 <i>Columbic Interactions Between Electron-Hole Pairs in Bulk Semiconductor</i>	16
1.1.4 <i>Quantum Confinement in One Dimension, Quantum Wells</i>	18
1.1.5 <i>Quantum Confinement in Two Dimensions, Quantum Dash</i>	23
1.1.6 <i>Quantum Confinement in Three Dimensions, Quantum Dots</i>	25
1.2 INTRODUCTION TO METALLIC SPLIT RING RESONATORS	26
1.3 PURCELL ENHANCEMENT	31
2 CHARACTERIZATION OF III-V MATERIAL GROWTH	32
2.1 LOW TEMPERATURE PHOTOLUMINESCENCE EMISSION DETECTION OF QUANTUM EMITTERS	33
2.2 QUANTITATIVE SURFACE ROUGHNESS AND NANO-STRUCTURE MEASUREMENTS VIA ATOMIC FORCE MICROSCOPY.....	36
2.3 GROWTH ON LONG WAVELENGTH QUANTUM DOTS SEVERAL NANOMETERS FROM THE SURFACE	38
3 METALLIC SPLIT RING RESONATORS	40
3.1 FABRICATION OF METALLIC SPLIT RING RESONATORS USING ELECTRON BEAM LITHOGRAPHY AND MICRO-FTIR TRANSMISSION CHARACTERIZATION	40
4 FEMTOSECOND TEMPORALLY AND SPECTRALLY RESOLVED PUMP PROBE SPECTROSCOPY OF SPLIT RING RESONATOR AND III-V GAIN COUPLED SYSTEMS	43

4.1	EXPERIMENTAL DESIGN AND APPARATUS	43
4.2	TWO LEVEL COUPLED OSCILLATOR MODEL FOR PLASMONIC METAMATERIAL RESONANCE AND TWO-LEVEL GAIN SYSTEM	48
4.3	TEMPORALLY AND SPECTRALLY RESOLVED RESULTS OF AG SRR ARRAYS AND QUANTUM WELLS	50
4.4	TEMPORALLY AND SPECTRALLY RESOLVED RESULTS OF AG SRR ARRAYS AND LONG WAVELENGTH QUANTUM WIRES	52
5	FUTURE DIRECTIONS AND STATE OF THE ART	57
6	APPENDIX JOURNAL PUBLICATIONS	61
7	REFERENCES.....	116

FIGURE 1	BANDGAP ENERGY VS LATTICE CONSTANT FOR COMMON III-V SEMICONDUCTOR MATERIALS.....	11
FIGURE 2	DIRECT BANDGAP SEMICONDUCTOR TRANSITION VIA ABSORPTION OF A PHOTON	13
FIGURE 3	INDIRECT BANDGAP SEMICONDUCTOR TRANSITION VIA ABSORPTION OF A PHOTON $\hbar\Omega$ WITH EITHER ABSORPTION OR EMISSION OF A PHONON, $+ - \hbar\Omega + k$ RESPECTIVELY	14
FIGURE 4	ABSORPTION OF DIRECT BANDGAP BULK SEMICONDUCTOR E_g IS THE BULK BANDGAP ENERGY	15
FIGURE 5	EXCITON ENERGY LEVELS INCLUDING BAND DISPERSION DUE TO CHANGES IN MOMENTUM k	17
FIGURE 6	EXCITONIC ABSORPTION PROFILES	18
FIGURE 7	SUBBAND TRANSITIONS IN A QUANTUM WELL.....	20
FIGURE 8	A SIMPLIFIED SCHEMATIC DIAGRAM OF ENERGY LEVELS AND CONFINEMENT POTENTIAL OF A QUANTUM WELL, WITH ALINAS BARRIERS AND INGAAS QUANTUM WELL MATERIAL SIMILAR TO THAT OF HSG37.	21
FIGURE 9	QUANTUM WELL ABSORPTION COMPARED TO BULK SEMICONDUCTOR FREE CARRIER ABSORPTION. PEAKS OF THE BLUE CURVE ARE THE EXCITON LINES.	23
FIGURE 10	QUANTUM WIRE ABSORPTION	24
FIGURE 11	SCANNING ELECTRON MICROGRAPH OF A SMALL SECTION OF AN ARRAY OF SPLIT RING RESONATORS	29

FIGURE 12 SIMPLE RLC MODEL FOR OBTAINING THE RESONANCE FREQUENCY OF THE SPLIT RING RESONATORS [16].....	30
FIGURE 13 LEFT, FTIR MICROTRANSMISSION SPECTRA OF SPLIT RING RESONATOR ARRAYS AND THEIR RESPECTIVE SEM IMAGES ON THE RIGHT.	30
FIGURE 14 LOW TEMPERATURE (4K) MICRO PHOTOLUMINESCENCE SPECTRUM OF PURCELL ENHANCED INAS QUANTUM DOTS IN PHOTONIC SLAB NANOCAVITY	32
FIGURE 15 PHOTOLUMINESCENCE SPECTROSCOPY APPARATUS, ABOVE BAND PUMPING IS ACHIEVED WITH THE USE OF EITHER THE Ti:SA LASER TUNED TO 810NM OR WITH A HeNe LASER CENTERED AT 632.8NM	34
FIGURE 16 LOW TEMPERATURE (10K) PHOTOLUMINESCENCE SPECTRA OF (A) HSG37 NEAR SURFACE QUANTUM WELL SAMPLE PUMPED AT 822NM AT VARIOUS PUMP INTENSITIES, AND (B) HSG44 NEAR SURFACE QUANTUM DASH SAMPLE AT DIFFERENT AT THE CENTER AND EDGE OF THE WAFER COMPARED WITH HSG24 PUMPED AT THE SAME POWER FOR EFFICIENCY REFERENCE.....	36
FIGURE 17 ATOMIC FORCE MICROSCOPY OF.....	37
FIGURE 18 STANDARD E-BEAM LITHOGRAPHIC FABRICATION WITH NEGATIVE RESIST MATERIAL	42
FIGURE 19 SEM IMAGES OF HSG24_P ARRAY SETS AND INDIVIDUAL SRR.....	43
FIGURE 20 FEMTOSECOND PUMP PROBE SPECTROSCOPY APPARATUS	45
FIGURE 21 DIFFERENTIAL TRANSMITTANCE OF NA1 SAMPLE FABRICATED ON HSG37.....	51
FIGURE 22 DIFFERENTIAL TRANSMITTANCE OF SRR SAMPLE NA1 ARRAY E6 FABRICATED ON HSG37, MEASURED ON TUCSON APPARATUS	51
FIGURE 23 DIFFERENTIAL TRANSMITTANCE OF SRR SAMPLE NA1 ARRAY E5 FABRICATED ON HSG37, MEASURED ON TUCSON APPARATUS.....	51
FIGURE 24 MAXIMUM DIFFERENTIAL TRANSMITTANCE MEASURED AT T = 20PS FOR 3 ARRAYS, E5, E6, E8 AND OFF ARRAY VS WAVELENGTH.	52
FIGURE 25 FTIR MICRO TRANSMISSION OF SEVERAL ARRAYS FROM HSG24_P SRR SAMPLE.....	53
FIGURE 26 DIFFERENTIAL TRANSMITTANCE $\Delta T/T$ OF HSG24_P ARRAY C12	55
FIGURE 27 TOY MODEL TWO-COUPLED OSCILLATOR FIT OF THE MAXIMUM $\Delta T/T$ OF HSG24_P ARRAY C12.....	57
FIGURE 28 (A) STRUCTURE DIAGRAM OF A PHOTONIC CRYSTAL SLAB NANO-CAVITY WITH A QUANTUM DOT LAYER (B) FDTD SIMULATION OF THE ELECTRIC FIELD PROFILE OF A PHOTONIC CRYSTAL SLAB NANO-CAVITY.	59

Abstract

Metallic nano-structures provide for new and exciting domains to investigate light-matter interactions. The coupling of these metallic nano-structures to semiconductor emitters allows for the observation of cavity QED effects including Purcell enhancement and Vacuum Rabi splitting. The focus of this dissertation will be to present an introduction and background to semiconductor optics, and metallic metamaterial systems. This will be followed by the presentation of the spectroscopy systems designed and constructed during my tenure as graduate student and the experimental data obtained with these systems. Some of the results have been published, while some of the presented material is still actively being pursued for publication. More specifically, the dissertation will cover the research at hand, experimental techniques, and results.

1 Introduction: Quantum Confined III-V Materials, Split Ring Resonators, and Metallic Nano-Antennas

1.1 Motivation for Use of III-V Materials

III-V materials have many inherent qualities that make them suitable for quantum confined semi-conductor structures. One such property of III-V materials is the direct bandgap nature of many combinations of III-V's, specifically GaAs, InAs, InGaAs, and GaAlInAs based "Zincblende" lattices. This direct bandgap structure allows for the efficient emission of light, a property that indirect bandgap materials such as Silicon do not exhibit. In addition, these III-V based material bandgap energies range from $\sim 0.38\text{eV}$ to $\sim 2\text{eV}$. This allows the use of higher energy bandgap alloys to effectively confine charge carriers in lower energy bandgap alloys in potential wells for the cases of quasi-2,1, and 0 dimensional semiconductors. Through various relative amounts of these materials in an alloy, the lattice constant and bandgap energy can be adjusted and exploited to shift wavelength response and material structure.

An important feature of any material selected for use is the ability to manufacture or produce such material. Molecular Beam Epitaxy, or MBE, was developed to accurately grow ultrathin layers of these semiconductor materials on the mono-molecular layer scale [38]. This crystallographic growth technique is highly repeatable and highly adjustable, allowing for a large variety of structures and alloys to be grown with extremely high fidelity. The basic growth technique has been adapted to several other similar techniques,

Molecular Vapor Phase Epitaxy is one such example. These similar techniques allow for similar quality growths in high volume. One can begin to see the many applications of these materials with emission in the near Infrared Red spectrum. A chart listing the III-V's bandgap energies and lattice constants is shown in Figure 1 for reference.

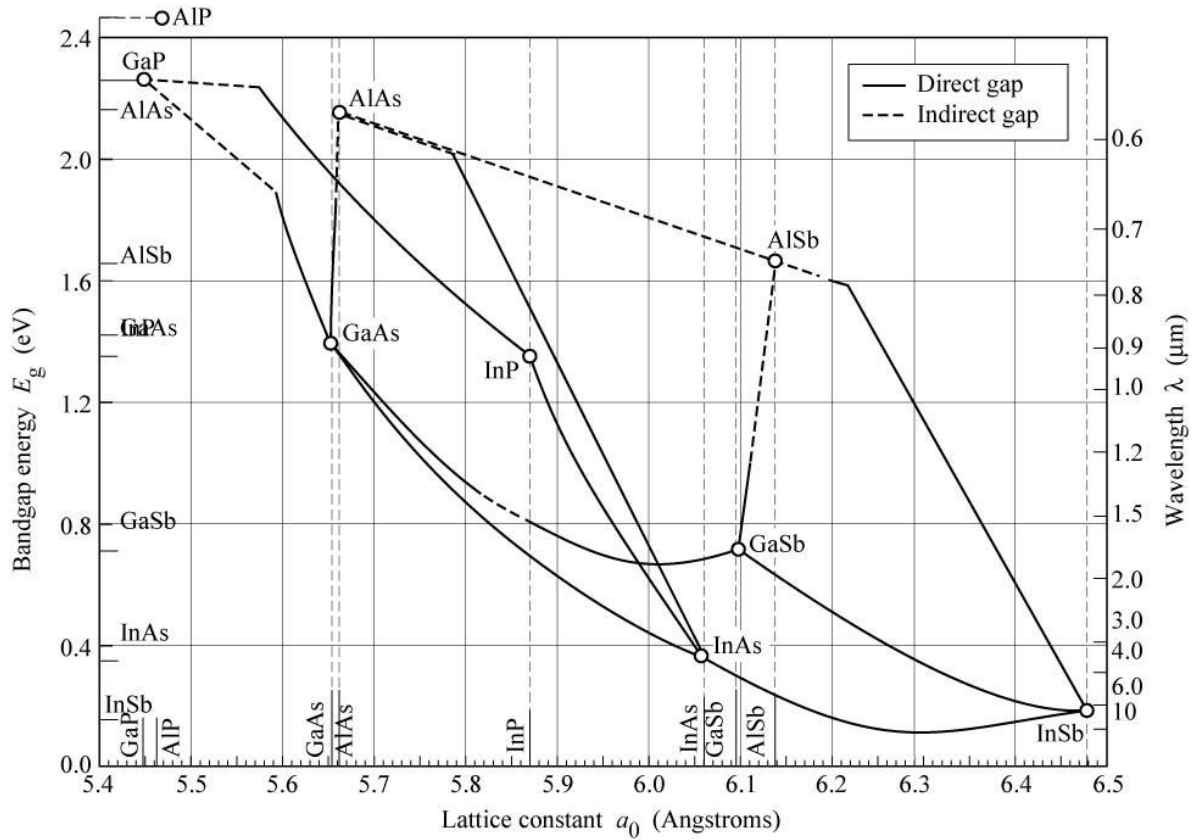


Figure 1
Bandgap Energy vs Lattice Constant for common III-V Semiconductor materials

We will start with an explanation of the bandgap and absorption characteristics of bulk semiconductor materials. This approach will help to understand the types of quantum confined semiconductor structures, and to introduce the concepts necessary to understand the data presented in this dissertation. Following that, a discussion will be presented on

excitons and quantum confined semiconductor structures with confinement in one, two and three dimensions, often called quasi-two, one and zero dimensional structures.

1.1.1 Direct Bandgap Bulk Semiconductor

For a bulk semiconductor the Kronig-Penney model will provide the general band structure of a material determined in the 3D Brillouin Zone. Using the Schrodinger equation with a square well periodic potential:

$$\left\{ \frac{-\hbar^2 \nabla^2}{2m} + V_L(\vec{r}) \right\} \varphi_{v,\vec{k}}(\vec{r}) = \varepsilon_{v,\vec{k}} \varphi_{v,\vec{k}}(\vec{r})$$

Where $\varepsilon_{v,\vec{k}}$ is the energy eigenvalue, \vec{k} is the momentum vector in the 1st Brillouin Zone,

$V_L(\vec{r})$ is the lattice potential in the crystal, and v is the band index. Using the Bloch

Theorem

$$\varphi_{v,\vec{k}}(\vec{r} + \vec{R}) = e^{i\vec{k} \cdot \vec{R}} \varphi_{v,\vec{k}}$$

near $k = 0$, for example the Γ -point in GaAs, we may approximate the Eigen energies with the Taylor expansion of

$$\varepsilon_{v,k} \approx \varepsilon_{c,0} + \frac{1}{2} \left. \frac{\partial^2 \varepsilon_{c,k}}{\partial k^2} \right|_{k=0} k^2$$

$$\varepsilon_{v,k} = \varepsilon_{c,0} + \frac{\hbar^2 k^2}{2m_c}$$

Here, m_c is the effective mass, which is determined by the curvature of the energy band.

This gives the dispersion curves of $\epsilon_{v,k}$ in general to have the form as depicted in Figure 2.

Also shown in Figure 2 is a schematic representation of an electron-hole pair excitation created by the absorption of a photon at frequency $\hbar\omega$ in a direct bandgap transition.

Momentum and energy conservation apply, however, often times in the case of direct bandgap transitions no momentum change occurs [1].

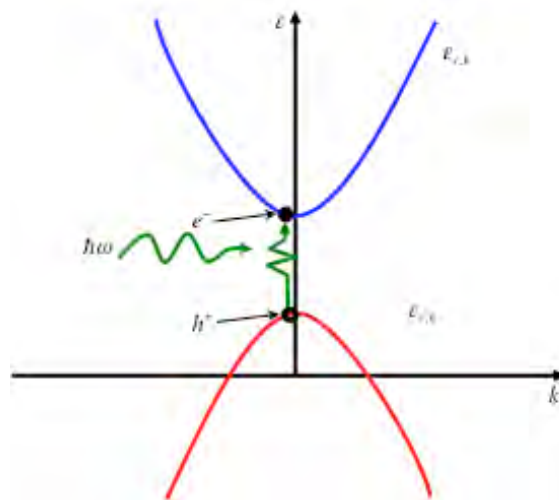


Figure 2
Direct bandgap semiconductor transition via absorption of a photon

1.1.2 Indirect Bandgap Bulk Semiconductor

Turning to the case of indirect bandgap materials, where the extrema of valence and conduction bands are at different points in the Brillouin zone, a transition cannot be made through absorption of a photon alone [1,2]. A phonon must be absorbed or emitted to

conserve energy $\epsilon_F = \epsilon_i + \hbar\omega \pm \hbar\Omega$, and momentum conservation, $\vec{k}_F = \vec{k}_i \pm \vec{k}$, requires a change in momentum \vec{k} as well. Figure 3 shows a general depiction of this band structure.

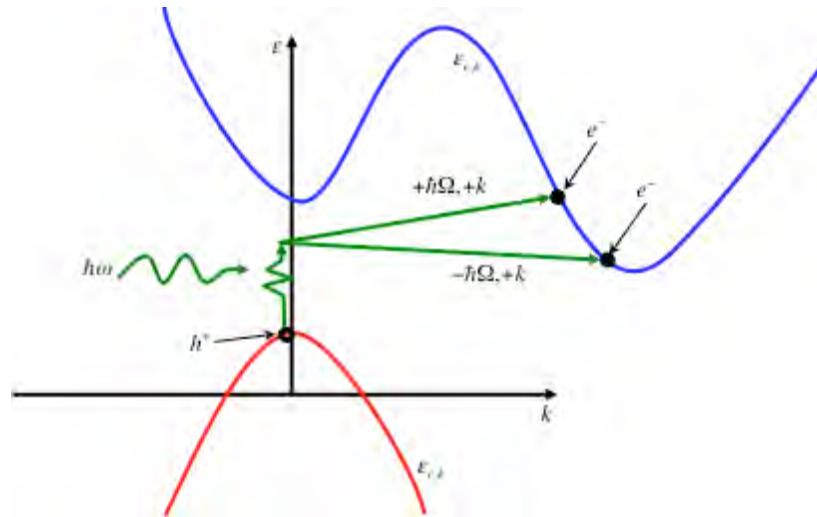


Figure 3
Indirect bandgap semiconductor transition via absorption of a photon $\hbar\omega$ with either absorption or emission of a phonon, $\pm \hbar\Omega + k$ respectively

It was previously stated that indirect bandgap materials are unsuitable emitters. This is due to the requirement of two quanta, a photon and phonon. Indirect bandgap transitions are second order and therefore much weaker than, often several orders of magnitude, 1st order dipole allowed transitions [1]. The significant efficiency loss and clear difference from direct bandgap semiconductors illuminates the choice to use III-V alloys for the following experiments. With their direct bandgap nature and red to infrared emission characteristics it becomes apparent that direct bandgap III-V materials are a unique set of semiconductor crystalline materials.

In the semi-classical treatment where the quantum nature of the material is taken into account but the field remains classical, very good results for the optical absorption in bulk material can be obtained [1]. This is considered the free carrier absorption in bulk semiconductor. For a direct band gap structure the absorption coefficient is

$$\alpha = \frac{2e^2}{n_b c m_0^2 \omega} |p_{cv}(0)|^2 \left(\frac{2m_r}{\hbar^2} \right)^{3/2} \theta(\hbar\omega - E_G) (\hbar\omega - E_G)^{1/2}$$

and is plotted in Figure 4 [1].

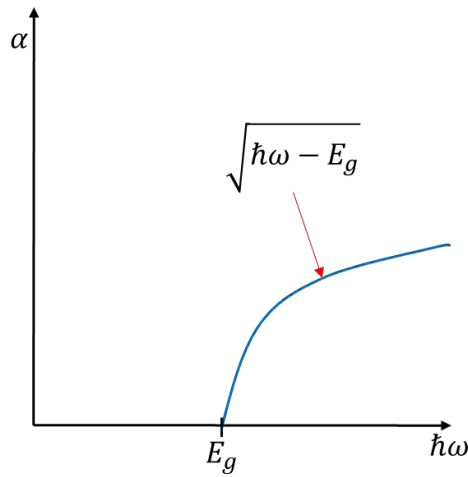


Figure 4
Absorption of direct bandgap bulk semiconductor E_g is the bulk bandgap energy

Note that no occupation of states exists below the bandgap energy E_g , however, this will not be the case for real semiconductor materials since the columbic interaction between the electron and hole has not been taken into account in the equation above. The discussions in the following sections will describe the modifications to the absorption coefficient with such Columbic interactions included for the case of bulk and quantum confined structures.

1.1.3 Columbic Interactions Between Electron-Hole Pairs in Bulk Semiconductor

As stated above, the Columbic interaction between the electron and hole in bulk material was not yet considered. However, the binding between these particles significantly affects the optical absorption in a semiconductor, especially in the cases of quantum confinement [1]. The Wannier Equation can describe the interaction between the electron and hole,

$$\left[-\frac{\hbar^2}{2m_r} \nabla_r^2 - \frac{e^2}{\epsilon_0 r} \right] \phi(r) = \epsilon_r \phi(r)$$

with energy Eigen values ,

$$\epsilon_r = \epsilon_{n,l,m} = \frac{-m_r e^4}{2\hbar^2 e_0^2} \left(\frac{1}{n^2} \right) = -E_B \left(\frac{1}{n^2} \right) , \quad a_B = \frac{\epsilon_0 \hbar^2}{m_r e^2}$$

E_B , is the Rydberg energy and a_b is the exciton Bohr radius. These are the same form as the solutions to the Hydrogen atom. The total energy of the exciton including the center of

mass contribution $\epsilon_R = \frac{\hbar^2 K_c^2}{2M}$ is,

$$\epsilon_n = E_g - E_B \left(\frac{1}{n^2} \right) + \frac{\hbar^2 K_c^2}{2M}$$

This describes a series of hydrogenic energy bands in the forbidden region of the bandgap

Figure 5.

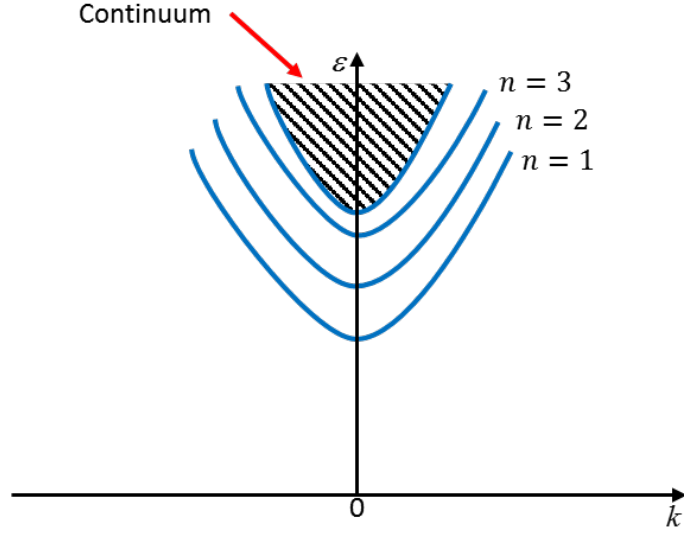


Figure 5
Exciton energy levels including band dispersion due to changes in momentum k .

With the inclusion of the Excitonic effects into the joint density of states, the absorption coefficient in bulk semiconductors is considerably different than the free carrier bulk absorption presented earlier [1].

$$\alpha(\omega) = \frac{e^2 \omega |d_{cv}|^2}{n_b c \epsilon_0} \left(\frac{2m_r}{\hbar^2} \right)^2 \left[E_b \sum_{n=1}^{\infty} \frac{4\pi}{n^3} \delta(\hbar\omega - E_g + E_B/n^2 + \theta(\hbar\omega - E_g)) \frac{\pi e^{(\pi \sqrt{E_B/(\hbar\omega - E_g)})}}{\sinh(\pi \sqrt{E_B/(\hbar\omega - E_g)})} \right]$$

The spacing of the energy Eigen values $\epsilon_n = E_g - E_B \left(\frac{1}{n^2} \right) + \frac{\hbar^2 K_c^2}{2M}$ appears in the absorption profile as delta function with decreasing intensity at locations \propto to $1/n^2$ at lower energies than the bandgap. To emphasize this a bit more, there are absorption peaks in the forbidden zone of the free carrier analysis. The free carrier absorption profile is also affected by the Coulombic potential as seen in the last term of the absorption coefficient;

see Figure 6.

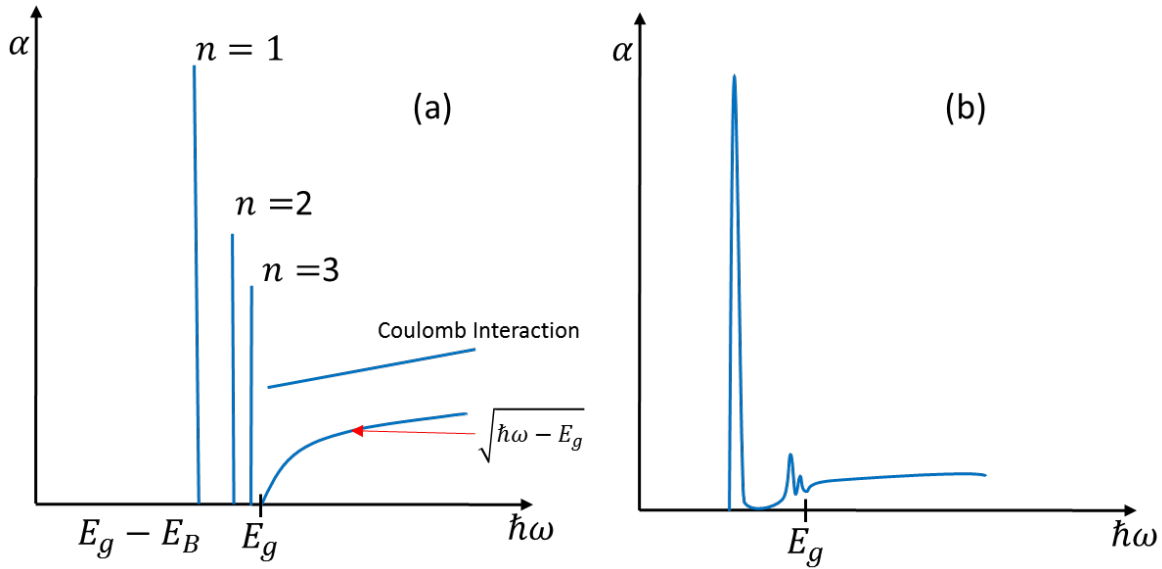


Figure 6

Excitonic absorption profiles

(a) Discrete absorption lines of the exciton in the forbidden region with Coulombic interaction included (b) absorption spectrum of a semiconductor with excitonic absorption

1.1.4 Quantum Confinement in One Dimension, Quantum Wells

Turning to the cases of quantum confinement in semiconductor materials and beginning first with the case of confinement in one dimension, quantum well structures. The problem of the infinite potential well is solved by inserting the function

$$V(z) = \begin{cases} 0, & 0 \leq x \leq L \\ \infty, & \text{else} \end{cases}$$

into the Schrodinger Equation. Often this is the first potential inserted into the Schrodinger equation in elementary texts [3,4]. Although the ideal case of the infinite potential well does not exist in practice, simple analytical solutions for this case exist and yield useful insight into the principal of quantum confinement. The Schrodinger Equation in three dimensions with an infinite well in the z-direction is as follows [1].

$$\left[\frac{-\hbar^2}{2m} \nabla^2 + V(z) \right] \psi(x, y, z) = \varepsilon \psi(x, y, z)$$

$$V(z) = \begin{cases} 0 & -L_z/2 < z < L_z/2 \\ \infty & |z| > L_z/2 \end{cases}$$

This equation is separable into $\phi(x, y)\zeta(z)$. The energy Eigen values of $\phi(x, y)$ are that of

a free particle with plane wave solutions $\varepsilon_{\perp}(k) = \frac{\hbar^2}{2m}(k_x^2 + k_y^2)$ [1,3,4]. In the confined z-

direction the energy Eigen values are [1,3,4].

$$\varepsilon_z = \frac{\hbar^2}{2m} \left(\frac{j^2 \pi^2}{L_z^2} \right) \quad j = 1, 2, 3, \dots$$

The total energy is simply

$$\varepsilon = \frac{\hbar^2}{2m} \left(\frac{j^2 \pi^2}{L_z^2} + k_x^2 + k_y^2 \right) \quad j = 1, 2, 3, \dots$$

So, the energy of the particle has a quasi-continuum of states in the x and y unconfined directions and discrete states in the z-direction dependent on the length of the well [1].

Graphically this can be depicted as sets of parabolic bands with spacing $\frac{1}{2m} \left(\frac{\hbar j \pi}{L_z} \right)^2$

Figure 7.

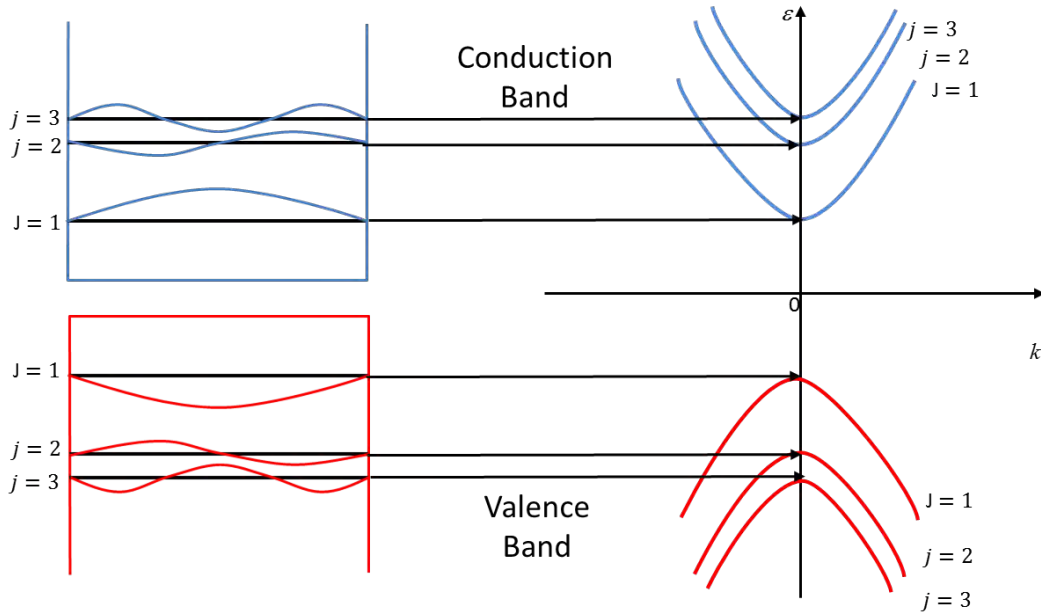


Figure 7
Subband Transitions in a Quantum Well. Left, subband energy levels of an electron-hole pair confined in one dimension of an infinite potential well. Right, parabolic bands representing the subband transitions with free propagation in the X and Y dimensions taken into account.

In the more realistic case of finite potential well, the wave function does not equal zero at the boundaries. One consequence of this is that there does not exist an infinite number of bound states as in the infinite potential. However, the bound states still follow a spacing of

$\epsilon \approx \frac{\hbar^2}{2m} \frac{j^2 \pi^2}{L_z^2}$ with a parabolic band structure until they are ionized into the continuum. The

scaling of the energy with respect to well length of $1/L_z^2$ is known as the Quantum Size Effect [1]. Consequently, the energy levels can be shifted or tuned simply by changing the thickness of the quantum well. In practice, the thickness of the well is easily controlled during MBE or MOCVD crystallographic growth techniques. In the following research presented many InGaAs ($E_g \approx 0.813 eV$) quantum wells were produced using InAlAs

($E_g \approx 1.5eV$) as the barrier material, with absorption centered on 1500nm ($E_g \approx 0.82eV$); see a schematic representation in Figure 8 [5,6].

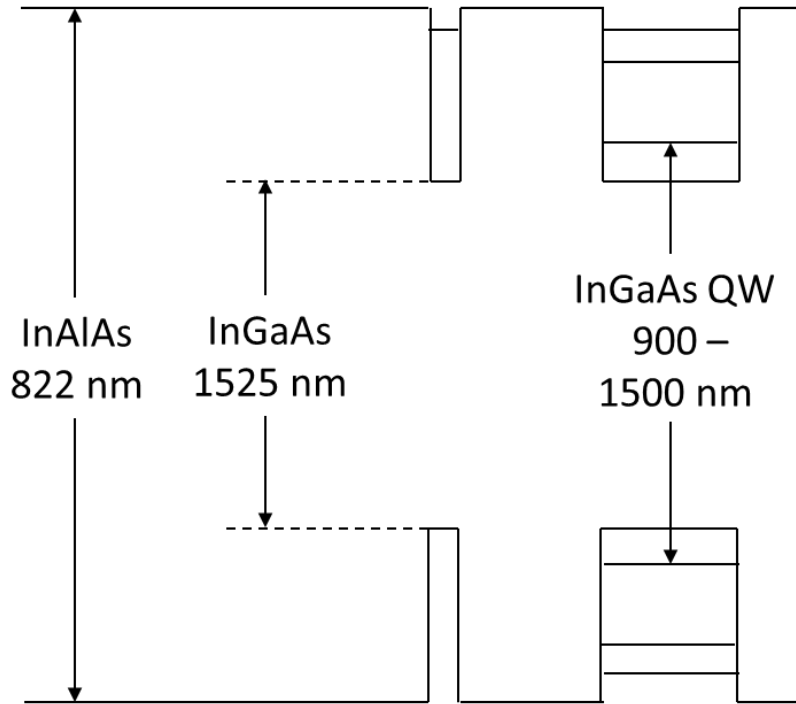


Figure 8
A simplified schematic diagram of energy levels and confinement potential of a quantum well, with AlInAs barriers and InGaAs quantum well material similar to that of HSG37.

Due to the confinement in one dimension from the well, and including the excitonic effects, the Eigen energies become

$$\varepsilon_n = E_g + \frac{\hbar^2 \pi^2 j^2}{2m_r L_z^2} - \frac{E_B}{(n_j - 1/2)} \quad n_j = 1, 2, 3, \dots$$

Each energy step due to the confinement of the electron hole pair now has an associated excitonic series.

An important consequence of the quantum confinement is the change in the ground state

energy compared to the free exciton case. The ground state energy here is 4 times that of the free exciton, driving the exciton absorption lines further away from the bandgap energy. The physically intuitive explanation of this is that the confinement of the exciton reduces the distance between the electron-hole pair, therefore reducing the Bohr radius, which increases the oscillator strength and yields stronger resonances. The absorption coefficient for the quantum well is then (the Elliot Formula)

$$\alpha(\omega) = \frac{2\pi\omega |d_{cv}|^2}{n_0 c L_z} \left(\frac{2m_r}{\hbar^2} \right) \left[\sum_{n=1}^{\infty} \frac{4E_B}{(n-1/2)^3} \delta \left(\hbar\omega - E_G + \frac{\hbar^2 \pi^2 j^2}{2m_r L_z^2} + \frac{E_B}{(n-1/2)^2} \right) \right. \\ \left. + \theta \left(\hbar\omega - E_G + \frac{\hbar^2 \pi^2 j^2}{2m_r L_z^2} \right) \frac{e^{\pi / \sqrt{\left(\hbar\omega - E_G + \frac{\hbar^2 \pi^2 j^2}{2m_r L_z^2} \right) / E_B}}}{\cosh \left(\pi / \sqrt{\left(\hbar\omega - E_G + \frac{\hbar^2 \pi^2 j^2}{2m_r L_z^2} \right) / E_B} \right)} \right]$$

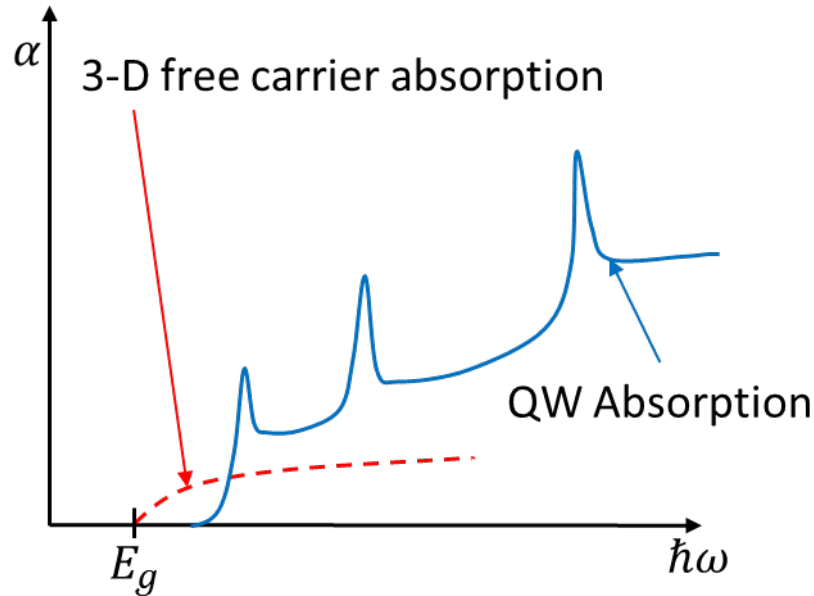


Figure 9
Quantum well absorption compared to bulk semiconductor free carrier absorption. Peaks of the blue curve are the exciton lines.

Interesting differences due to the confinement are easily seen in Figure 9. The continuum absorption is now twice that of the free carrier case. The exciton lines are much farther from the band edge and now are much more spectrally resolved. It is worth emphasizing that these effects are due to confinement in only one dimension. Physically, that is a thin layer of lower energy band gap material sandwiched by higher energy band gap material.

1.1.5 Quantum Confinement in Two Dimensions, Quantum Dash

With such striking effects due to confinement in one dimension, interest in higher orders of confinement is quite natural. The next logical step in further confining the exciton is the quantum wire or dash. The quantum wire would then confine the exciton in two

dimensions, allowing free particle movement in one dimension. These are often referred to in the literature as quasi-one-dimensional quantum structures [1,2]. The absorption coefficient for the case of the quantum wire includes Whittaker Functions and can be found in ref. [2]; the absorption profile is presented here in Figure 10.

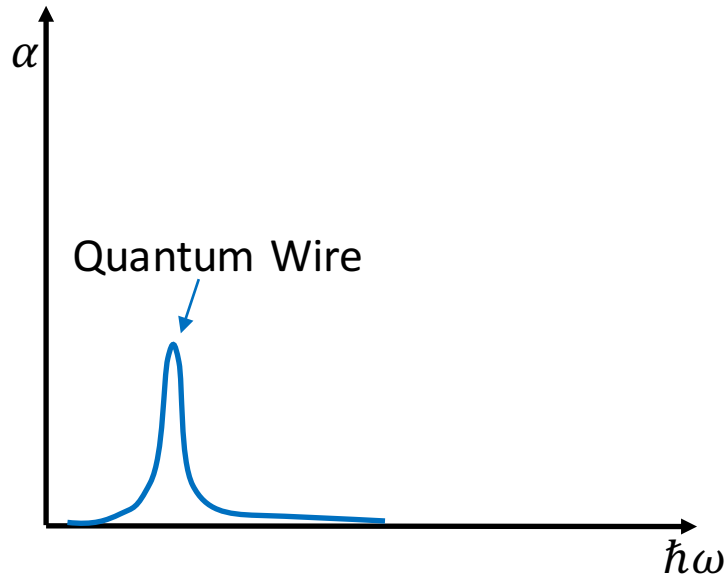


Figure 10
Quantum wire absorption with 3D bulk free carrier absorption for reference. The exciton resonance is pushed out of the continuum due to the increased confinement and the oscillator strength is mostly accumulated in the ground state exciton [1].

The higher confinement in the quantum wire increases the binding energy significantly and drives the excitonic lines even further from the band edge than the case of the quantum well [1,2]. The Exciton ground state accounts for the majority of the total oscillator strength and the second excited state dominates the absorption profile due to parity selection rules [2]. Higher order excited states have very low oscillator strengths and therefore vanish quickly as order is increased [2].

1.1.6 Quantum Confinement in Three Dimensions, Quantum Dots

It's clear that the next step in increased confinement is confinement in three-dimensions, often called a quasi-zero-dimensional structure, or quantum dots in the literature [1,2].

Quite naturally for confinement in the third dimension of the infinite potential well the energy Eigen values become [1,3,4]

$$\varepsilon = \frac{\hbar^2 \pi^2}{2m} \left(\left(\frac{j}{L_x} \right)^2 + \left(\frac{j}{L_y} \right)^2 + \left(\frac{j}{L_z} \right)^2 \right) \quad j = 1, 2, 3, \dots$$

Many dots are semi-spherical in shape, including the pancake shaped dots grown for this research [10]. In an infinite spherical potential the Eigen energies become [1]

$$\varepsilon^i = \frac{\hbar^2 \pi^2}{2m_i} \left(\frac{\alpha_{nl}}{R} \right)^2$$

with α_{nl} as the n th root to the l th Bessel Function. Note the characteristic blue shift based on confinement that shifts like $1/R^2$ with a series of eigenstates. The above is the single particle energy; the total energy is of the same form as the above for the electron and hole with the addition of band gap energy

$$\varepsilon = E_g + \frac{\hbar^2}{2m_e} \left(\frac{\alpha_{n_e l_e}}{R} \right)^2 + \frac{\hbar^2}{2m_h} \left(\frac{\alpha_{n_h l_h}}{R} \right)^2$$

The absorption coefficient of the quantum dot is as follows

$$a(\omega) = \frac{4\pi\omega}{\hbar c \sqrt{\varepsilon_2}} \sum_i |d_{0i}|^2 \frac{\gamma_i}{\gamma_i^2 + (\omega_i - \omega)^2}$$

Here, ε_2 is the background dielectric constant, d_{0i} is the dipole matrix element of the

transition from 0 to I, and γ_i is the homogenously broadened linewidth. The absorption lines are then a series of Lorentzians centered about the electron hole pair energies $\hbar\omega_i = \varepsilon_i \propto 1/R^2$. There is no bulk absorption band edge near these transitions due to the large blue shift. The Quantum dot is the semiconductor counterpart to the Hydrogen atom.

1.2 Introduction to Metallic Split Ring Resonators

It was Veselago who first presented the idea of negative index materials in his 1968 paper [11]. He realized that if both the dielectric constant ε and magnetic permeability μ were negative, the system would become what he termed a “Left Handed System”. It is easy to show that in an isotropic medium the dispersion relation is

$$k^2 = \frac{\omega^2}{c^2} n^2 \quad \text{with} \quad n^2 = \varepsilon\mu$$

If both ε and μ are negative the equations above are still valid. Hence, there is no fundamental reason that a material with negative values of ε or μ would be forbidden by Electromagnetic Theory [11]. Maxwell’s equations give the following relations for a plane monochromatic wave $e^{i(kz-\omega t)}$

$$k \times E = \frac{\omega}{c} \mu H, \quad k \times H = -\frac{\omega}{c} \varepsilon E$$

Directly from those equations the system becomes Left Handed if $\varepsilon < 0$ and $\mu < 0$.

Veselago pointed out several interesting results of this at the time for hypothetical materials, as no naturally occurring negative index materials exist in the optical frequencies [11]. Snell’s law written correctly for the case of material interfaces with different

handedness will be

$$\frac{\sin\phi_2}{\sin\phi_1} = \frac{p_2}{p_1} \sqrt{\frac{\epsilon_2\mu_2}{\epsilon_1\mu_1}}$$

Here, $p_{1,2}$ are the “handedness of the materials”, $p = 1$ indicates a completely right handed material while $p = -1$ indicates a completely left handed material [11]. According to this rewritten Snell’s law, if the index of the mediums are different and one is negative, refraction will also be negative. This will reverse the roles of negative index materials with respect to a typical right-handed materials.

Another interesting effect occurs for the special case when $\epsilon_1 = -\epsilon_2$ and $\mu_1 = -\mu_2$. For those values there is no reflected ray. These results were striking, yet purely hypothetical at the time. No naturally occurring left-handed materials exist, so they must be engineered [12].

Veselago’s paper went largely uncited until JB Pendry’s seminal paper on perfect lensing [12,13]. After Pendry’s paper, activity in the subject greatly increased. The work to design such materials by Smith et al. demonstrated the first LHM’s (Left Handed Materials) [12,13]. Since then, work on these so called “Meta-Materials” has continued to increase in volume and the development and investigations of these engineered materials has produced many fascinating results; see Ref. 12 for a comprehensive overview.

This dissertation will focus predominately on those of the “Horseshoe” single split ring resonator type. To elaborate on Pendry’s theoretical findings, Pendry noticed an important

difference from a standard positive index optical element. A positive index optical element applies a phase correction factor to produce an image. The evanescent fields decay, thus limiting the resolution of such imaging systems to [14]

$$\Delta \approx \frac{2\pi c}{\omega} = \lambda$$

However, a planar material with index $n = -1$ actually amplifies the evanescent waves and the information is not lost. These higher order Fourier components are amplified in the material and then decay upon exiting the material. The decay length works out such that the field intensity at the image plane is exactly the same as the intensity at the object plane. Since the high order Fourier components are not lost, the system can image in a sub-diffraction limit or “Superlensing” capacity [14].

A promising meta-material that exhibits both negative ϵ and μ at optical frequencies is the metallic single split ring resonator design first demonstrated by Liden et al. with resonances up to 100 THz [15]; see Figure 11. These structures were then fabricated later to frequencies of 200 THz, the very useful 1550nm wavelength band used in telecommunication [16].

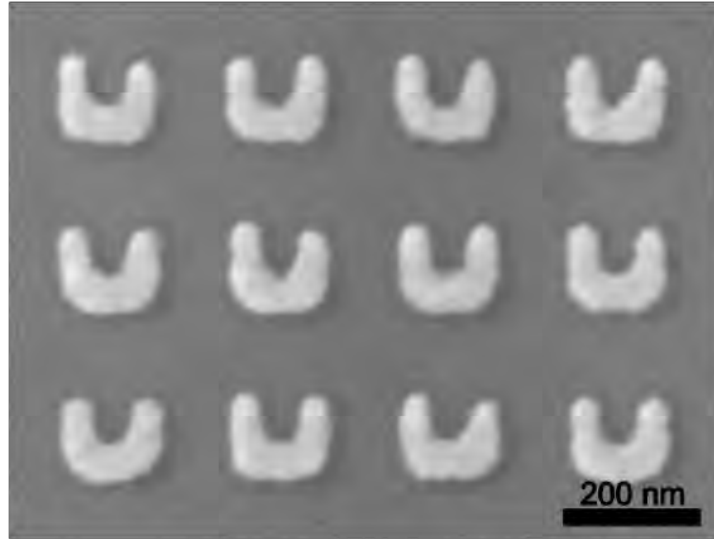


Figure 11
Scanning electron micrograph of a small section of an array of split ring resonators

An intuitive way to think of these SRR's is to imagine them as an array of magnetic atoms. While not on the size scale of an atom, they are an order of magnitude smaller than the wavelength of light and, therefore, are small enough to appear to the light field as a homogenous negative μ material. Elementary statics can give an intuitive look at the behavior of such structures. The SRR is roughly a split coil that forms part of an inductive loop and a capacitive gap. The resonance frequency ω_{LC} can be determined by writing the capacitance of a large plate capacitor and a long inductor with windings equal to 1 [16].

$$C = \epsilon_0 \epsilon_c \frac{\omega t}{d} \quad \text{and} \quad L = \mu_0 \frac{l^2}{t}$$

The resonance frequency follows, with l = length of the sides, d = to the gap spacing, w equal to the width of the base, and ϵ_c equal to the dielectric constant of the material in the gap.

$$\omega_{LC} = \frac{1}{\sqrt{LC}} = \frac{1}{l} \frac{c_0}{\sqrt{\epsilon_C}} \sqrt{\frac{d}{w}}$$

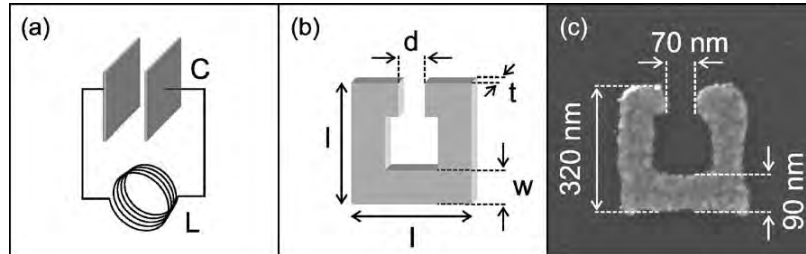


Figure 12
Simple RLC model for obtaining the resonance frequency of the split ring resonators [16].

This formula, while not the complete story, gives a good approximation of where the resonance frequency lies [17]. Figure 13 shows arrays of fabricated SRRs with their respective transmission spectra.

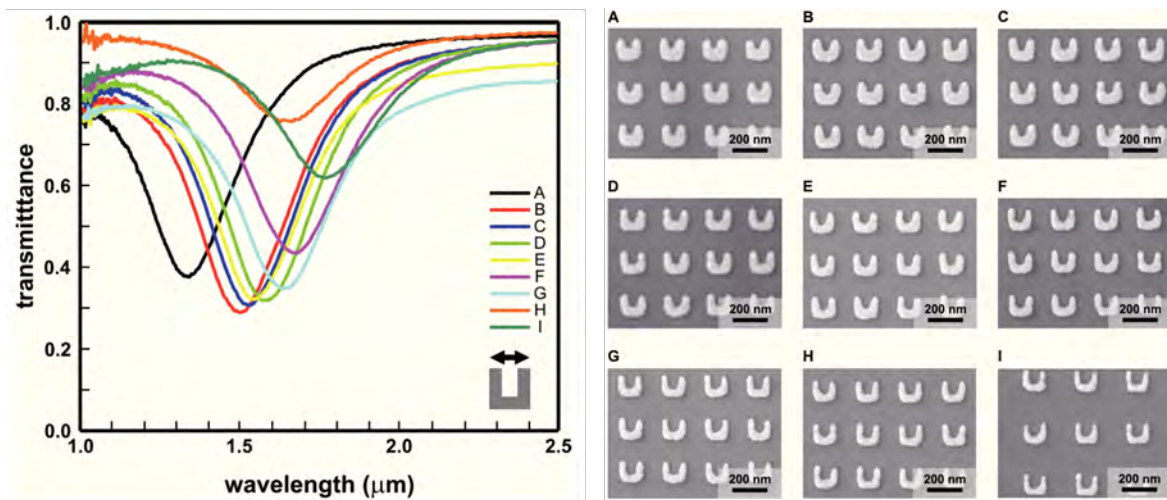


Figure 13
Left, FTIR microtransmission spectra of split ring resonator arrays and their respective SEM images on the right.

1.3 Purcell Enhancement

Edwin Purcell first introduced the concept of modifying spontaneous emission rates through cavity interactions in his 1946 publication [18]. Purcell had determined that an oscillator at frequency ν , coupled to a resonant cavity with a quality factor $Q = \nu/\delta\nu$, would experience an increased emission probability. That Purcell factor is

$$f = \frac{3Q\lambda^3}{4\pi^2V}$$

This result went largely un-cited until Eli Yablonovic published his predictions of controlling spontaneous emission rates in the solid-state. Although his goal was to inhibit spontaneous emission in semiconductor lasers, its basis was in using the Purcell factor to do so [19]. An exponential growth of citations to Purcell's publication ensued. To date, Purcell's paper has been cited ~2293 times, and Yablonovich's an astounding ~9800.

An example of the Purcell enhancement of quantum dot emission in a photonic crystal slab non-cavity can be seen in Figure 14 as the much higher intensity peaks above the ensemble photoluminescence emission.

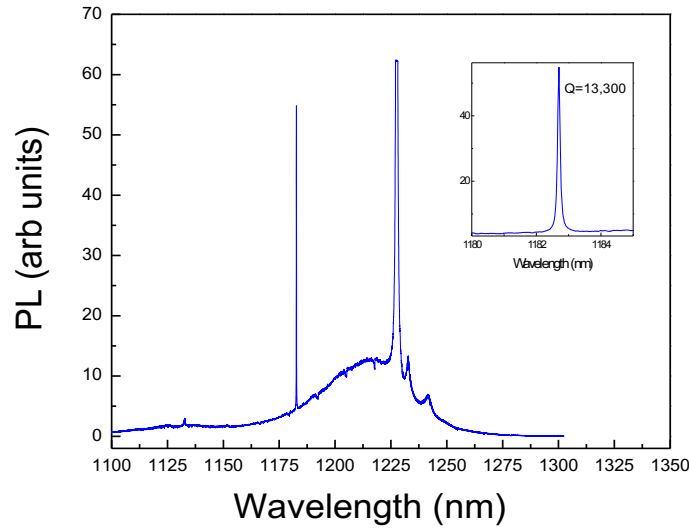


Figure 14

Low temperature (4K) micro photoluminescence spectrum of Purcell enhanced InAs quantum dots in photonic slab nanocavity. The broad emission profile is the unenhanced ensemble QD emission.

2 Characterization of III-V Material Growth

The semiconductor structures presented in this dissertation are all III-V group materials grown by Molecular Beam Epitaxy. Molecular Beam Epitaxy, or MBE, is a highly controllable method of semiconductor crystal growth. It allows for ultrapure materials to be deposited in stoichiometric ratios with monoatomic layer precision. It has proven to be an extremely useful key technology in the development of semiconductor fundamental and device research [20].

To characterize the samples grown for the experiments at hand, several imaging and spectroscopic techniques were used. These techniques allowed for the determination of

emission center wavelength, emission linewidth and relative emission efficiencies in the quantum confined structures, surface roughness, and dot density and size to sub-nanometer resolution. The primary method of determining the quantum well, dot, or dash excitonic spectroscopic information was by low temperature photoluminescence spectroscopy, while surface roughness dot size, and dot density were quantified via Atomic Force Microscopy.

2.1 Low Temperature Photoluminescence Emission Detection of Quantum Emitters

Photoluminescence (PL) is the spontaneous emission profile of an emitter that has been excited above the bulk material band edge by an external laser source. The hot, energetic charge carriers cool through non-radiative means into the quantum well, dash or dots. Once the carriers are captured by the quantum structures the carriers can recombine and emit at the well, dash, or dots respective allowed frequencies. The low temperature PL used to characterize the samples grown by MBE was performed with the experimental apparatus shown in Figure 15.

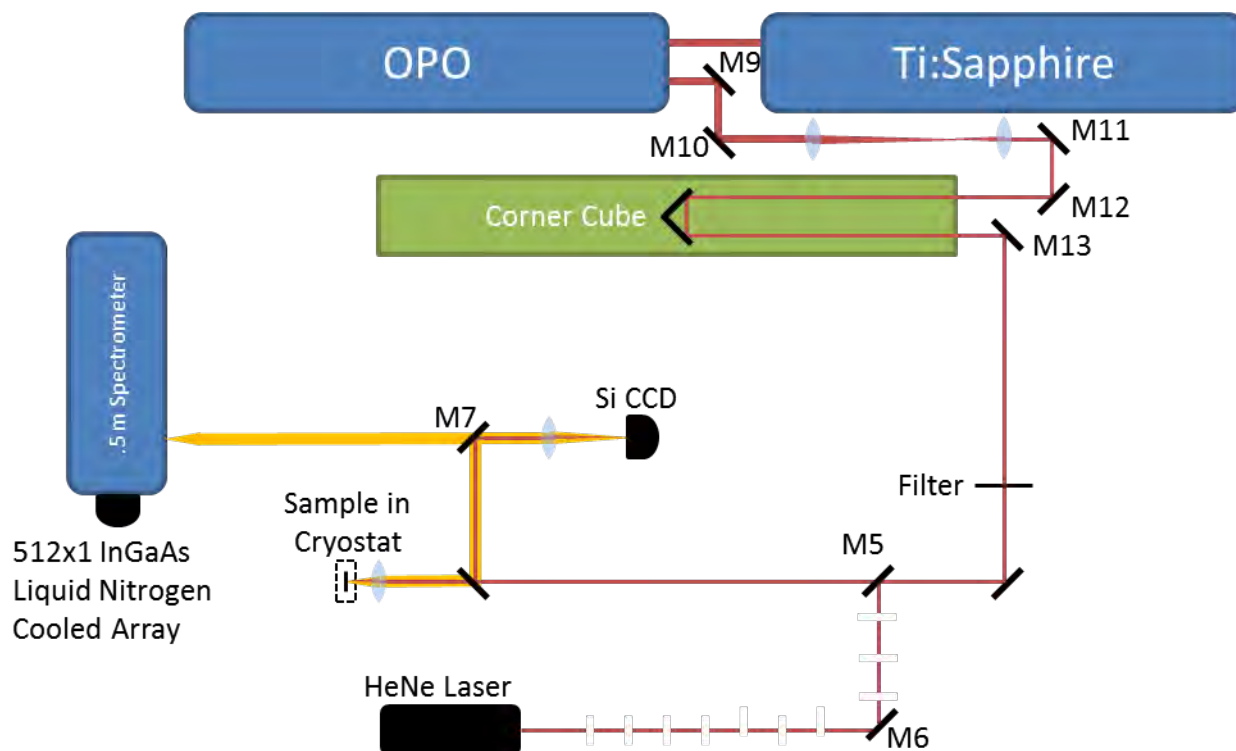


Figure 15
 Photoluminescence Spectroscopy apparatus, above band pumping is achieved with the use of either the Ti:Sa laser tuned to 810nm or with a HeNe laser centered at 632.8nm

Samples were cooled to cryogenic temperatures of 10K using an ARS closed cycle Helium cryostat. To determine the sample response with respect to temperature the cryostat's internal heater had the ability to regulate the temperature of the sample mount to approximately one-tenth of a degree. The sample volume of the cryostat was evacuated with a Varian TPS-compact turbo molecular pump system to pressures of less than 30 μ Torr prior to cooling the sample to eliminate condensation of water or other contaminants that would shift the resonance of the SRR's. The samples were pumped above band using either a Spectra Physics Tsunami femtosecond Ti:Sapphire laser tuned to 810-820nm or a He:Ne laser centered at 632nm. Excitation spots were measured to be

25 μ m in diameter. Variable neutral density filters in the collimated space of the beam controlled incident laser excitation power.

The photoluminescence from the sample is emitted into a 4π solid angle and was collected in a reflection type arrangement. Collection of emitted energy was accomplished using the front focusing lens. A partially reflective pellicle beam splitter was used to pick off the collected photoluminescence signal and direct it towards the spectrometer. Prior to entering the spectrometer, the signal was filtered to remove any residual pump using SEMROCK knife-edge filters. The filtered signal beam was then collected and coupled into the spectrometer. The spectrometer model was a Princeton Instruments Acton Spectrapro 500mm focal length grating spectrometer. Light detection at the output of the spectrometer was achieved with a Princeton Instruments OMA V liquid nitrogen cooled 512 pixel linear InGaAs array. The spectroscopic system was calibrated and dispersion compensated using neon and krypton gas discharge calibration sources with a minimum of 4 spectral lines that spanned the useful range of the spectrometer \sim 700-1600nm. An example of PL collected from the quantum well sample HSG37 and the Quantum dash HSG44 sample is shown in Figure 16. The high frequency noise in the spectra of the quantum dash sample is an artifact generated by the experimental apparatus and is not a characteristic of the PL emission.

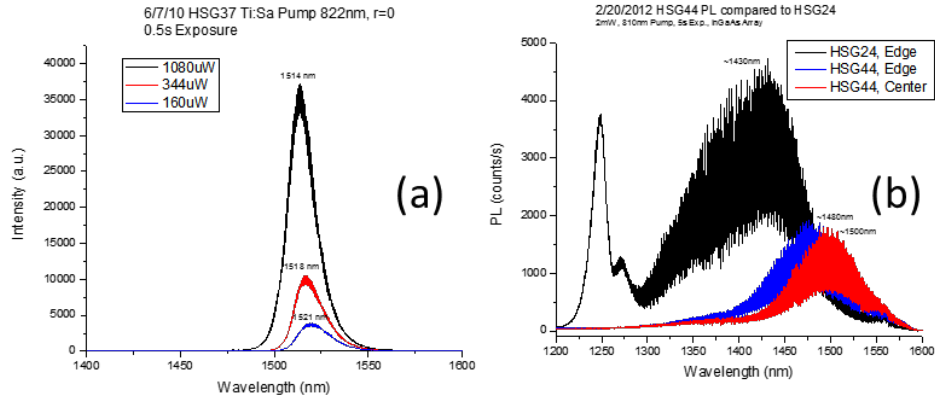


Figure 16

Low temperature (10K) photoluminescence spectra of (a) HSG37 near surface quantum well sample pumped at 822nm at various pump intensities, and (b) HSG44 near surface quantum dash sample at different at the center and edge of the wafer compared with HSG24 pumped at the same power for efficiency reference.

2.2 Quantitative Surface Roughness and Nano-Structure Measurements via Atomic Force Microscopy

Atomic Force Microscopy is a method of determining surface morphology with resolution far beyond the diffraction limit of optical imaging techniques. It consists of rastering an ultra-sharp tip in the x-y plane across the surface of a sample while measuring the deflection of the tip. This deflection data can then be used to generate surface images of the sample in question.

For the HSG series used in this research, samples were examined with AFM imaging to determine surface roughness and to determine what type and density of quantum dots or dashes had been grown. Long wavelength quantum dot samples had not previously been grown by the group and growth parameters took many iterations to optimize both the dot

density and surface roughness. As the samples were being optimized often the dot portion of the growth was repeated on the barrier cap shown in Figure 17-a. While these dots are not optically active, due to the absence of the barrier cap, they provide dot density and dot/dash shape characteristics. In fact, the first long wavelength attempts at quantum dots yielded quantum dashes, which was quickly identified by the implementation of this technique.

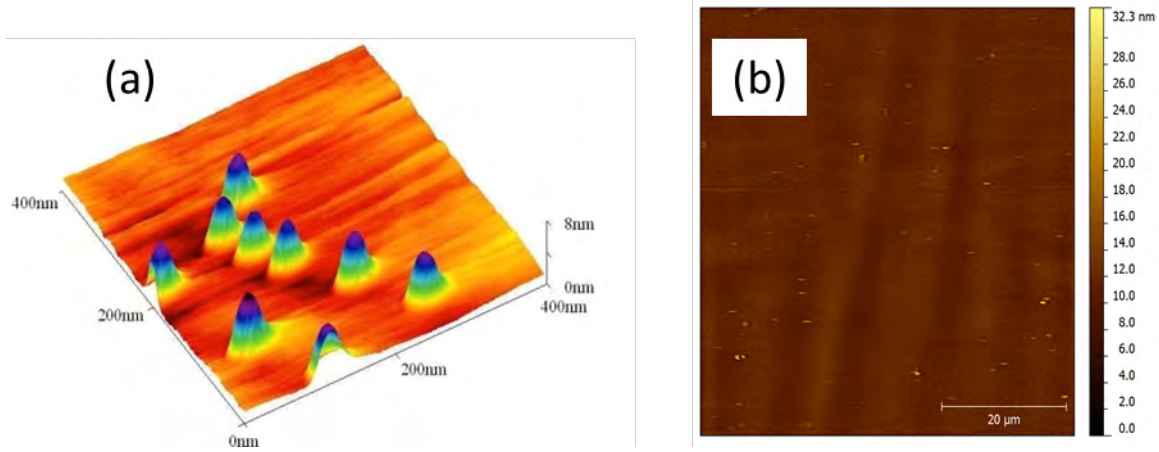


Figure 17
Atomic Force Microscopy of (a) a quantum dot sample with dot growth repeated on the cap surface to determine dot size and density. (b) HSG44 long wavelength near surface quantum dash sample AFM image.

As noted earlier, the surface roughness was of great importance for these samples, since the goal was to have 30nm tall split ring resonators fabricated on the surface. AFM played a crucial role in determining the surface roughness of the samples grown and eventually drove the group away from the Enzmann InGaAS/AlInAs matrix type long wavelength dots to long wavelength dot growth with the removal of the GaAlInAs matrix and the addition of GaAs wetting layer, similar to the wetting layer commonly used in shorter

wavelength dots. HSG44 long wavelength quantum dash sample AFM surface false color image is shown in Figure 17-b.

2.3 Growth on Long Wavelength Quantum Dots Several Nanometers from the Surface

Many samples have been grown in support of the experiments and results presented in this dissertation. The goal of the growth was to fabricate quantum wells and quantum dots very near to the surface. Metallic split ring resonators were then fabricated on the surface to investigate the temporal and spectral coupling characteristics between the two nanostructures. With that goal in mind, the motivating factor for surface to quantum confined nanostructure spacing was twofold. First, the coupling of the SRRs to quantum wells has been shown to occur through the evanescent field of the plasmonic nanostructure and, therefore, decay exponentially with distance [21]. The $1/e$ point for single horseshoe SRR's operating in the 1500nm range has been experimentally and numerically determined to be $\sim 8\text{nm}$ [21]. Second, without a sufficient potential barrier, the exciton wavefunction overlap with surface states will quench the quantum well through decay to non-radiative modes. Another subtle yet important contribution to the overall distance between the quantum well and SRRs is the presence of an InGaAs cap layer. For the case of the quantum wells, the high aluminum content in the barrier materials of InAlAs used for these quantum wells will oxidize quickly when exposed to atmosphere. To combat this

oxidation, thin ~2.3nm InGaAs cap layers were grown. Long wavelength quantum dot or dash samples that are capped with InGaAs do not suffer from oxidation.

Initial near surface growths exhibited unacceptable surface roughness and a large number of long wavelength quantum dot samples were grown with various parameter changes. These parameters included composition proportions of the III-V alloys in combination with growth and dwell temperature variations. The parameter changes were based on the belief that the roughness was induced by large lattice mismatches required for self-assembled dots, with very short distances to grow lattice matched material to smooth the surface.

These long wavelength dots had two basic variants. One variant, we'll call Gibbs dots, was grown on InP wafers with lattice matched AlInAs buffer, InGaAs barriers, and InAs dots on GaAs wetting layers. The second variant followed Enzmann's long wavelength dot/dash growth method, substituting the InGaAs barriers with InGaAs/AlInAs matrices [22].

The Enzmann type dots demonstrated much higher efficiencies from absorption to radiative emission, when compared to the Gibbs dots, approximately 2x in photoluminescence under the same pumping conditions at 10K; see Figure 16-b. However, the Enzmann dots required a much larger barrier to achieve an acceptably smooth surface. A 15nm barrier cap yielded ~2-3nm rms surface roughness with the Enzmann style growth. While growing InAs dots on a GaAs wetting layer with InGaAs barriers yielded as low as

1.78nm RMS surface roughness with a barrier cap of only 4nm on HSG44. As will be shown in the pump probe results of this dissertation, coupling to HSG24, which was an Enzmann type growth, was very low.

3 Metallic Split Ring Resonators

3.1 Fabrication of Metallic Split Ring Resonators Using Electron Beam Lithography and Micro-FTIR Transmission Characterization

The metallic split ring resonator and nano-antennae arrays for the research presented in this dissertation were fabricated by Nina Meinzer and Muriel Bechu, graduate students in the group of Martin Wegner at the Karlsruhe Institute of Technology. The arrays were fabricated onto quantum wells and quantum dash samples grown at the College of Optical Sciences in the group of Professors Galina Khitrova and Hyatt Gibbs. The metallic resonators were fabricated via electron beam lithographic techniques to be outlined here.

Electron beam lithography was the chosen methodology of fabrication for its unmatched flexibility and resolution. The technology allows for direct patterning of structures to sub-10nm resolution with the ability to tune parameters at will [24]. The E-beam consists of a modified scanning electron microscope with computer controlled field steering electron optics and a beam blanker [24,25]. In practice, the high-energy (10-100kV) electrons can

be focused to a spot of $\sim 5\text{nm}$ [23]. To fabricate the desired nano-structures, in this case split ring resonators, the spot is focused onto the surface of the semiconductor samples that have been coated with the positive-tone photoresist PMMA 950k. PMMA is a long-chain polymer positive-tone photoresist, which under exposure to high-energy electrons breaks down. This so called softening of exposed material becomes more soluble than the surrounding unexposed resist. When developed in solvent the written material can be removed, leaving a negative mask of the written structure. Deposition of silver is achieved through electron beam evaporation under high vacuum. The remaining PMMA mask can be lifted off post-silver deposition. Figure 18 demonstrates the E-beam lithographic fabrication described here.

For the split ring resonator fabrication outlined here, the quantum well and quantum dash samples are sectioned into $5 \times 5 \text{ mm}$ areas. The PMMA is spin coated to a thickness of 200nm and heated to 165°C to drive off remaining solvents [25]. Samples were written on a Raith eLine scanning electron microscope (SEM) with dosing densities of $180\mu\text{C}/\text{cm}^2$ at acceleration voltages of 30kV [25]. Taking advantage of the variability of the E-beam technique, dosing parameters are varied by 25% from one array to the next, while holding other parameters constant. This increases the chance of yielding the proper dose on at least one array without the need for multiple fabrication runs. Once exposed, the samples are developed in the selective etch solution of 1:3 methyl-isobutyl ketone/isopropanol for 8s, followed by pure isopropanol for 20s. At pressures of less than $2 \times 10^{-6}\text{mbar}$ silver is E-beam evaporated to a thickness of 30nm [25]. Acetone at 65°C completes the process lift

off to remove the remaining mask. See figure 18.

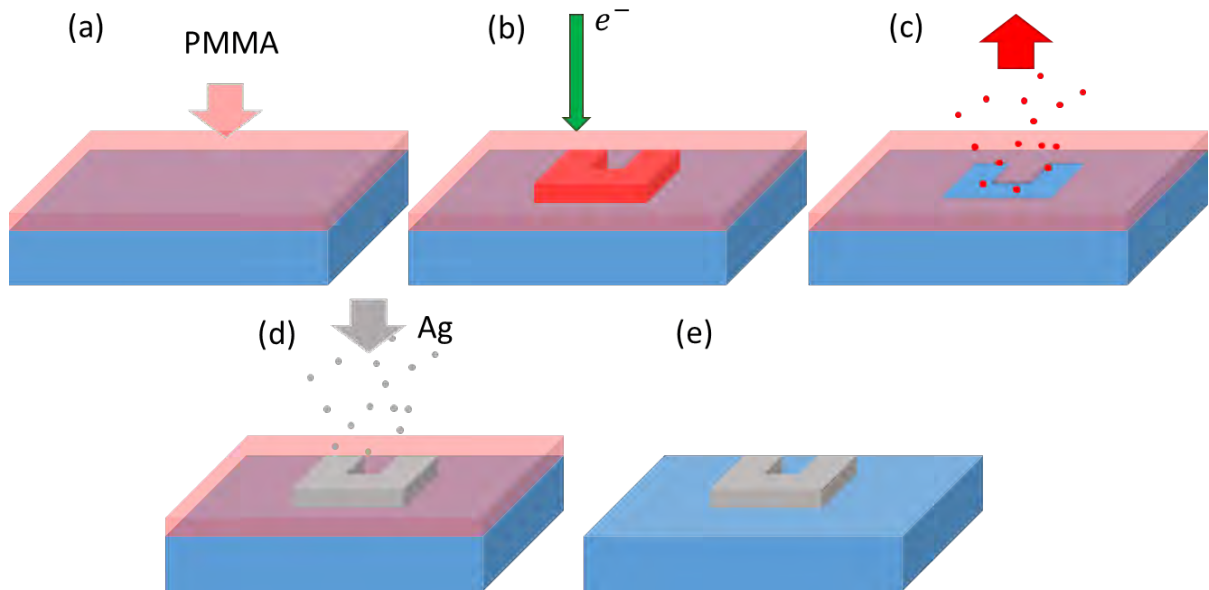


Figure 18
Standard E-beam lithographic fabrication with negative resist material. (a) PMMA is spin coated onto surface of sample. (b) The pattern is written by exposing PMMA with electron beam. (c) The exposed, softened negative resist is removed through selective wet etching. (d) Silver is electron beam evaporated onto the written pattern. (e) Remaining PMMA is removed by hot acetone bath, leaving fabricated SRR's on surface.

The quantum wells and quantum dashes center wavelength can only be tuned by tens of nanometers using temperature tuning from 10-30K; in this case temperature is maintained at 5-10K. Beyond 30K the influence of phonons in the semiconductor broadens excitonic resonances and decreases gain. However, it is desirable to have the ability to tune the resonances of the SRRs and gain structures through one another. Tuning of that nature allows for the experiment to probe how the coupling affects resonance linewidth and intensity. Additionally, one would expect to demonstrate the characteristic anti-crossing curves in the case of strong coupling of the two oscillators. To accomplish this tuning,

length and gap parameters are varied from one array to the next to tune the SRR resonances from $\sim 1200\text{nm}$ to 1800nm . The arrays have a lattice constant $a = 250\text{nm}$, with each individual square array having dimensions $100\ \mu\text{m} \times 100\ \mu\text{m}$ Figure 19.

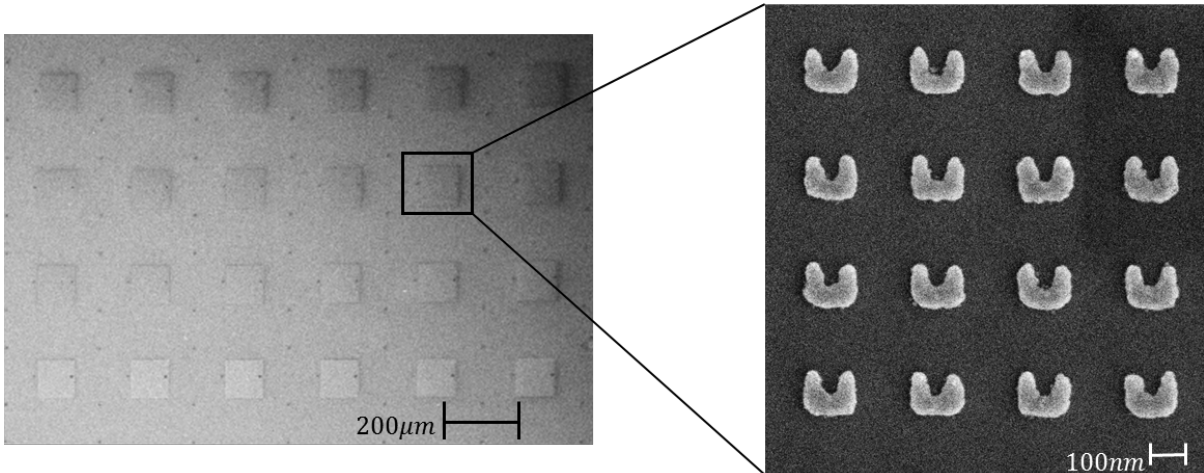


Figure 19
SEM images of HSG24_P array sets and individual SRR

Once fabricated, the individual SRR arrays mode center wavelength and strength were then characterized at room temperature using an FTIR microscope in transmission mode, Figure 25.

4 Femtosecond Temporally and Spectrally Resolved Pump Probe Spectroscopy of Split Ring Resonator and III-V Gain Coupled Systems

4.1 Experimental Design and Apparatus

To investigate the time dynamics of the coupled SRR quantum confined gain structure a

pump probe spectroscopy apparatus was built and implemented. By above band pumping the quantum well at 820nm the excited state can be populated, allowing for gain to occur at the resonance frequency of the well; for example, in the case of HSG37 the gain resonance is centered at 1512nm.

The changes in the gain profile will be detailed later, but for now it should be noted that the gain profile is modified by the coupling of the two oscillators. After the strong pump pulse excites the gain media, a weak probe pulse is then propagated through the sample. If a weak probe pulse is incident on the bare well immediately after the pump pulse, one can imagine that intensity of the probe pulse should increase due to the propagation through the inverted gain media following Lambert's Law $I \propto I_0 e^{gx}$, where I is the intensity, g is the gain coefficient which depends on frequency, and x is the propagation length [26].

Conversely, if the probe pulse is incident on the sample without any inversion the intensity should decrease exponentially with length following Lamberts Law again as $I \propto I_0 e^{-\alpha x}$, with α the absorption coefficient. By experimentally measuring the transmitted pulse ΔT with the strong pump incident on the sample and dividing it by the transmitted pulse T without pumping, we can determine the differential change in transmittance, thereby directly measuring the change in the gain and absorption of the excited sample. By delaying the probe pulse in time with respect to the pump pulse, time dynamic information can be collected. The tuning of the pump pulse also allows the wavelength dependence of the time dynamic information to be collected. An example of one such measurement can be

seen in Figure 26. The system has been characterized to achieve a spectral resolution of 20nm, a temporal resolution of ~140fs, and a $\Delta T/T$ resolution of 0.1%.

The following section is the description of the experimental apparatus design and setup. A diagram of the system can be seen in Figure 20. The laser sources used in the pump probe apparatus were a spectra physics Tsunami Ti:Sa laser coupled to a Spectra Physics OPAL OPO. The Tsunami output was tuned to 820nm with a bandwidth of ~8nm for efficient pumping of the OPO at wavelengths of 1420 nm -1600 nm. The Tsunami and OPO were

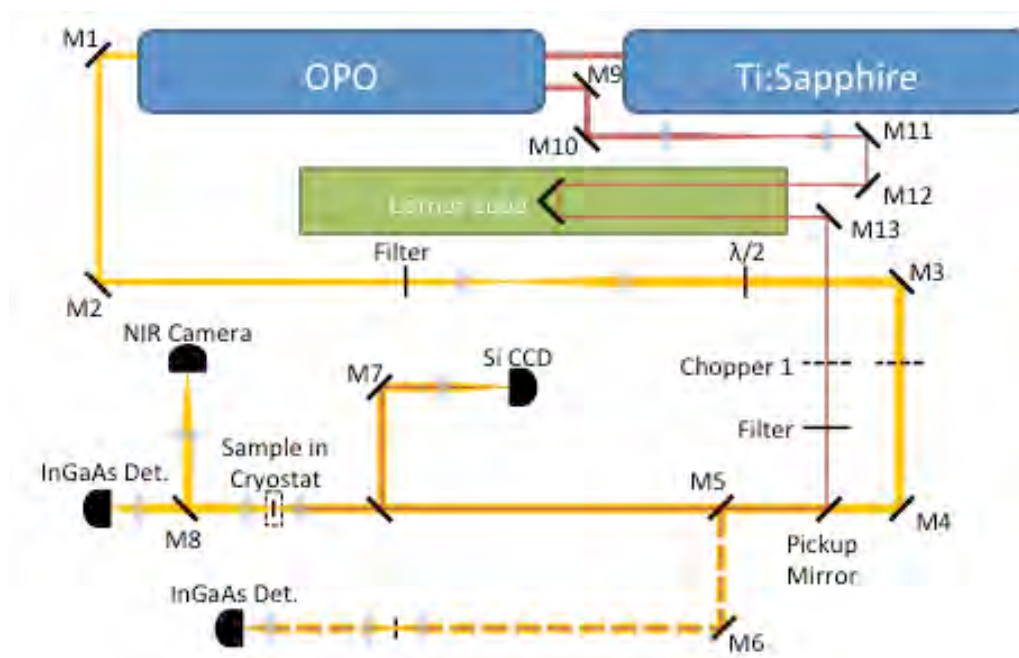


Figure 20
Femtosecond pump probe spectroscopy apparatus. Pump wavelength is tuned to 820nm. Probe pulse can be tuned from 1400nm-1600nm.

electronically frequency locked to 80.000000MHz repetition rates with 130fs pulse lengths. Residual Tsunami pump signal, up to 200mW, was out coupled from the OPO for use as

the pump pulse in these experiments. However, due to losses in the optics of the system, only ~130mW were available for pump pulses at the sample. The OPAL OPO probe pulse width was also ~140fs with a bandwidth of ~20nm. Both the wavelength of the Tsunami and OPAL were directly measured with a calibrated Princeton Instruments SpectraPro500 calibrated spectrometer. The OPO's temperature and wavelength tuning map was tuned at increments of 20nm to ensure stable, reliable probe pulses at all wavelengths across the 1400nm-1600nm range. The excess pump power exiting the OPO was directed into a two-lens collimator with focal lengths $L1 = 150\text{mm}$ and $L2 = 50\text{mm}$ to control collimation and spot size on the sample while also reducing the collimated diameter by ~3X. After passing through the collimating optics the beam was precision aligned into a double pass motorized delay line. This delay line consisted of a computer controlled stepper motor screw driven stage (Daedal 1m) with two corner cubes mounted to the shuttle. The pump pulse was directed from the delay line through an optical chopper SRS model 540 set to 400Hz. The pump beam was combined with the probe beam with the use of a dichroic pickup mirror from Semrock LP02-980RE-25. The probe pulse also passed through a two lens collimator, in this case to expand the beam, $L3 = 35\text{mm}$ and $L4 = 10\text{mm}$. To rotate the polarization of the probe beam, a Newport Model 5540 Berek waveplate was used. In order to produce a highly polarized beam a Thorlabs Glan-Thomson Model GT15 with an extinction ratio of 100,000:1 was added after the waveplate. The focusing and collection optics at the sample were both identical lenses with focal lengths of 5cm. Collected signal was filtered with Schott RG1000 filter glass to remove any unabsorbed pump light with attenuations of 7 orders of magnitude at 820nm. The filtered, collected signal could then be directed into a

near infrared (NIR) camera or a single channel Thorlabs InGaAs detector with a 2.5cm focusing optic. The NIR camera in the transmission arrangement was a crucial imaging step to ensure that pump, probe, and collection optics were focused onto the SRR arrays. The imaging Si CCD in the reflection arrangement assisted in finding proper arrays and rough alignment of the pump and probe beam due to its superior resolution to the NIR camera and viewing the sample front fabricated surface. The image was reflected towards the Si CCD with a Pellicle beam splitter on a flip mount so that it could be removed from the beam path during pump probe measurements.

Rough co-linearity alignments were achieved using a pinhole in two positions, one very near the pickup mirror (PM) and one very near the sample cryostat. Once rough alignment was completed the co-linear beams are reflected to a secondary leg with the exact same path length as the experimental path via a flip mirror. This path was identical to the experimental path with a small pinhole substituted for the sample. This scheme was used to precision align the beams co-linearity and for alignment of the delay line. The relative intensity on the detector was tracked and the delay line was translated to maximum travel limits, more than 3X the needed travel for the time periods measured here. A pinhole was also attached to motorized stages such that knife edge beam waist measurement techniques could be used to measure the spot size of both pump and probe pulses, ensuring that the probe was incident on a uniformly pumped area.

The samples were mounted in an ARS closed cycle Helium Cryostat and cooled to 10K. The cryostat sample compartment was pulled to vacuum pressures of $\sim 30\mu\text{Torr}$ using a

Varian TPS turbo pump system. The samples were mounted at angle of $\sim 13^\circ$ degrees to eliminate pump pulses reflected off the back surface of the sample. It was found that the reflected pump introduced a secondary pump delayed in time to the probe location. Spot sizes of the probe and pump beams were $10\mu\text{m}$ and $20\mu\text{m}$, respectively.

4.2 Two Level Coupled Oscillator Model for Plasmonic Metamaterial Resonance and Two-Level Gain System

A simple coupled oscillator model is used to fit the dT/T data presented in this dissertation. The model outlined here is that of reference [39]. This model while not a comprehensive physical model of the system, still provides useful insight into the behavior of the coupled system. Despite its simplistic approach the model provides for very good fits to experimental data. The simplistic model is also in good agreement with full FDTD three dimensional Maxwell Equation solutions [39]. Beginning with the external electric field written as

$$E(t) = E_o \cos(\omega t) = \frac{E_o}{2} (\exp(-i\omega t) + c. c.)$$

and noting the local electric field of the two level system is $E = E + LP_{pl}$ and the local electric field of the plasmonic system is $E = E + LP_{2LS}$. Here, L is phenomenological constant related to the coupling and P is the polarization of the of the plasmonic system and 2 level system respectively [39]. The Bloch equations for the 2 level system are arranged as follows.

$$\begin{aligned} \dot{p}_{2LS} + (i\Omega_{2LS} + \gamma_{2LS})p_{2LS} &= i\hbar^{-1}d_{2LS}E(1 - 2f) \\ \dot{f} + \Gamma_{2LS}f &= i\hbar^{-1}(p_{2LS}^*d_{2LS}E - p_{2LS}d_{2LS}^*E^*) \end{aligned}$$

Above, p_{2LS} is the complex transition amplitude, f is the occupation probability of the upper level, d_{2LS} is the dipole matrix element, Ω_{2LS} is the transition frequency and γ_{2LS} is the damping rate, all referring to the 2 level system [39]. The corresponding Bloch equations of the plasmonic system are

$$\dot{p}_{pl} + (i\Omega_{pl} + \gamma_{pl})p_{pl} = i\hbar^{-1}d_{pl}E$$

$$\dot{f} + \Gamma_{pl}f = i\hbar^{-1}(p_{pl}^*d_{pl}E - p_{pl}d_{pl}^*E^*)$$

The transition amplitudes $p = \tilde{p}\exp(-i\omega t)$ can be derived and found to be

$$\tilde{p}_{2LS} = \frac{(1 - 2f) \left(\hbar^{-1}d_{2LS} \frac{\tilde{E}_o}{2} + \frac{V_{2LS}\hbar^{-1}d_{pl} \frac{\tilde{E}_o}{2}}{(\Omega_{pl} - \omega) - i\gamma_{pl}} \right)}{(\Omega_{2LS} - \omega) - i\gamma_{2LS} - (1 - 2f) \frac{V_{pl}V_{2LS}}{(\Omega_{pl} - \omega) - i\gamma_{pl}}}$$

$$\tilde{p}_{pl} = \frac{\hbar^{-1}d_{pl} \frac{\tilde{E}_o}{2} + V_{pl}\tilde{p}_{2LS}}{(\Omega_{pl} - \omega) - i\gamma_{pl}}$$

with

$$V_{2LS} = \hbar^{-1}d_{2LS}LN_{pl}d_{pl}$$

$$V_{pl} = \hbar^{-1}d_{pl}LN_{2LS}d_{2LS}$$

Here, N is the volume density of the 2 level system and plasmonic mode respectively [39].

Using the Maxwell Garnett approach as an approximation of the system, the Linear susceptibility, χ can be found from the following equation (l_{2LS} and l_{pl} are the film thicknesses of the 2 level and plasmonic systems respectively)

$$P = \frac{l_{2LS}}{l_{2LS} + l_{pl}}P_{2LS} + \frac{l_{pl}}{l_{2LS} + l_{pl}}P_{pl} = \varepsilon_o\chi \frac{\tilde{E}_o}{2} \exp(-i\omega t) + c. c.$$

in combination with the macroscopic polarization $P_{2LS} = N_{2LS}d_{2LS}p_{2LS} + c. c.$, for the 2 level system. The macroscopic polarization for the plasmonic system identical in form [39]. Electromagnetic theory gives the transmission coefficient as

$$t(\omega) = \frac{2}{(1 + z_r) \cos(\phi) - i(z_r z + z^{-1}) \sin(\phi)}$$

with $z_r = n_s/n_i$, the substrate and incident indexes respectively, $Z = n_i/n(\omega)$, and $\phi(\omega) = \omega n(\omega) d/c_o$ [40]. The transmission is then found from

$$T = \frac{n_s}{n_i} |t(\omega)|^2$$

For a given system the parameters used in the above equations $\omega_{2LS}, \omega_{pl}, \gamma_{2LS}, \gamma_{pl}, N_{2LS}, N_{pl}, L_{2LS}, L_{pl}, d_{2LS}, d_{pl}, f, n_s$, and n_i are properties of the materials in the system and are therefore essentially constants. The only parameter left to adjust for fitting of data is the phenomenological parameter L. The dT/T data for the coupled system is generated by calculating the transmission on the SRR array with the gain material in the ground state (un-pumped) with $f = 0$, repeating the same calculation with $f = 1$, subtracting the two curves and then dividing by the curve with $f = 0$. To calculate the system response with no coupling the parameter L is set to zero.

4.3 Temporally and Spectrally Resolved Results of Ag SRR Arrays and Quantum Wells

Nina Meinzer in the German group at KIT took the first data on SRRs coupled to quantum wells on the HSG37 sample. Their results showed $\Delta T/T$ of up to -8% on some arrays

fabricated at 1480nm Figure 21.

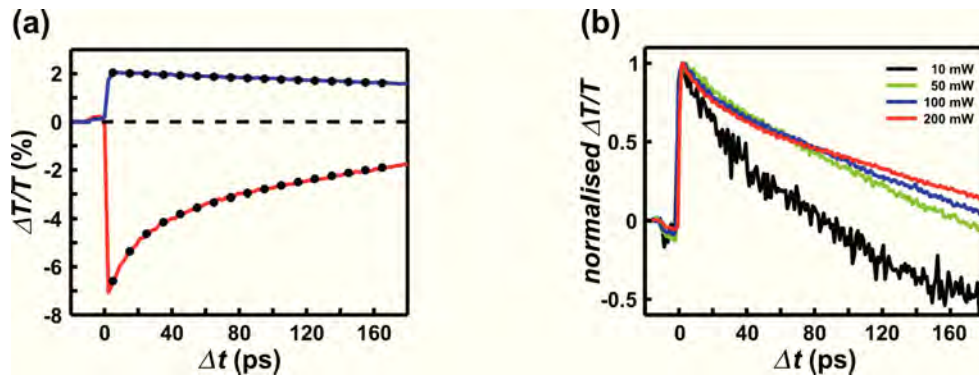


Figure 21

Differential transmittance of NA1 sample fabricated on HSG37 with probe tuned to 1480nm. These samples were later reexamined in the Tucson apparatus and, while similar results were found, it appeared that some aging had occurred. No longer could the differential transmittance of -8% be seen, it had been reduced to -2.0% maximum $\Delta T/T$. However, the wavelength peak negative $\Delta T/T$ had shifted from 1480nm to 1540nm indicating that the SRRs had changed in some way. We attribute this to oxide layers forming over time on the Ag SRRs, causing a shift in SRR resonance, while the QW remained resonant at 1500nm.

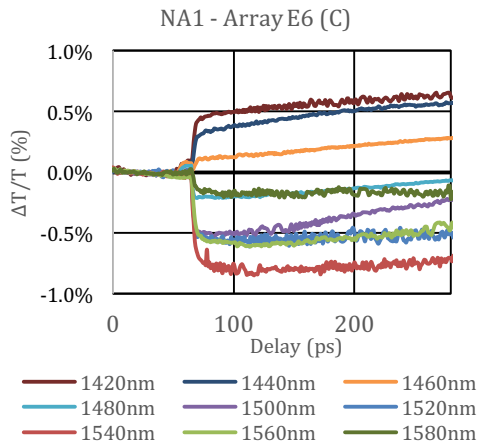


Figure 22

Differential transmittance of SRR sample NA1 array E6 fabricated on HSG37, measured on Tucson apparatus

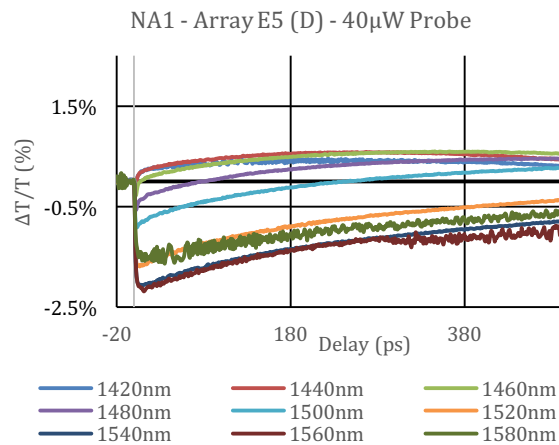


Figure 23

Differential transmittance of SRR sample NA1 array E5 fabricated on HSG37, measured on Tucson apparatus.

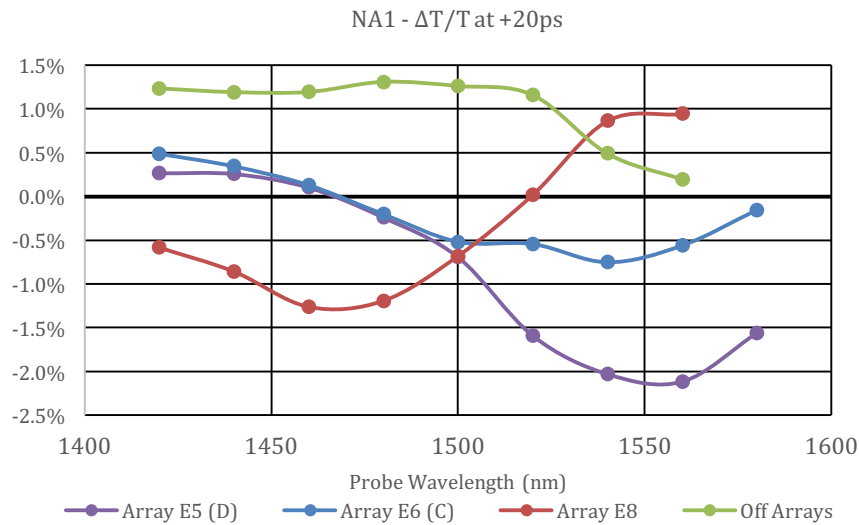


Figure 24
 Maximum Differential transmittance measured at $t = 20$ ps for 3 arrays, E5, E6, E8 and off array vs wavelength.

4.4 Temporally and Spectrally Resolved Results of Ag SRR Arrays and Long Wavelength Quantum Wires

Our research group has a large amount of past experience with Purcell enhancement and coupled oscillators [27,28,29]. The first demonstrations of coupled quantum well SRR were shown to demonstrate Purcell enhanced emission [6]. With those results it was a natural decision then to pursue coupling of SRRs to ever more confined semiconductor nanostructures. The next step after quantum well coupling was to attempt to demonstrate coupling between long wavelength quantum wire or dash samples. HSG24 was grown with the quantum dash first excited state PL peak at 1447nm. SRR arrays were fabricated with tunings from 1350nm to 1600nm on the surface of that sample. The SRRs resonances were characterized and mapped using micro-FTIR and pump probe spectroscopy was performed

on many arrays. Some examples of arrays on HSG24_P are shown below in Figure 25.

Two conditions are of interest in selecting an array for pump probe investigations. The first is simple, it requires that a strong resonance exists. In this case we look for arrays with ~50% or greater absorption in micro-FTIR spectra. The second condition is that the center wavelength of the array resonance is close to the center of the quantum gain material resonance. For HSG24 that resonance is ~1450nm and is shown as the black normalized curve on the bottom of Figure 25. Per those requirements arrays C12 and C13 should prove good candidates for the observation of coupling effects.

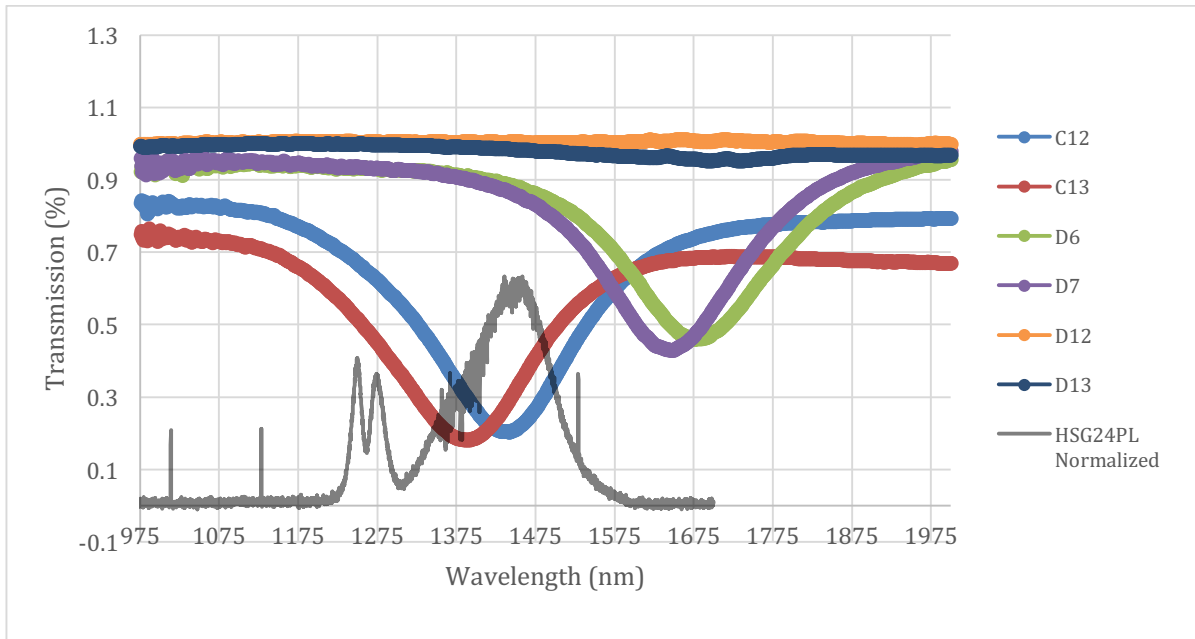


Figure 25

FTIR micro transmission of several arrays from HSG24_P SRR sample. The black spectrum plotted on the bottom of the chart is the normalized photoluminescence spectrum of the HSG24 quantum dash emission and is presented to demonstrate the spectral location relative to the various SRR array resonances.

C12 was selected for pump probe $\Delta T/T$ measurements and the results are presented in

Figure 26. The differential transmittance shows the same characteristics as that of the quantum well SRR sample NA1 fabricated on HSG37. The red curve in each spectra is again when the polarization is horizontal and the SRR resonance is active, while the blue curve is taken with the probe polarization rotated 90 degrees in the vertical orientation such that the resonance is essentially turned off. Each curve in Figure 26 consists of a constant wavelength while the probe is delayed in small steps of 100fs relative to the pump. As the probe wavelength is scanned across the SRR resonance the differential transmittance changes sign.

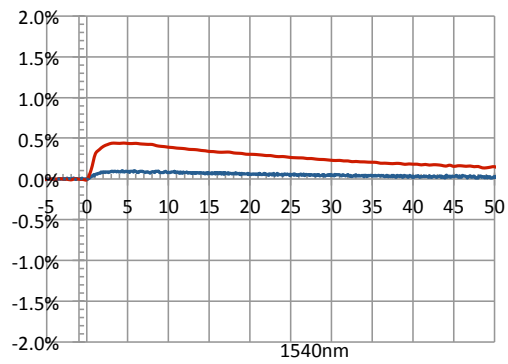
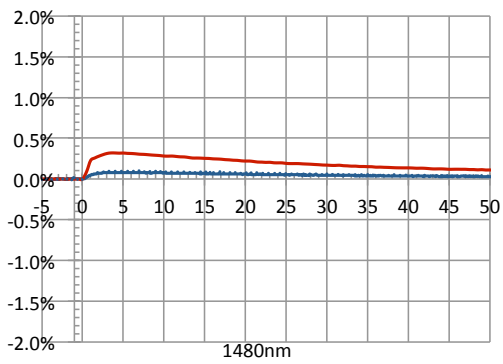
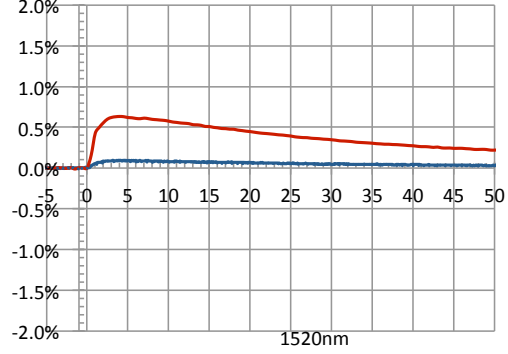
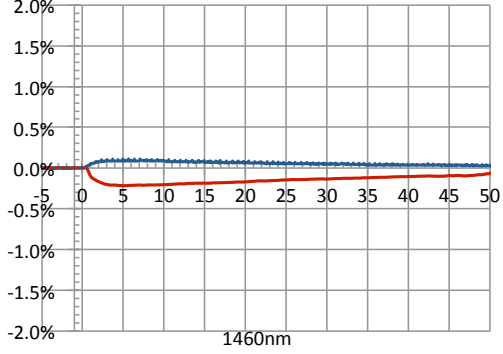
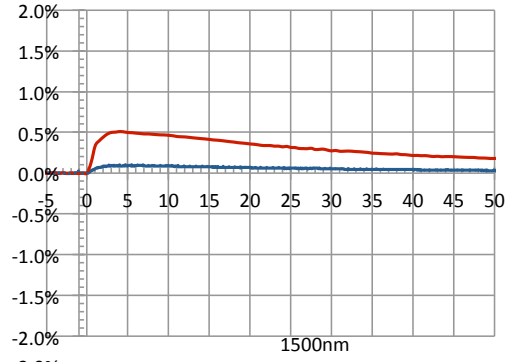
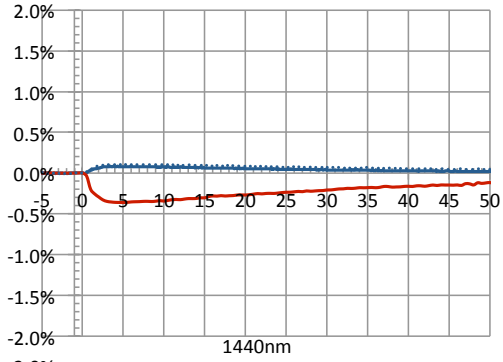
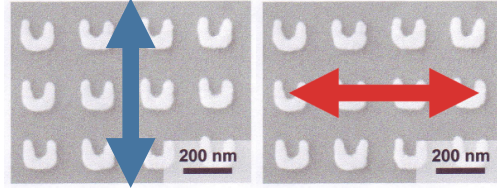
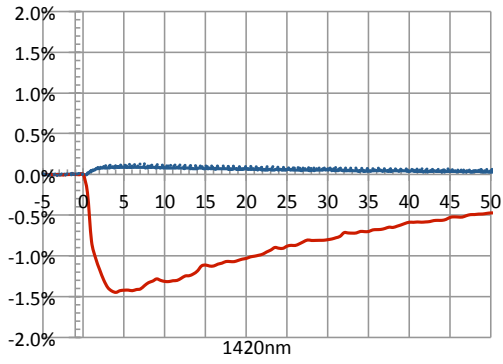


Figure 26

Differential transmittance $\Delta T/T$ of HSG24_P array C12. Red curves were recorded with the probe horizontally polarized on array and therefore resonant with the SRR modes. Blue curves were recorded with the probe vertically polarized on array and not resonant with the SRR. Also recorded was off array $\Delta T/T$ which is not presented in the plots but would overlap the blue curves presented here.

These curves can be fit with a simple two-coupled oscillator toy model following section

4.2, Figure 27. The parameters used in the model were as follows; $\Omega_{2LS} =$

$2\pi \times 206.75 \text{ THz}$, $\gamma_{2LS} = 50 \text{ THz}$, $d_{2LS} = 9.59 \times 10^{-29} \text{ m}^{-3}$, $N_{2LS} = 4.79 \times 10^{22} \text{ m}^{-3}$,

$L_{2LS} = 3 \times 10^{-9} \text{ m}$, $\Omega_{PL} = 2\pi \times 208 \text{ THz}$, $\gamma_{PL} = 90 \text{ THz}$, $d_{PL} = 4.2 \times 10^{-26}$, $N_{PL} =$

5.3×10^{20} , $L_{PL} = 30 \times 10^{-9} \text{ m}$.

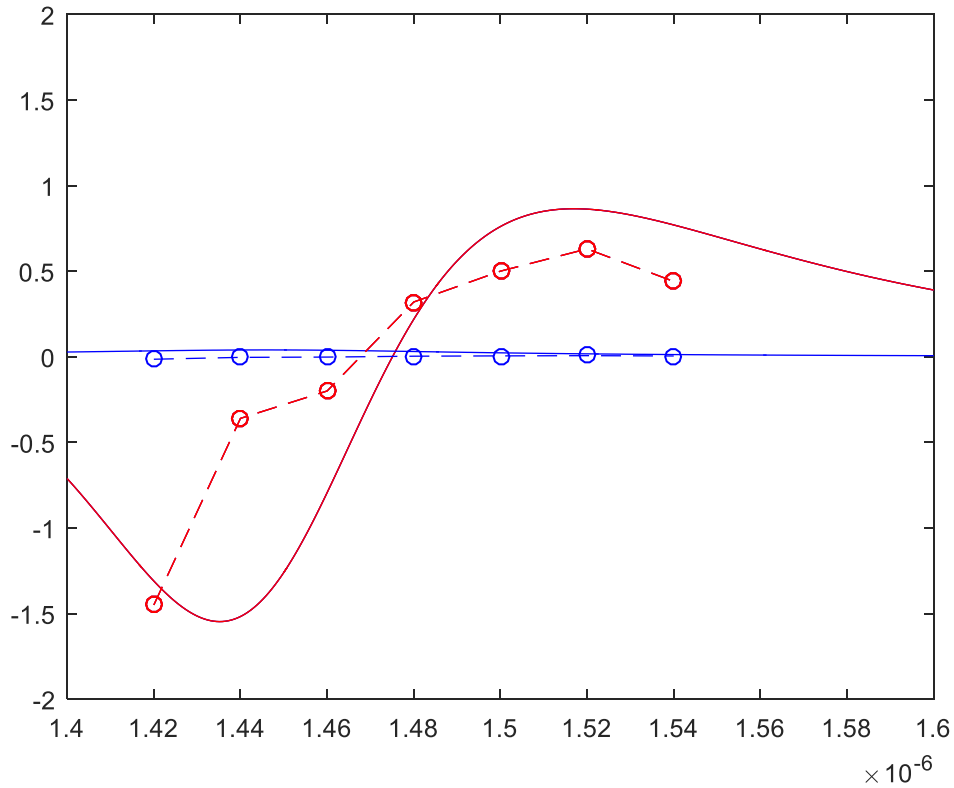


Figure 27

Toy Model two-coupled oscillator fit of the maximum $\Delta T/T$ of HSG24_P array C12. Dashed curves are the experimentally measured results where red and blue are horizontally and vertically polarized probes respectively. The solid curves are the two-coupled oscillator calculated results.

5 Future Directions and State of the Art

This is the first demonstration of quantum dash structures coupled to a split ring resonator array and leaves much to be explored. One can see that significant enhancement of the differential transmittance occurs in both the negative and positive regions of $\Delta T/T$. In the case of coupling to the quantum well positive enhancement was minimal, which suggests that interesting physics might be found upon further investigations. However, it should be noted that this difference in enhancement characteristics is fairly well described by the simple two-coupled oscillator model.

The research group at the College of Optical Sciences has a great deal of experimental familiarity with Purcell enhancement of semiconductor nanostructures, specifically single quantum dots coupled to optically resonant nano-cavities. With the demonstration of Purcell enhancement of quantum well oscillator through the coupling interactions with split ring resonator arrays, and now the demonstration of coupling between split ring resonator and quantum dash samples, it is very natural to pursue investigations to achieve nano-antennae or SRR Purcell enhanced single quantum dots for a number of reasons.

The Arizona group in 2004 demonstrated Vacuum Rabi Splitting with a single quantum dots coupled to a semiconductor photonic crystal slab nano-cavity [28]. The interesting physics here could likely be demonstrated again in a new material system by demonstrating

strong coupling between a single quantum dot and a plasmonic split ring resonator cavity. Several advantages to this arrangement from an experimental and application standpoint make this an exciting proposal.

In the case of the quantum dot photonic crystal system a quantum dot must be spectrally resonant with the nano-cavity, while also spatially aligned with an antinode of the cavity. This turns out to be a low probability process due to the requirement of narrow linewidth cavities and the random distribution of quantum dots. The requirement for strong coupling is that the Rabi splitting 2Ω must exceed the decay rates of the cavity κ and of the dot γ , with $\Omega = \mu E_{vac}/\hbar$, and the vacuum field satisfying $n^2 \epsilon_o |E_{vac}|^2 V = \hbar \nu / 2$ [28,30]. κ generally exceeds γ and $\Omega/\kappa \propto Q/\sqrt{V}$.

The strong coupling that was demonstrated by the Arizona group was done so with mode volume of $\approx 0.04 \mu\text{m}^3 \approx (\lambda_o/n)^3$ [28]. The challenge then was to fabricate cavities with Q's of > 6000 . Progress in growth and fabrication, later yielded higher Q cavities on a more regular basis, but never achieved the computational results that Si cavities were able to achieve [31,32,33]. This requirement and effort towards ever higher Q's yields extremely narrow cavity linewidths. The quantum dots used in those experiments and also the quantum dot and dash samples presented in the research here are all of the self-assembled strain induced type. An average self-assembled InAs quantum dot has a linewidth of $\sim 1\text{nm}$ and a center wavelength dependent on size. The size of these dots is a random distribution and for an average sample with a density of $\sim 200\text{-}300 \mu\text{m}^{-2}$ has an ensemble bandwidth of $\sim 100\text{nm}$ Figure 14. These factors create a condition of high probability that the QD and the

cavity spectral resonance will have large detunings. In addition, the QD must physically be located at the antinode of the cavity; see Figure 28 which demonstrates a false color FDTD electric field calculation to illustrate the anti-node locations.

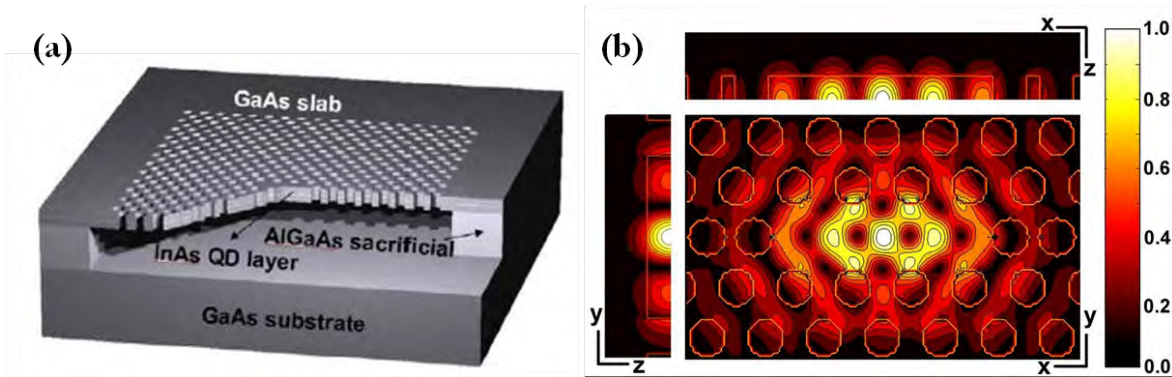


Figure 28
 (a) Structure diagram of a photonic crystal slab nano-cavity with a quantum dot layer (b) FDTD simulation of the electric field profile of a photonic crystal slab nano-cavity.

While one can search thousands of cavities to find a QD and cavity that satisfy the necessary conditions for a purely science based investigation, this arrangement would yield poor results for useful devices. Work has been done in the Arizona group towards selective site growth of InAs quantum dots. However, QD coupling and photonic crystal slab nano-cavity fabrication has not been successful using this selective site approach [35].

To the contrary, the SRR resonances are very broad with Q's of ~ 10 . However, due to the extremely small mode volumes of some of the single SRR modes the important Q/V factor can be equal to or possibly exceed that of the L3 cavity [36]. This ability to easily couple spectrally with similar Purcell enhancement factors means that any Quantum confined nanostructure that lies in the antinode of the plasmonic structure's E-field will be coupled

and the emission characteristics modified. This opens the door to a variety of interesting devices and device physics experimentation, such as nanoscale microscopy, quantum optics for single photon sources, photovoltaics with higher efficiencies, and other exciting directions as well [37].

6 Appendix Journal Publications

Arrays of Ag split-ring resonators coupled to InGaAs single-quantum-well gain

Nina Meinzer,^{1,2,*} Matthias Ruther,^{1,2} Stefan Linden,^{1,2} Costas M. Soukoulis,³
Galina Khitrova,⁴ Joshua Hendrickson,⁴ Joshua D. Olitzky,⁴ Hyatt M. Gibbs,⁴
and Martin Wegener^{1,2}

¹Institut für Nanotechnologie, Karlsruhe Institute of Technology (KIT),
Postfach 3640, D-76021 Karlsruhe, Germany

²Institut für Angewandte Physik and DFG-Center for Functional Nanostructures (CFN),
Karlsruhe Institute of Technology (KIT), D-76128 Karlsruhe, Germany

³Ames Laboratory and Department of Physics and Astronomy, Iowa State University, Ames, Iowa 50011, U.S.A., and
Research Center of Crete, and Department of Materials Science and Technology, 71110 Heraklion, Crete, Greece

⁴College of Optical Sciences, The University of Arizona, Tucson, AZ 85721, USA

*Nina.Meinzer@kit.edu

Abstract: We study arrays of silver split-ring resonators operating at around 1.5- μm wavelength coupled to an MBE-grown single 12.7-nm thin InGaAs quantum well separated only 4.8 nm from the wafer surface. The samples are held at liquid-helium temperature and are pumped by intense femtosecond optical pulses at 0.81- μm center wavelength in a pump-probe geometry. We observe much larger relative transmittance changes (up to about 8%) on the split-ring-resonator arrays as compared to the bare quantum well (not more than 1-2%). We also observe a much more rapid temporal decay component of the differential transmittance signal of 15 ps for the case of split-ring resonators coupled to the quantum well compared to the case of the bare quantum well, where we find about 0.7 ns. These observations are ascribed to the evanescent coupling of the split-ring resonators to the quantum-well gain. All experimental results are compared with a recently introduced analytical toy model that accounts for this evanescent coupling, leading to excellent overall qualitative agreement.

©2010 Optical Society of America

OCIS codes: (160.4760) Optical properties; (260.5740) Resonance; (160.3918) Metamaterials.

References and links

1. V. M. Shalaev, "Optical negative-index metamaterials," *Nat. Photonics* **1**(1), 41–48 (2007).
2. C. M. Soukoulis, S. Linden, and M. Wegener, "Physics: Negative refractive index at optical wavelengths," *Science* **315**(5808), 47–49 (2007).
3. K. Busch, G. von Freymann, S. Linden, S. F. Mingaleev, L. Tskhelashvili, and M. Wegener, "Periodic nanostructures for photonics," *Phys. Rep.* **444**(3-6), 101–202 (2007).
4. J. B. Pendry, "Negative refraction makes a perfect lens," *Phys. Rev. Lett.* **85**(18), 3966–3969 (2000).
5. D. Schurig, J. J. Mock, B. J. Justice, S. A. Cummer, J. B. Pendry, A. F. Starr, and D. R. Smith, "Metamaterial electromagnetic cloak at microwave frequencies," *Science* **314**(5801), 977–980 (2006).
6. D. J. Bergman, and M. I. Stockman, "Surface plasmon amplification by stimulated emission of radiation: quantum generation of coherent surface plasmons in nanosystems," *Phys. Rev. Lett.* **90**(2), 027402 (2003).
7. T. A. Klar, A. V. Kildishev, V. P. Drachev, and V. M. Shalaev, "Negative-Index Metamaterials: Going Optical," *IEEE J. Sel. Top. Quantum Electron.* **12**(6), 1106–1115 (2006).
8. J. A. Gordon, and R. W. Ziolkowski, "The design and simulated performance of a coated nano-particle laser," *Opt. Express* **15**(5), 2622–2653 (2007).
9. A. A. Gomyadinov, V. A. Podolskiy, and M. A. Noginov, "Active metamaterials: Sign of refractive index and gain-assisted dispersion management," *Appl. Phys. Lett.* **91**(19), 191103 (2007).
10. M. I. Stockman, "Criterion for Negative Refraction with Low Optical Losses from a Fundamental Principle of Causality," *Phys. Rev. Lett.* **98**(177404), 1–4 (2007).
11. P. Kinsler, and M. W. McCall, "Causality-based criteria for a negative refractive index must be used with care," *Phys. Rev. Lett.* **101**(16), 167401 (2008).
12. N. I. Zheludev, S. L. Prosvirnin, N. Papasimakis, and V. A. Fedotov, "Lasing spaser," *Nat. Photonics* **2**(6), 351–354 (2008).
13. J. A. Gordon, and R. W. Ziolkowski, "CNP optical metamaterials," *Opt. Express* **16**(9), 6692–6716 (2008).

#134264 - \$15.00 USD Received 30 Aug 2010; revised 6 Oct 2010; accepted 22 Oct 2010; published 3 Nov 2010
(C) 2010 OSA 8 November 2010 / Vol. 18, No. 23 / OPTICS EXPRESS 24140

14. M. Wegener, J. L. García-Pomar, C. M. Soukoulis, N. Meinzer, M. Ruther, and S. Linden, "Toy model for plasmonic metamaterial resonances coupled to two-level system gain," *Opt. Express* **16**(24), 19785–19798 (2008).
15. A. Fang, Th. Koschny, M. Wegener, and C. M. Soukoulis, "Self-consistent calculation of metamaterials with gain," *Phys. Rev. B* **79**(241104), 1–4 (2009).
16. E. Plum, V. A. Fedotov, P. Kuo, D. P. Tsai, and N. I. Zheludev, "Towards the lasing spaser: controlling metamaterial optical response with semiconductor quantum dots," *Opt. Express* **17**(10), 8548–8551 (2009).
17. S. Xiao, V. P. Drachev, A. V. Kildishev, X. Ni, U. K. Chettiar, H.-K. Yuan, and V. M. Shalaginov, "Loss-free and active optical negative-index metamaterials," *Nature* **466**(7307), 735–738 (2010).
18. K. Tanaka, E. Plum, J. Y. Ou, T. Uchino, and N. I. Zheludev, "Multi-fold Enhancement of Quantum Dot Luminescence in a Plasmonic Metamaterial", arXiv:1008.4770 (2010).

1. Introduction

At near-infrared and visible frequencies, losses of metal-based optical metamaterials are very large due to the fact that the intrinsic free-electron metal losses increase drastically when even remotely approaching the metal plasma frequency (see, *e.g.*, the reviews [1–3]). For many of the envisioned applications of metamaterials such as in perfect lenses [4] or in transformation optics [5], low-loss or even zero-loss metamaterials are required. Theoretical calculations have shown that introducing optical gain is a possible remedy [6–15].

So far, to the best of our knowledge, only two experiments [16,17] along these lines have been published. Ref. 16 has used an approximately 1- μm thick film of 3.2-nm diameter PbS quantum dots spun onto an array of complementary split-ring resonators (with two slits) operating at around 1.0- μm wavelength. At room temperature and upon continuous-wave optical pumping, they observe induced transmittance changes on the order of 1% [see their [16] Fig. 2(d)]. Ref. 17 has employed Rh800 dye molecules embedded in an epoxy filled into a double-fishnet-type negative-index metamaterial operating at around 0.7- μm wavelength. They measure an increased relative transmittance on the order of 100% [see their [17] Fig. 3(b)] upon pulsed optical pumping at room temperature and infer zero loss at some wavelength by comparison with detailed numerical calculations [17].

In the present work, we focus on optically-pumped epitaxially-grown single 12.7-nm thin InGaAs semiconductor quantum wells in close proximity to a layer of 30-nm thin silver splitting resonators operating at around 1.5- μm wavelength. To maximize the optical gain, we cool the samples to helium temperature. We use semiconductor quantum wells because they open perspectives towards electrical carrier injection and because they are long-term photo-stable – in sharp contrast to, *e.g.*, dye molecules.

Before turning to our experiments, we would like to provide an intuitive qualitative discussion of what effects can be expected. In this discussion, the coupling strength between a metamaterial layer and the gain is a determining factor. We start our reasoning with the case of no coupling and continue towards weak and strong coupling.

To illustrate the limit of no coupling, let us consider a metamaterial layer and a gain medium separated by the absurd distance of one meter. It is clear that losses can be compensated in this fashion. However, this system can hardly be considered as one material and this geometry would not solve the problems mentioned above. It is interesting to note (and relevant for some of the controls in Section 3) that this uncoupled arrangement would always lead to increased transmittance once the gain material is optically pumped. In fact, one would obtain exactly the same differential transmittance change, $\Delta T/T$, with and without the metamaterial, respectively, at any wavelength. For example, if the metamaterial itself transmits 10% of the light and the gain material transmittance changes from 100% to 101% upon optical pumping, the differential transmittance change is $\Delta T/T = 1\%$ with and without the lossy metamaterial (*i.e.*, without metamaterial, the overall system transmittance T changes from 100% to 101%; with metamaterial it changes from 10.0% to 10.1%).

This gedankenexperiment makes clear that a coupling between metamaterial layer and gain material is absolutely crucial for success. Coupling in the spirit of a metamaterial can only be achieved if the two structures are not separated by more than the decay length of the evanescent electromagnetic fields – typically 10-20 nm for our conditions.

In the case of weak coupling *via* the evanescent fields, the two resonances do get mixed (or hybridized) to some extent, yet addressing them by their original names remains meaningful. Here, the overall transmittance change results from coupling two competing contributions: First, the gain resonance again leads to an increase of transmittance over the spectral range of the gain upon optical pumping. Second, the metamaterial resonance (specifically, we consider a spectral transmittance minimum) leads to reduced transmission over a wider range. Which of these two contributions dominates depends on the relative strengths of the two resonances. For the case of a weak gain resonance (that is relevant in the present paper), the coupling of these two leads to reduced transmittance at the common resonance frequency position and increased transmittance on the two spectral sides. This reasoning, however, is still a bit too naive because a change in gain, hence in the imaginary part of the gain-material refractive index, is necessarily accompanied by a change in the real part of the gain-material refractive index *via* the Kramers-Kronig relations (resulting from causality). Thus, one additionally expects spectral shifts, which are again accompanied by spectral regions of reduced transmittance.

In the case of strong coupling between the two resonances *via* the evanescent fields, the resonances completely lose their original identity. One expects avoided crossings and generally Fano-type resonance lineshapes, including the possibility of complete loss compensation at specific frequencies.

All of the above aspects and limits are included in a simple analytical toy model that has been introduced two years ago [14]. This toy model considers (on a self-consistent footing) two coupled resonances, a Lorentzian resonance of the metamaterial and a second Lorentzian resonance that can be inverted, delivering the gain. The relevance of this toy model to the problem under discussion has explicitly been shown in [14]. We will use this analytical model in Section 4 to fit to our experimental data. It is clear that this toy model leaves lots of space for future improvements regarding theoretical modeling, but it would be very difficult to actually fit a complete numerical model to the vast experimental data to be presented below.

2. Definition of the experiment

The samples in our experiments are fabricated by standard electron-beam lithography on single-crystalline semiconductor wafers that have been grown by molecular-beam epitaxy (MBE) on semi-insulating InP substrates. We choose an operation wavelength at around 1.5 μm because metal losses are already an issue there but losses are not yet as bad as in the visible regime. Our design is the result of investigating several dozens of wafers (single and multiple quantum wells) that we have grown and characterized (and that will not be shown here). For positioning the gain material, one must appreciate that the evanescent fields of split-ring resonators operating at this wavelength and located on such high-refractive-index substrates decay on a scale of 10-20 nm normal to the wafer surface. This number has been obtained from numerical calculations (not shown). This decay length obviously limits the possible thickness of the gain material. The position of the single QW results from a trade-off: On the one hand, the QW should be close to the surface to maximize the coupling to the SRR *via* the evanescent fields. On the other hand, the QW should be sufficiently far away from the surface to prevent evanescent coupling to non-radiative modes ("quenching") or deterioration of the QW optical properties due to substantial overlap of the QW exciton wavefunction with the wafer surface. Furthermore, to prevent oxidation of the AlInAs top barrier, it must be capped with a layer of InGaAs. The barrier plus caplayer necessitate a minimum separation of the QW from the wafer surface of about 5-10 nm.

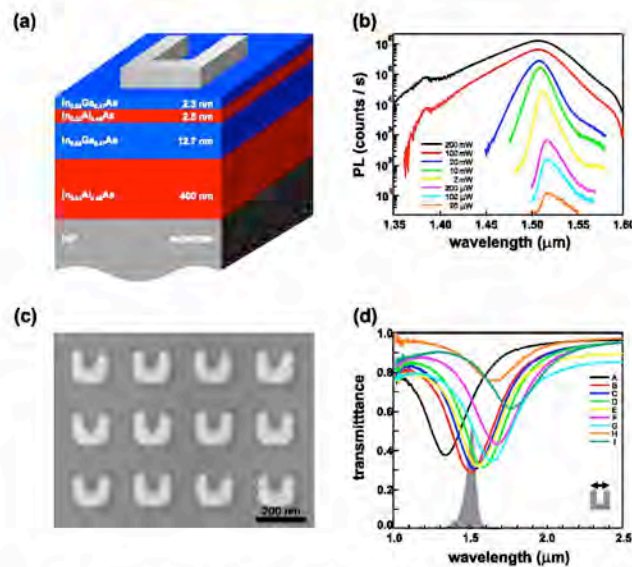


Fig. 1. (a) Layer sequence (not to scale) and composition of the semiconductor crystal structure grown by molecular-beam epitaxy (MBE), lattice-matched to the InP substrate. After MBE growth, arrays of 30-nm thin Ag split-ring resonators (SRR) are fabricated on top of this wafer using a standard electron-beam-lithography process. (b) Low-temperature quantum well photoluminescence (PL) spectra for increasing power, P , of the exciting femtosecond Ti:sapphire laser at 0.81- μm center wavelength as indicated. In the pump-probe experiments depicted in Figs. 2-4, we have used the identical laser with $P = 200$ mW under identical focusing conditions. (c) Electron micrograph of SRR array "D". (d) Optical normal-incidence linear intensity transmittance spectra of some of the SRR arrays used in this work (horizontal linear incident polarization of light) taken at room-temperature. The gray area corresponds to the low-temperature PL spectrum of the bare QW for an excitation power of $P = 200$ mW.

As expected from our reasoning, we have found that introducing three QWs instead of just one QW does not improve the behavior (not shown).

In regard to obtaining strong coupling between QW and SRR, we note that the optical selection rules for the QW do not work in our favor: The strongest and longest-wavelength interband optical transition, the one involving the heavy-hole valence band, is dipole-forbidden for an electric field oriented perpendicular to the QW plane. Unfortunately, for the SRR used, this field component is expected to be the strongest one within the QW plane. We expect that the combination of these two aspects reduces the effective coupling between SRR and QW.

We have grown the sample shown in Fig. 1(a) in a Riber 32P MBE machine. The InP substrate was degassed at 175 $^{\circ}$ C in vacuum overnight, heated to 490 $^{\circ}$ C under an As $_4$ flux of 1.4×10^{-5} Torr, and we have performed the epitaxy at 480-485 $^{\circ}$ C under the same As $_4$ flux. The target layers grown lattice-matched to InP and without any interruptions are: 400-nm In $_{0.52}$ Al $_{0.48}$ As buffer and lower barrier, 12.7-nm In $_{0.53}$ Ga $_{0.47}$ As quantum well, 2.5-nm In $_{0.52}$ Al $_{0.48}$ As upper barrier, and a 2.3-nm In $_{0.53}$ Ga $_{0.47}$ As cap layer. We have measured the surface roughness by atomic-force microscopy to be 0.37 nm root mean square in the center of the 51-mm diameter wafer and 0.54 nm at a radius of 20 mm from the center, indicating smooth interfaces.

Low-temperature photoluminescence spectra of the wafer used throughout this work are shown in Fig. 1(b) for various excitation powers. The photoluminescence spectrum at low excitation exhibits a spectral line full width at half maximum of about 25 nm – a good value for a QW that close to the wafer surface.

Next, we fabricate silver split-ring resonators (SRR) using standard electron-beam lithography and standard high-vacuum electron-beam evaporation of silver onto these wafers. Silver is chosen because of its known low losses compared to other metals. Due to the high-refractive-index semiconductor wafer, the SRR lateral features have to be smaller compared to, e.g., SRR on glass substrates (see, e.g., [2,3]) to reach 1.5- μm operation wavelength. The silver thickness is 30 nm. The individual arrays composed of SRR square lattices with lattice constant $a = 250$ nm have a footprint of $100 \mu\text{m} \times 100 \mu\text{m}$.

On each wafer piece we fabricate an entire set of SRR arrays in which the electron-beam exposure dose is systematically varied. This leads to a variation of the geometrical SRR parameters, hence to a tuning of the SRR resonance wavelength from about 1.3 μm to about 1.8 μm . This lithographic tuning allows us to systematically change the spectral detuning between the QW gain position and the SRR resonance. A typical top-view electron micrograph is shown in Fig. 1(c); the measured room-temperature normal-incidence transmittance spectra of all SRR arrays discussed within this paper are displayed in Fig. 1(d). Normalization of the transmittance is with respect to the bare quantum wells.

For all femtosecond experiments shown in this work, the samples are held at helium temperatures in a microscope helium flow cryostat (KryoVac). The actual sample temperature (without optical excitation) is $T = 5\text{-}10$ K.

Optical pumping of the QW to achieve gain is accomplished by pumping the samples from the QW side of the wafer with 150-fs optical pulses at around 810-nm center wavelength obtained from a Ti:sapphire mode-locked laser oscillator (Tsunami from Spectra-Physics, 81-MHz repetition frequency). This oscillator also pumps an optical parametric oscillator OPO (Opal from Spectra-Physics) that is tunable in the spectral range from 1.4 μm to 1.6 μm wavelength. The samples have been designed to be centered in this OPO interval. Pump and probe pulses with variable time delay, Δt , are coaxially focused onto the samples by means of a single 5-cm focal length lens. To ensure that the pump spot is sufficiently large compared to the probe spot to obtain spatially homogeneous excitation conditions, we use two independently adjustable optical telescopes for the pump and the probe beam, respectively. In the sample plane, using a knife-edge technique, we measure a pump-spot diameter of 22 μm (full width at half maximum) and a probe-spot diameter of 10 μm . These spots are sufficiently smaller than the footprint of the SRR arrays quoted above to avoid edge effects. To monitor the focusing conditions as well as the alignment of the two spots relative to each other and relative to the SRR arrays, we image the sample plane onto a PbS camera.

The transmitted probe beam is collected, spectrally filtered to suppress the residual pump, and sent onto a room-temperature Ge photodetector. The pump beam is chopped at about 0.4-kHz frequency and the differential signal ΔI is detected using a standard Lock-In technique. By blocking the probe beam, we routinely ensure that only a negligible fraction of that differential signal stems from pump-induced photoluminescence (that cannot really be spectrally filtered). Typically, the pump-induced photoluminescence is about 10 times weaker than the probe-related differential signal. Upon additionally measuring the probe transmittance, T , without pump, we obtain the relative transmittance change $\Delta I/I$. We follow the usual sign convention, i.e., $\Delta I/I > 0$ corresponds to increased sample transmittance upon optical pumping. The pump polarization is horizontal with respect to the SRR shown in Fig. 1(c), the linear probe polarization is always varied between horizontal and vertical polarization to provide controls. The meaning of these controls will be discussed in Section 3.

We also perform all experiments on the SRR fields and soon thereafter on the side on a region with only the bare QW to provide another set of controls. The meaning of these controls will also be discussed in Section 3. Such experiments are performed for many OPO wavelengths.

As further control experiments, we have twice removed the single QW by mechanical polishing and have performed similar pump-probe experiments on the remaining InP wafers. We have found no detectable differential transmittance signals at all, indicating that no nonlinear contribution outside the noise level stems from the InP substrate for all data shown in this work. Thus, the thick InP substrate can be considered as a passive linear dielectric for the purpose of the present paper.

The average power of the probe beam is set to not more than 0.07 mW in front of the sample (clearly the OPO power varies with OPO wavelength). By further attenuating the probe power at the price of worse signal-to-noise ratio, we have verified that the probe is within the linear regime. The pump beam power is fixed at about 200 mW in front of the sample in this work – unless stated otherwise. This is the maximum power accessible under our experimental conditions (the main part of the Ti:sapphire laser oscillator pumps the OPO). Notably, we have not observed any sample deterioration whatsoever under these conditions – not even over many days. This pump power is expected to completely saturate the QW. We find that the QW photoluminescence spectrum develops a pronounced high-energy tail at powers much below 200 mW [see Fig. 1(b)]. Below, we will discuss on selected examples that the general behavior does not depend on the pump power, whereas the absolute signal strengths obviously do. This observation clearly implies that we have not found any indications of lasing (or “spasing”) in our work.

3. Low-temperature femtosecond pump-probe experiments

Figure 2 gives an overview over the data obtained from one of the SRR arrays, namely one that is nearly resonant with the expected peak of the QW gain spectrum (compare Fig. 1). Data for horizontal (left column in Fig. 2) and vertical (right column in Fig. 2) OPO probe polarization are depicted. For horizontal polarization, the light does couple to the fundamental SRR resonance, for vertical polarization it does not. In all cases, the red curves correspond to measurements on the SRR arrays, the blue curves to measurements on the bare QW on the side, *i.e.*, without any SRR array. The OPO probe center wavelength increases from top to bottom. Note that the width of the OPO spectrum is about 20 nm. Hence, the data have been taken with 20-nm spectral separation. In each case, the dashed black horizontal line defines $\Delta T/T = 0$.

Inspection of the left column of Fig. 2 shows a rather different behavior for the SRR on the QW compared to the bare QW. While the bare QW always delivers positive $\Delta T/T$ signals below about +2% (blue curves), the sign and magnitude of the signals change for the SRR on the QW (red curves). Under some conditions, $\Delta T/T$ reaches values as negative as -8%. Following our introduction, this behavior can be expected for the coupled system of SRR and QW.

In addition to the sign and magnitude of the differential transmittance signal, the temporal behavior is also quite different for the case of SRR on the QW compared to the QW alone. Precisely, the temporal decays tend to become much faster with SRR compared to the case without. For example, for an OPO probe wavelength of 1.48 μm , the blue measured curve can nicely be fitted with a single-exponential decay with a time constant of 670 ps (see dots in Fig. 2). The red curve cannot be fitted with a single exponential (not shown). It can, however, be fitted with the sum of two exponentials (see dots in Fig. 2), one with time constant 15 ps and the other with time constant 180 ps.

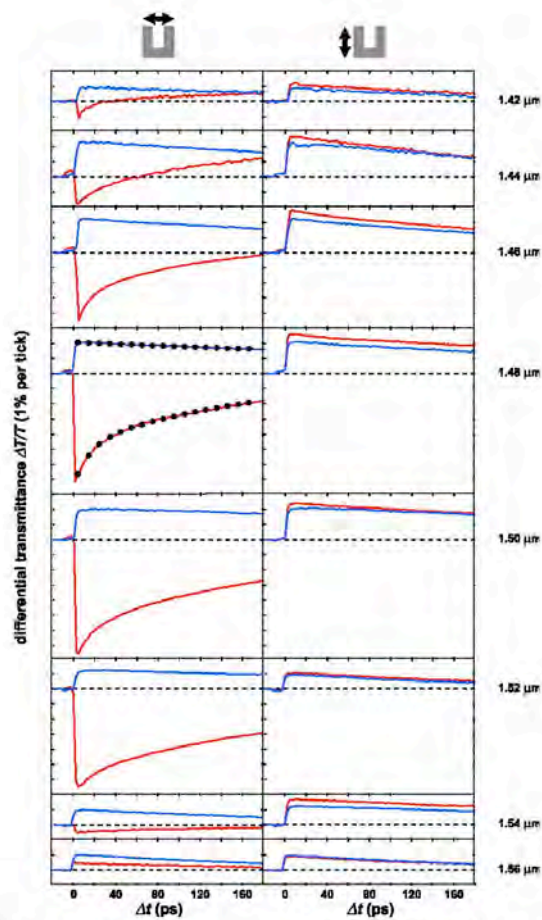


Fig. 2. Femtosecond pump-probe experiments for an array of SRR that is nearly resonant with the QW gain (sample "D" in Figs. 1 and 4). The left column corresponds to horizontal probe polarization with respect to the SRR, the right column to vertical probe polarization. The differential transmittance signals for the case of QW and SRR are shown by the red curves, the case of QW alone by the blue curves. Zero differential signal, *i.e.*, $\Delta T/T = 0$, is indicated by the dashed horizontal lines. One tick on the vertical axis corresponds to $\Delta T/T = 1\%$. The curves are unequally vertically displaced for clarity. The OPO probe wavelength increases from top to bottom as indicated on the right-hand side. Sample temperature is 5-10 K, the 150-fs pump pulses are centered at around 0.81- μm wavelength.

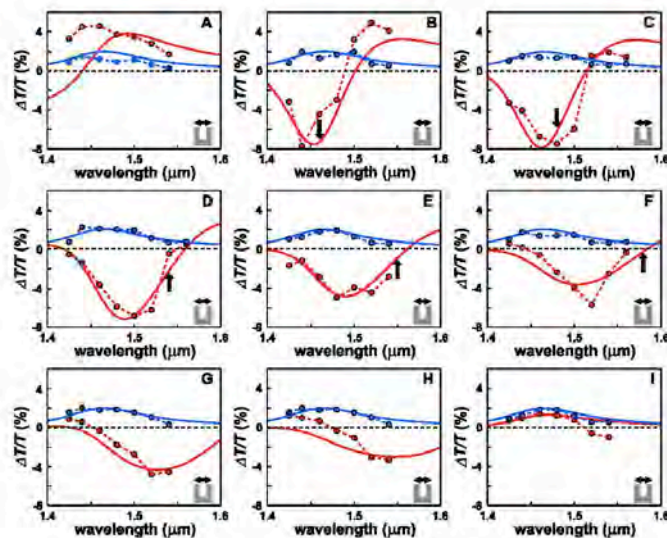


Fig. 4. Summary of femtosecond pump-probe experiments (like exemplified in Figs. 2 and 3) for various SRR arrays. The OPO probe polarization is horizontal. For reference, the measured linear optical spectra of the corresponding SRR arrays are shown in Fig. 1(d). The color coding is the same as in Figs. 2 and 3. Spectra of the differential transmittance signal are shown versus OPO probe wavelength for a fixed time delay of $\Delta t = +5$ ps. Dots connected by dashed straight lines correspond to the experiment, the solid curves are derived from the toy model (parameters are given in the main text). The plasmonic resonance frequencies of the toy model quoted in Table 1 are illustrated by the black arrow in sub-panels B to F; for the other panels the resonances lie outside the wavelength range shown here.

The behavior of the magnitude of the differential transmittance signal in Fig. 2 is also consistent with this interpretation. For a QW with SRR, the modulus of the signals is a factor of about 5 larger than for the case of the bare QW. In Section 4, we will show that this measured behavior is consistent with the toy model, the physics of which has been explained in the introduction (Section 1).

We have taken complete data sets similar to that in Fig. 2 for several other SRR arrays. A second example is shown in Fig. 3. Here, the SRR resonance is largely blue-detuned with respect to the QW gain spectrum, resulting in an off-resonant situation. As expected on the basis of the qualitative discussion in our introduction, we observe a positive differential signal when probing the spectral wings of the SRR resonance. To give an overview on all these results, we compress the data as shown in Fig. 4. Here, we use the same color coding as in Figs. 2 and 3 and merely plot the differential transmittance signal at small positive time delay, *i.e.*, for $\Delta t = +5$ ps, versus the OPO probe wavelength. It becomes obvious that negative $\Delta T/T$ signals for the case of QW and SRR are the rule rather than the exception. In contrast, the $\Delta T/T$ signals are always positive (and generally smaller in magnitude) for the bare QW. Close to resonance between the SRR resonance and the QW gain peak, the behavior is similar to that shown in Fig. 2. For more off-resonant SRR arrays, the differences between QW and SRR and QW alone become smaller – as expected from resonant coupling between the SRR resonance and the QW gain.

4. Comparison with toy model

To obtain a better understanding for the fairly complex measured behavior shown in Figs. 2-4, we compare these data with the above-mentioned toy model that has been defined in detail in [14]. We refer the reader to the mathematics therein. In Section 1 of the present paper, we have already revisited the underlying physics.

Clearly, this toy model [14] has quite a few free parameters: For the resonances of SRR and QW, respectively, one can choose the resonance position Ω , the damping γ , the number density N and the dipole matrix element d – four parameters each. In addition, the local-field coupling parameter L is purely heuristic. Altogether, this makes 9 adjustable parameters. However, the four parameters for the QW gain resonance can already be adjusted on the basis of the experiments on the bare QW (see Fig. 4) where the background dielectric constant is set to $(3.1)^2$. The number density of the SRR can be taken from Fig. 1(c), the other three parameters for the SRR resonance without gain (*i.e.*, without optical pumping) can already be adjusted according to the linear optical spectra of the SRR arrays. Note that the plasmon resonance frequencies referring to low sample temperature listed in Table 1 are consistently blue-shifted with respect to the minima in the room-temperature transmittance spectra shown in Fig. 1(d). This shift is very likely due to the changes in refractive index of the semiconductor materials upon cooling. The combination of these boundary conditions essentially leaves the local-field parameter L as the only truly free parameter. It is expected to be similar for all SRR arrays, regardless of their resonance wavelengths.

In more detail, we compute the differential transmittance by taking the difference between the transmittance of the pumped case (assuming $f = 1$ occupation of the upper level) and the unpumped case (*i.e.*, $f = 0$) and normalize the result with respect to the unpumped transmittance. Using the Maxwell-Garnett approximation described in [14], the 30-nm thin layer of SRR and the 12.7-nm thin single QW are treated as a single effective layer with a thickness of 42.7 nm on top of a dielectric halfspace, the InP substrate. The InP refractive index is taken as $n = 3.1$ (independent of wavelength). In principle, the spectra obtained along these lines should finally be convoluted with the about 20-nm broad OPO probe spectrum. However, for the present conditions, the resulting effects turn out to be unimportant (not shown). Thus, we avoid this process step here. For all samples “A” to “I”, the following model parameters (same nomenclature as in [14]) are fixed: $\Omega_{21,S} = 2\pi \times 205$ THz, $\gamma_{21,S} = 50$ THz, $d_{21,S} = 6.5 \times 10^{-29}$ Cm, $N_{21,S} = 2.1 \times 10^{24}$ m⁻³, $\gamma_{pl} = 90$ THz, $d_{pl} = 4.2 \times 10^{-26}$ Cm, and $N_{pl} = 5.3 \times 10^{20}$ m⁻³. The plasmonic resonance frequencies Ω_{pl} and the local-field parameters L for all samples shown in this paper are listed in Table 1.

Corresponding results are also shown in Fig. 4, allowing for direct comparison with experiment. Obviously, the general agreement between experiment and toy model is excellent considering the complexity of the overall behavior. In particular, we again find that negative differential transmittance signals $\Delta T/T$ are the rule rather than the exception. These negative signals are mainly due to reduction of the damping of the SRR transmittance minimum (see discussion in Section 1). Furthermore, in agreement with experiment, we find that the magnitude of the $\Delta T/T$ signals is substantially larger for the case of QW and SRR compared to the case of the QW alone. Let us emphasize, as already discussed in Section 1, that without any coupling between SRR and QW, *i.e.*, for local-field parameter $L = 0$, the $\Delta T/T$ signals for the case of QW and SRR and the case of QW alone would be just identical (not shown) – in striking disagreement with the experimental facts. This once again emphasizes that our results imply a considerably strong local-field coupling between the SRR and the QW gain – which is at the heart of our aim of reducing the metamaterial’s losses. (The fitted local field coupling parameter L for sample “I” is an anomaly. The fit procedure for this very off-resonant sample turns out to be ambiguous.)

Table 1. Model parameters Ω_{pl} and L that are individually adjusted for samples "A" to "I" (compare Fig. 4).

sample	Ω_{pl}	L
A	$2\pi \cdot 241$ THz	$1.8 \cdot 10^{10}$ F/m
B	$2\pi \cdot 205$ THz	$1.7 \cdot 10^{10}$ F/m
C	$2\pi \cdot 203$ THz	$1.8 \cdot 10^{10}$ F/m
D	$2\pi \cdot 195$ THz	$2.1 \cdot 10^{10}$ F/m
E	$2\pi \cdot 193$ THz	$1.8 \cdot 10^{10}$ F/m
F	$2\pi \cdot 190$ THz	$2.1 \cdot 10^{10}$ F/m
G	$2\pi \cdot 187$ THz	$2.2 \cdot 10^{10}$ F/m
H	$2\pi \cdot 183$ THz	$2.1 \cdot 10^{10}$ F/m
I	$2\pi \cdot 175$ THz	$0.1 \cdot 10^{10}$ F/m

Let us note in passing that the simple toy model [14] cannot describe the Purcell effect, *i.e.*, the near-field non-radiative energy transfer from the QW to the SRR. In the limit of weak probe field and in absence of any spontaneous contributions, the upper-state two-level-system occupation f relaxes exponentially with rate Γ_{2LS} from $f = 1$ to $f = 0$ [see Eq. (5) in Ref. 14]. Subsequently, for the present parameters, all JIT signals with and without SRR show the same exponential decay (in sharp contrast to, *e.g.*, the experimental data in Fig. 2).

Finally, it is interesting to ask on the basis of the toy model: How far are we away from the original aim of completely compensating metamaterial losses? Let us consider the best case, *i.e.*, that the two-level system (2LS) resonance frequency Ω_{2LS} representing the QW and the plasmonic resonance (pl) frequency Ω_{pl} representing the SRR array are degenerate. Under this condition, a simple and transparent way to summarize the influence of the various parameters is to start from the loss = gain condition (lasing spasing condition) (Eq. (13) in [14]) for the two-level system upper-state occupation f , *i.e.*, from

$$f = \frac{1}{2} \left(1 + \frac{\gamma_{pl} \gamma_{2LS}}{V_{pl} V_{2LS}} \right) = \frac{1}{2} \left(1 + \frac{\gamma^2}{V^2} \right) \in [0, 1]. \quad (1)$$

Here, γ_{2LS} and γ_{pl} are the damping frequencies of the two-level system and the plasmonic resonance. The quantities V_{2LS} and V_{pl} are the respective effective coupling frequencies given by (Eq. (9) in [14])

$$\begin{aligned} V_{2LS} &= \hbar^{-1} d_{2LS} L N_{pl} d_{pl}, \\ V_{pl} &= \hbar^{-1} d_{pl} L N_{2LS} d_{2LS}. \end{aligned} \quad (2)$$

The condition (1) is graphically illustrated in Fig. 5. In the gray triangle, the loss = gain condition can *not* be fulfilled because f has a mathematical solution outside the interval $[0, 1]$. In other words, the available gain is simply not sufficient to compensate for the losses. In the white triangle, the loss = gain condition can be fulfilled, even under continuous-wave self-consistent conditions. The red dot corresponds to the parameters that we have used to fit to the experimental data in Fig. 2.

To move the red dot into the white triangle, one could, *e.g.*, increase the QW dipole moment d_{2LS} by a factor of three to four ("more gain"). Alternatively, one could increase the local field coupling parameter L by the same factor ("more effective metamaterials at fixed QW gain"), or reduce the SRR damping ("less loss"), or reduce the QW damping ("more gain") by the same factor. On the basis of the experimental results of this paper, these parameter improvements are not quite impossible, but are not simple to reach either. Other material systems may have to be chosen.

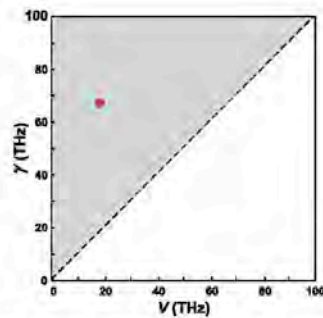


Fig. 5. Illustration of the loss = gain condition for the case that the quantum-well and the splitting-resonator resonances are degenerate [see Eq. (1)]. Complete loss compensation is possible within the white triangle, but is not possible in the gray triangle. The two triangles are separated by the straight line with $\gamma = V$ [see Eq. (1)]. The red dot inside the gray triangle corresponds to the experimental conditions of sample "D" and is obtained from exactly the same model parameters that we have used to fit to these experimental results (compare Fig. 4).

5. Conclusions

We have presented experiments aiming at compensating the metal losses of arrays of SRR by coupling to an optically pumped InGaAs single quantum well *via* the local (or evanescent) electromagnetic fields of the SRR. We observe differential transmittance signals from the coupled system that are a factor of four to five larger than for the bare quantum well. Furthermore, we observe a more rapid temporal decay of the differential transmittance signal for the coupled system compared to the bare quantum well. Both effects indicate substantial local-field-enhancement effects, which increase the effective metamaterial gain beyond the bare quantum-well gain, leading to a significant reduction of the metamaterial's losses. This interpretation is also confirmed by comparison of the experimental data with a recently introduced analytical toy model. However, despite of the fact that we have employed very intense pulsed optical pumping and that we have cooled the samples to helium temperatures and that we have optimized the semiconductor-wafer design, the magnitude of the effect is too small to obtain complete metamaterial-loss compensation in our experiments.

Acknowledgements

We acknowledge support by the Deutsche Forschungsgemeinschaft (DFG) and the State of Baden-Württemberg through the DFG-Center for Functional Nanostructures (CFN) within subproject A1.5. The project PHOME acknowledges the financial support of the Future and Emerging Technologies (FET) programme within the Seventh Framework Programme for Research of the European Commission, under FET-Open grant number 213390. The project MBTAMAT is supported by the Bundesministerium für Bildung und Forschung (BMBF). The PhD education of N.M. and M.R. is embedded in the Karlsruhe School of Optics & Photonics (KSOP). Work at Ames Lab was supported by Dept. of Energy (Basic Energy Sciences), contract No. DE-AC02-07CH11358. The Tucson group thanks AFOSR, NSF AMOP, and NSF ERC CIAN for support. H.M.G. and J.H. thank the Alexander von Humboldt Foundation for a Renewed Research Stay and Junior Scientist Award, respectively.

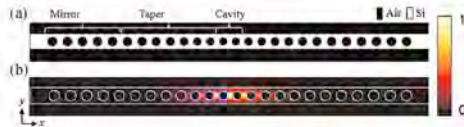


Figure 1 (online color at: www.pss-b.com) (a) Top view of cavity design. (b) Normalized computed electric field profile showing cavity region.

2 Design and fabrication

2.1 Design The first cavity investigated in this study is a photonic crystal nanobeam cavity, which is essentially a wavelength-scale Fabry–Perot etalon formed by sandwiching a 1D photonic crystal waveguide between 1D photonic crystal Bloch mirrors, as shown in Fig. 1. In the transverse directions, the light is confined in the nanobeam by total internal reflection. By smoothly tapering the air hole radius and the corresponding lattice constants in the mirror sections, the scattering loss is minimized and a high Q is achieved [13–15]. 3D finite-difference time-domain (FDTD) simulations [16] reveal that the cavity exhibits a reasonably high Q in excess of 500 000 with very low mode volumes, even though it is placed on a low index substrate. The region of tapered holes in the center of the nanobeam effectively confines the light, analogous to a Fabry–Perot spacer.

2.2 Fabrication The nanobeams are fabricated using electronics grade silicon-on-insulator with a 220 nm silicon device layer and 2 μm buried oxide. To prepare the samples for electron-beam lithography, the wafers are manually cleaned, cleaned with acetone and isopropanol, and the native oxide is removed by a short dip in 10:1 buffered hydrofluoric acid. The samples are then baked at 180 $^{\circ}\text{C}$, spin-coated with 2% PMMA 950 K in chlorobenzene, and baked again at 180 $^{\circ}\text{C}$ for 5 min. Electron-beam lithography is performed in a Leica EBPG 5000+ at 100 kV. Following electron-beam exposure, the samples are developed in 1:3 MIBK/IPA for 60 s, rinsed in IPA, and dried with nitrogen. After development, the wafers are etched using an Oxford Instruments Plasmalab System100 ICP380 with a mixed-mode gas chemistry consisting of SF_6 and C_4F_8 . Figure 2 shows an SEM of one of our nanobeam cavities.

3 Fiber taper loop apparatus Our nanobeams were investigated by means of a transmission measurement through a tapered microfiber loop that was brought into physical contact with the nanobeam. The tapered region of the fiber is 1–1.5 μm in diameter, and the taper loop has a radius of curvature of 200 μm . The taper loop is produced in two stages, first by heating and pulling a standard single mode optical fiber into a taper, and then by forming the tapered region into a loop in a specially built curving apparatus. The fiber is then glued to a microscope slide in such a way that the loop extends beyond the edge of the slide, and the motion of this assembly is controlled by means of a computer controlled, motorized xyz stage.

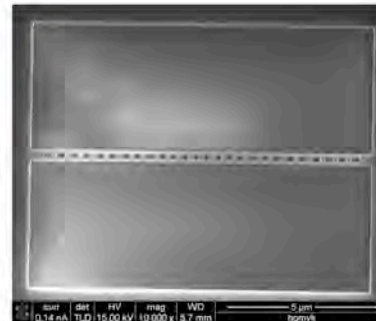


Figure 2 SEM of typical nanobeam cavity.

A beam from an Agilent 8164A mainframe with an Agilent 81682A tunable laser with 0.2 nm wavelength resolution propagates through the fiber and is detected at the output end by means of an InGaAs photodiode. An in-line polarization controller is installed between the laser and the tapered region. The wavelength of the laser is swept across a region of interest, and the output is recorded by a computer. When the tapered loop is moved into physical contact with a nanobeam, light that is propagating through the fiber can be coupled into the mode of the nanocavity, and the resulting interaction is observed as a change in the transmission spectrum output. The laser for this measurement must have a linewidth smaller than the FWHM of a cavity mode, and it must have amplitude fluctuations which are slow compared to the time necessary to scan across a mode. The Q is given by the wavelength of the cavity mode divided by the FWHM of the cavity mode. Figure 3a shows a schematic of the

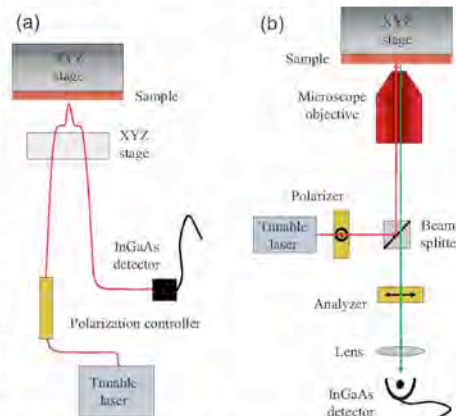


Figure 3 (online color at: www.pss-b.com) (a) Experimental setup for fiber taper loop measurement. (b) Experimental setup for resonant scattering measurement.

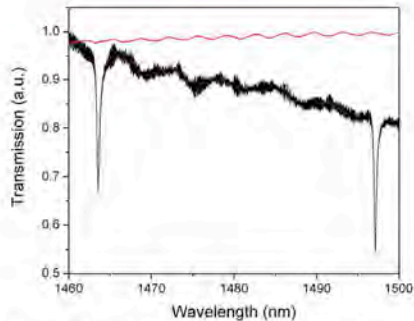


Figure 4 (online color at: www.pss-b.com) Fiber loop transmission spectrum of typical nanobeam cavity at 45° , center contact (black), and spectrum directly from laser (red).

apparatus. Figure 4 shows a typical transmission spectrum of a nanobeam taken with the fiber taper loop apparatus.

4 Coupling to a nanobeam

4.1 Polarization The nanobeams are designed to support a mode which is linearly polarized in a direction perpendicular to the axis of the nanobeam. In order to effectively couple into the cavity mode, the field in the fiber must have a polarization component parallel to the mode of the cavity. Our in-line polarization controller allows us to tune the polarization of the field, and hence control the coupling into the cavity. There are several pathways that the field can travel, each dependent upon the polarization: it can be coupled into the substrate, or it can be scattered back into the fiber in either the forward or the backward direction. As a result of these multiple pathways, we expect to observe interference effects which depend upon the polarization of the incident field, and hence the strength of the coupling into the available channels. We did observe such interference effects, which caused the lineshape of the cavity mode transmission to vary as a function of input polarization, resulting in asymmetric lineshapes. However, by tuning the polarization we were always able to achieve a symmetric lineshape of the transmitted signal.

4.2 Contact pressure The fiber taper loop is brought into contact with the nanobeam, and the motion of the loop is controlled by a motorized xyz stage. As the loop comes near to the surface of the sample, electrostatic and Van der Waals forces pull the fiber into the sample, causing it to stick to the nanobeam.

Once the taper loop is in contact with the nanobeam, it can still be advanced or retracted by the actuators, allowing us to adjust the pressure with which the fiber loop contacts the nanobeam. Increased pressure increases the contact length between the fiber taper and the nanobeam, and hence affects the coupling between them, and decreased pressure caused by pulling the taper away likewise decreases

the contact length. At some point as the loop is pulled away it pops off the surface of the nanobeam.

Because the contact between the nanocavity and the fiber taper introduces another loss mechanism for light to escape from the cavity, we expect the strength of coupling between the two to affect the measured Q of the cavity. Specifically, if the coupling between the two systems is very strong, we expect to observe lower Q s, and hence the optimal configuration for observing the highest Q s will be the configuration that minimizes the coupling between the fiber taper and the nanobeam, while still allowing enough interaction to observe a change in transmission through the fiber. This expectation was confirmed by our observation of the pressure and contact length affecting the measured Q s of our cavities. To measure the highest Q , it is important to minimize the contact length between the nanobeam and the fiber taper.

4.3 Contact position As seen in Fig. 1, the field profile of the cavity mode is concentrated near the center of the nanobeam. As a result, we expect the coupling between the fiber loop and the nanobeam to depend on the position along the length of the nanobeam at which contact is made: contact at the center should result in the strongest coupling, and contact at the edge should result in the weakest coupling. We confirmed that this is in fact the case, and that to measure the highest Q s, the taper loop should be brought into contact as close to the edge of the nanobeam as will still produce a modification in the transmission. Contact near the center of the nanobeam also produces a modification of the refractive index in the environment of the cavity mode, resulting in a shift of the wavelength of the observed resonance.

4.4 Contact angle Because the polarization of the cavity mode is always linearly polarized in the same direction, the coupling between the fiber taper and the cavity mode can also be varied by changing the angle between the fiber taper loop and the axis of the nanobeam. The sample itself is mounted on a rotary stage that allows us to rotate the sample about an axis normal to the sample surface. Whereas the polarization controller only allows control over the polarization along the axis of the fiber, rotating the sample with respect to the fiber provides another degree of control over the coupling.

When the fiber is oriented parallel to the nanobeam, we expect that the field polarization can always be tuned such that it has a component parallel to the mode of the cavity where the coupling between them will be the strongest. Alternatively, when the fiber taper is contacted in a configuration perpendicular with respect to the nanobeam, we would expect that the field never has a component parallel to the cavity mode, and hence coupling between the two will be minimal.

We found that in the parallel configuration, the coupling was indeed the strongest, and the Q the lowest. As we tuned the angle between the nanobeam and the fiber away from parallel, the Q improved, but at angles close to the

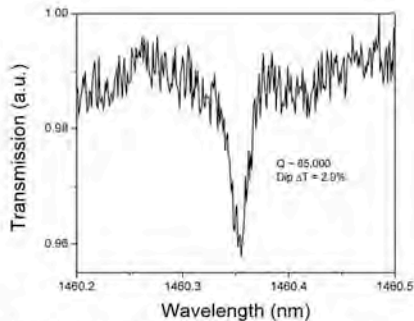


Figure 5 Fiber loop transmission spectrum of high- Q cavity mode, at 45° edge contact, with $Q = 85\,000$.

perpendicular configuration, there was not enough coupling to observe a change in the transmitted signal.

4.5 Results The highest Q s were observed with an angle of the fiber taper between 20 and 60° with respect to the nanobeam axis, and contact made at the edge of the nanobeam. This configuration minimizes the contact between the loop and the nanobeam, but still supports a polarization component corresponding to the cavity mode. The highest Q measured in our system was 85 000, which with a computed mode volume of $0.27(\lambda/n)^3$, yields Q/V of 315 000, which we believe to be the highest Q/V reported in nanobeams on substrate. The group of De La Rue [17] reported a Q of 147 000 with a computed mode volume of $0.85(\lambda/n)^3$, yielding Q/V of 173 000. Figure 5 shows the transmission spectrum of our highest Q cavity mode.

5 Comparison to resonant scattering Another method commonly used for measuring the Q s of semiconductor nanobeam cavities is a cross-polarized resonant scattering technique [8, 9], shown in Fig. 3b. Whereas the fiber taper measurement introduces an additional loss mechanism to the cavity, and hence lowers the Q , the resonant scattering technique does not affect the Q of the cavity, and hence provides a more accurate measurement of the intrinsic Q . We compared the two techniques and found that the Q s measured by resonant scattering were higher than those measured on the same cavity by fiber taper loop. However, the resonant scattering technique also suffers from some drawbacks. First, in the spectral region of our cavity modes and within the range of our tunable laser, 1460–1580 nm, there is a number of absorption lines due to atmospheric nitrogen, which also appear as dips in the detected signal similar to the cavity modes of the nanobeams. If one of these lines is spectrally coincident with the mode of a cavity, it is not possible to distinguish the dip of the cavity mode from the dip due to nitrogen absorption. This was unfortunately the case with our highest Q cavity of 85 000 that was measured with the fiber taper. In order to overcome

this difficulty, the cavity mode would have to be tuned away from the nitrogen resonance, for instance by heating or by condensation of xenon or nitrogen gas [18]. Second, the resonant scattering method is known to exhibit asymmetric lineshapes. This is attributed to a Fano interference between the resonantly scattered light and the coherent background, and requires that a Fano lineshape be fit to the data in order to determine the cavity Q . Galli et al. have reported [19] that the asymmetry of the lineshape can be changed by changing the spot size of the incident laser beam.

In addition to these considerations, the two methods also differ in ease of setup and use. The fiber taper loop is very robust and easy to use once it is set up; however, the fabrication of the fiber taper loop itself requires special equipment and experience. The resonant scattering method can be set up with standard optical laboratory components and instruments, but it is extremely sensitive to alignment and hence more difficult to use. Both methods are useful at room temperature as well as at cryogenic temperatures, but the fiber loop measurement would require substantial modification to most cryostats for low temperature measurements. The resonant scattering measurement does not require components inside the cryostat.

6 2D GaAs slab nanocavities While nanocavities in silicon achieve very high Q s, GaAs remains the system of choice for quantum optics experiments because of the ease of incorporating active emitters, such as InAs QDs, which has so far remained elusive for Si. The majority of our research focuses on the GaAs/InAs 2D photonic crystal slab system for the purpose of quantum optics experiments. However, in spite of extensive efforts by the cavity QED community aimed at reaching high Q s at shorter wavelengths in GaAs PC nanocavities, the results have been disappointing compared to what has been achieved at longer wavelengths in GaAs [20] and Si.

In the course of work toward optimizing the growth and fabrication of such GaAs 2D nanocavities, AFM of the sample surface was used extensively for characterizing the quality of the growth. We found, that even on samples where AFM showed a smooth surface, TEM images revealed that the top of the AlGaAs sacrificial layer could be very rough, with the roughness larger along one crystal axis. Changing certain MBE growth parameters reduced the roughness, but this did not result in a noticeable increase in Q [7], indicating that other loss mechanisms are still holding down the Q s. With future improvements in fabrication, we expect the smoothness of the AlGaAs layer to be significant.

Investigations of the sample surfaces by AFM and SEM also revealed debris on the surface of the samples that we believed to be an artifact of the HF acid wet etch. A 140 s dip in a KOH solution removed the debris, confirming that it was most likely a hydroxide of aluminum generated during the wet etch. The measured Q s of the cavities did improve noticeably following the removal of this debris, by an average of 50% on 10 different nanocavities, and the intensity of the photoluminescence also increased [7].

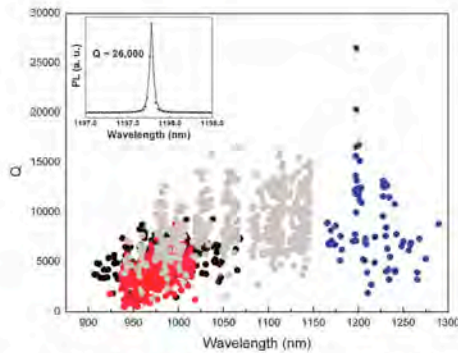


Figure 6 (online color at: www.pss-b.com) Scatter plot of Q s from four different samples: QD24-3 (black), QD25-3 (red), A0961-3 (gray), and QD58-1 (blue).

Such improvements in growth and fabrication have yielded modest improvements in the Q s we have been able to achieve. Nevertheless, we still consistently observe that even our best samples show lower Q s as wavelength decreases. Figure 6 shows Q versus wavelength data for several 100 nanocavities from four of our best samples covering a broad wavelength range from 900 to 1300 nm. The data show a decisive decrease in Q in the shorter wavelength region. The highest Q measured was 26 000, and the PL spectrum for this nanocavity is shown in the inset to Fig. 6.

7 Conclusion We have succeeded in measuring the Q s of photonic crystal nanobeam cavities using a fiber taper loop, and have observed Q s as high as 85 000, which yields the highest Q/V ratio reported in these devices on substrate. We have observed that the results of this technique depend on strength of contact between the fiber and the nanobeam, incident field polarization, contact position on the nanobeam, and angle between the fiber loop and the nanobeam. We compared our results to the cross polarized resonant scattering method, and found that the fiber loop does lower the Q s, but that the effect can be minimized and high Q s can still be measured by choosing the above parameters appropriately.

Acknowledgements The USA authors would like to acknowledge support (EEC-0812072) from the National Science Foundation (NSF) through the Engineering Research Center for Integrated Access Networks (CIAN). The Tucson group also acknowledges support from NSF Atomic Molecular and Optical Physics (AMOP) and Electronics, Photonics, and Device Technologies (EPDT), AFOSR, and Arizona Technology & Research Initiative Funding (TRIF). The Caltech authors gratefully acknowledge critical support and infrastructure provided for this work by the Kavli Nanoscience Institute at

Caltech. H. M. G. thanks the Alexander von Humboldt Foundation for a Renewed Research Stay. A. H. appreciates the generous support of the ARCS Foundation.

References

- [1] T. Yoshie, A. Scherer, J. Hendrickson, G. Khitrova, H. M. Gibbs, G. Rupper, C. Ell, O. B. Shchekin, and D. G. Deppe, *Nature* **432**, 200–203 (2004).
- [2] D. Englund, D. Fattal, E. Waks, G. Solomon, B. Zhang, T. Nakaoka, Y. Arakawa, Y. Yamamoto, and J. Vuckovic, *Phys. Rev. Lett.* **95**, 013904 (2005).
- [3] D. Press, S. Gotzinger, S. Reitzenstein, C. Hofman, A. Löffler, M. Kamp, A. Forchel, and Y. Yamamoto, *Phys. Rev. Lett.* **98**, 117402 (2007).
- [4] J. Hendrickson, B. C. Richards, J. Sweet, S. Mosor, C. Christenson, D. Lam, G. Khitrova, H. M. Gibbs, T. Yoshie, A. Scherer, O. B. Shchekin, and D. G. Deppe, *Phys. Rev. B* **72**, 193303 (2005).
- [5] G. Khitrova, H. M. Gibbs, M. Kira, S. W. Koch, and A. Scherer, *Nature Phys.* **2**, 81–90 (2006).
- [6] U. K. Khankhoje, S.-H. Kim, B. C. Richards, J. Hendrickson, J. Sweet, J. D. Olitzky, G. Khitrova, H. M. Gibbs, and A. Scherer, *Nanotechnology* **21**, 065202 (2010).
- [7] J. Sweet, B. C. Richards, J. D. Olitzky, J. Hendrickson, G. Khitrova, H. M. Gibbs, D. Litvinov, D. Gerthsen, D. Z. Hu, D. M. Schaadt, M. Wegener, U. Khankhoje, and A. Scherer, *Photon. Nanostruct. Fundam. Appl.* **8**, 1–6 (2010).
- [8] M. W. McCutcheon, G. W. Rieger, I. W. Cheung, J. F. Young, D. Dalacu, S. Frédéric, P. J. Poole, G. C. Aers, and R. L. Williams, *Appl. Phys. Lett.* **87**, 221110 (2005).
- [9] D. Englund, A. Faraon, I. Fushman, N. Stoltz, P. Petroff, and J. Vucković, *Nature* **450**, 857–861 (2007).
- [10] K. Srinivasan, P. E. Barclay, M. Borselli, and O. Painter, *Phys. Rev. B* **70**, 081306(R) (2004).
- [11] I.-K. Hwang, G.-H. Kim, and Y.-H. Lee, *IEEE J. Quantum Electron.* **42**, 131–136 (2006).
- [12] B. C. Richards, J. Hendrickson, J. D. Olitzky, R. Gibson, M. Gehl, K. Kieu, U. K. Khankhoje, A. Homyk, A. Scherer, J.-Y. Kim, Y.-H. Lee, G. Khitrova, and H. M. Gibbs, *Opt. Express* **18**, 20558–20564 (2010).
- [13] P. Deotare, M. McCutcheon, I. Frank, M. Khan, and M. Loncár, *Appl. Phys. Lett.* **94**, 121106 (2009).
- [14] C. Sauvan, P. Lalanne, and J. Hugonin, *Phys. Rev. B* **71**, 1–4 (2005).
- [15] E. Kuramochi, H. Taniyama, T. Tanabe, K. Kawasaki, Y.-G. Roh, and M. Notomi, *Opt. Express* **18**, 15859–15869 (2010).
- [16] A. Oskooi, D. Roundy, M. Ibanescu, P. Bermel, J. Joannopoulos, and S. Johnson, *Comput. Phys. Commun.* **181**, 687702 (2010).
- [17] A. R. M. Zain, N. P. Johnson, M. Sorel, and R. M. De La Rue, *Opt. Express* **16**, 12084–12089 (2008).
- [18] S. Mosor, J. Hendrickson, B. C. Richards, J. Sweet, G. Khitrova, H. M. Gibbs, T. Yoshie, A. Scherer, O. B. Shchekin, and D. G. Deppe, *Appl. Phys. Lett.* **87**, 141105 (2005).
- [19] M. Galli, S. L. Portalupi, M. Belotti, L. C. Andreani, L. O’Gaolain, and T. F. Krauss, *Appl. Phys. Lett.* **94**, 071101 (2009).
- [20] S. Combrí, A. De Rossi, Q. V. Tran, and H. Benisty, *Appl. Phys. Lett.* **87**, 141105 (2005).

Modelling and fabrication of GaAs photonic-crystal cavities for cavity quantum electrodynamics

U K Khankhoje¹, S-H Kim¹, B C Richards², J Hendrickson²,
J Sweet², J D Orlitzky², G Khitrova², H M Gibbs² and A Scherer¹

¹ Electrical Engineering, California Institute of Technology, Pasadena, CA 91125, USA

² College of Optical Sciences, University of Arizona, Tucson, AZ 85721, USA

E-mail: uday@caltech.edu

Received 5 November 2009, in final form 14 December 2009

Published 8 January 2010

Online at stacks.iop.org/Nano/21/065202

Abstract

In this paper, we present recent progress in the growth, modelling, fabrication and characterization of gallium arsenide (GaAs) two-dimensional (2D) photonic-crystal slab cavities with embedded indium arsenide (InAs) quantum dots (QDs) that are designed for cavity quantum electrodynamics (cQED) experiments. Photonic-crystal modelling and device fabrication are discussed, followed by a detailed discussion of different failure modes that lead to photon loss. It is found that, along with errors introduced during fabrication, other significant factors such as the presence of a bottom substrate and cavity axis orientation with respect to the crystal axis, can influence the cavity quality factor (Q). A useful diagnostic tool in the form of contour finite-difference time domain (FDTD) is employed to analyse device performance.

(Some figures in this article are in colour only in the electronic version)

1. Introduction

Photonic-crystal cavities have come a long way from the initial conceptualization of photonic crystals [1, 2]. Sustained efforts in semiconductor growth, lithography and etching techniques have paved the way for the creation of high Q , low mode volume (V) optical resonators that are ideally suited for exploring effects in quantum optics such as Purcell enhancement [3], vacuum Rabi splitting or strong coupling [4], and photon anti-bunching [5].

In our experiments, optical resonators are constructed by perturbing a 2D photonic crystal composed of a triangular lattice of air holes in a thin slab of GaAs (see figure 1(a)), and embedded InAs QDs serve as internal light sources. Typical resonator designs involve the creation of a defect by omission of one or more holes and/or the modification of the immediate neighbourhood of the missing air hole(s). Figure 1(b) demonstrates one such tuning process to get high Q/V resonant modes, in which two air holes are shifted by s [6]. In such a geometry, horizontal in-plane optical confinement is provided by the photonic bandgap [1] which can be nearly perfect as long as the cavity is surrounded by sufficiently many layers of photonic crystals. Incomplete

vertical confinement [7] happens on account of index contrast between the slab and the surrounding vacuum and is the primary cause of photon loss. The slab thickness is chosen such that only the lowest-order optical mode in the vertical direction is supported, thereby keeping the mode volume at a minimum and suppressing the coupling to the higher-order slab modes. Therefore, the slab thickness tends to be approximately close to half the wavelength of light in the material for optimal confinement.

This paper is dedicated to the modelling and fabrication of these devices, followed by a detailed investigation of the important channels for optical loss in these devices. Using three-dimensional (3D) FDTD methods and contour information extracted from the scanning electron micrograph (SEM) of a fabricated device, it is shown how various optical properties can be accurately analysed. Then, two important distinctive mechanisms of Q degradation will be emphasized: the presence of a bottom substrate and crystal-axis-dependent surface roughness resulting from the epitaxial growth process. As shown in the schematic in figure 1(a), a typical epi-structure for GaAs photonic-crystal slabs includes an optically flat bottom substrate. The sacrificial layer thickness is of the order

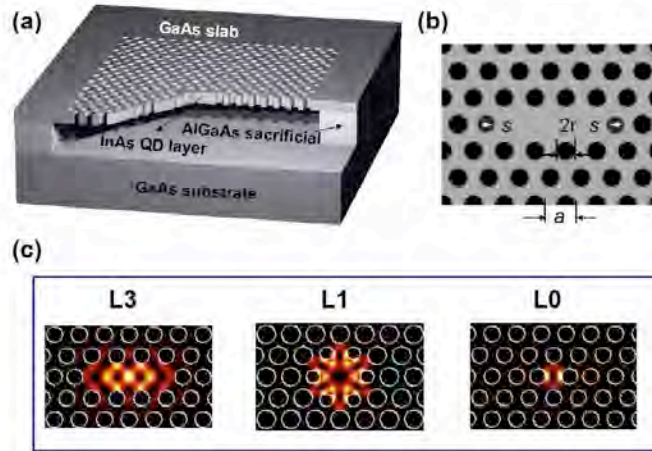


Figure 1. (a) Cutaway of a photonic-crystal-slab cavity. (b) Top view of the L3 cavity design. a , r , s are the lattice constant, radius and hole shifts, respectively. (c) In-plane (centre of slab) electric-field energy densities for three typical cavity designs; L3 (three missing holes, shifted end holes), L1 (one missing hole, shifted and shrunk nearest-neighbour holes) and L0 (no missing holes, only two shifted holes).

of $\sim 1 \mu\text{m}$, which has been chosen to be sufficiently larger than the evanescent tail of photonic-crystal cavity modes. However, it is still comparable to the free space emission wavelengths of InAs QDs used in this work. As a result, interesting interference effects originate from air-gap size-dependent resonances. The fabrication of these devices is fairly involved and challenging, and in our experiments we have come across several failure modes. Here, an attempt is made to catalogue these, and to suggest solutions where possible.

2. Photonic-crystal cavity modelling

For all the elegance of photonic crystals, a completely analytical description is illusive and hence these devices must be analysed numerically. Frequency-domain simulations [8] of the defect-free photonic-crystal slab reveal the extent of the photonic bandgap as a function of the in-plane Bloch wavevectors, as seen in figure 2. A subtlety must be mentioned at this point: since the structure only has 2D periodicity, light is (incompletely) confined in the vertical direction by total internal reflection. Therefore, any mode designated by (ω, k) lying above the light line, $\omega = ck$ (ω , c , k : optical frequency, speed of light and in-plane wavevector, respectively) will always couple to the continuum of vacuum electromagnetic (radiation) modes. Thus, the photonic bandgap in this case is defined as the frequency range that is devoid of any guided modes [9] below the light line (i.e. for $\omega < ck$) (radiation modes will exist at all frequencies). It should be noted that all guided bands can be divided into two groups depending on the mirror symmetry with respect to the plane in the middle of the slab; even and odd (or, equivalently, transverse electric (TE)-like or transverse magnetic (TM)-like, to invoke the similarities to their 2D counterparts). In the case of the triangular lattice

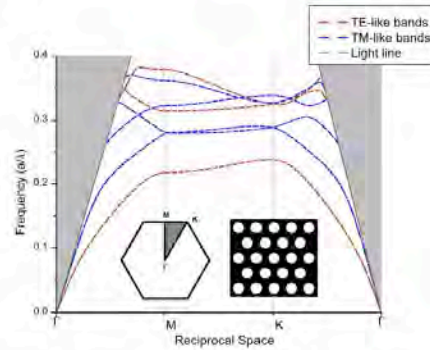


Figure 2. Dispersion diagram for TE-like (even) and TM-like (odd) modes of a 2D photonic-crystal slab composed of a triangular lattice of air holes (slab width, d , dielectric constant ϵ). $r/a = 0.30$, $d/a = 0.75$, $\epsilon = 12.605$. Insets show the reciprocal lattice space along with the irreducible Brillouin zone (shaded grey) and a real-space representation of a regular photonic crystal.

of air holes it is well known that a bandgap exists only for TE-like modes, and this can be seen in figure 2. In section 4.1.3 this characteristic of the photonic-crystal band structure will be revisited to explain an in-plane loss channel.

While frequency-domain simulations reveal highly accurate eigenfrequencies and modes, they cannot be used for time-dependent phenomena, such as Q calculations, and it is here that 3D FDTD simulations [10, 11] must be employed. Using these tools, we have modelled, fabricated and characterized

Table 1. Parameter summary of typical cavity designs obtained by 3D FDTD tools. r' refers to the radius of the perturbed holes. λ , V , g refer to the mode wavelength, mode volume and slab refractive index, respectively.

	$(\frac{r'}{\lambda}, \frac{r'}{\lambda^2}, \frac{r'}{\lambda^3}, \frac{r'}{\lambda^4})$	$(\frac{g}{\lambda}, Q, \frac{V}{(\lambda a)^3})$
L0	(0.75, 0.30, 0.14, 0.30)	(0.287, 71 000, 0.122)
L1	(0.50, 0.35, 0.10, 0.25)	(0.300, 323 740, 0.422)
L3	(0.75, 0.30, 0.17, 0.30)	(0.247, 67 315, 0.392)

several cavity designs that feature high Q s and low V s; L3 [6], L1 [12] and L0 [13] cavity geometries (see figure 1(c)). Table 1 summarizes the various salient features of these cavities.

The regime of strong coupling [14] is entered when the coupling strength, g , between the QD and the cavity mode exceeds the average of the individual decay rates of the QD, γ , and the cavity mode, κ , i.e. $2g > (\gamma + \kappa)/2$. The motivation to choose a high Q comes from the fact that $\kappa \propto 1/Q$, while the need for a low V comes from the fact that $g \propto 1/\sqrt{V}$. To apply these cavity designs for cQED, special care must be taken to optimize both spatial and spectral overlap between a single QD and a cavity mode. Specifically, the placement of a QD at positions very close to the GaAs surfaces must be avoided, since coupling to surface states [15] will lead to strong non-radiative losses. In light of these considerations, the L3 mode which has the highest electric-field intensity at the cavity centre (see figure 1(c)) seems to be the most promising candidate for cQED experiments.

3. Fabrication and optical characterization

The GaAs material in which these resonators are fabricated is grown by molecular beam epitaxy (MBE). Details of this growth are provided elsewhere [16]. We typically start with a blank (001)-oriented GaAs wafer, onto which a 300 nm GaAs buffer is grown, followed by a 1 μm thick sacrificial layer of the type $\text{Al}_x\text{Ga}_{1-x}\text{As}$ (with $0.7 \leq x \leq 0.94$), a 90 nm GaAs bottom slab, an atomic monolayer thick wetting layer on which form InAs QDs and finally a 90 nm GaAs top slab. It must be noted that, in the above-described scheme, dot growth is strain-induced and hence has a spatially probabilistic distribution. Further, minute variations in QD dimensions across the wafer give rise to a spectral distribution of emission wavelengths, typically a 5% spread about a 1 μm central wavelength. It is worth mentioning here that the QD has an electric-field polarization that is primarily in-plane and thus couples to the TE-like (even) modes of the photonic crystal.

Fabrication of photonic-crystal cavities involves the following steps: cleaning of the top of the grown GaAs wafer surface, spinning and baking of an electron-beam resist, electron-beam lithography and subsequent resist development, pattern transfer into the substrate using a chemically assisted ion beam etch (CAIBE), removal of the underlying sacrificial layer by a suitable wet etch and a final strip of the remnant resist.

The first step in device fabrication is the removal of any organic material from the top GaAs surface using acetone and iso-propyl-alcohol (IPA). Any GaAs surface that has been

exposed to atmospheric oxygen forms a thin oxide layer and this is removed by immersing the wafer in a dilute solution of hydrochloric acid (HCl) (1:1 = HCl:deionized water (DI) by volume) for 10 min. After blow drying with N_2 gas and heating on a hot plate at 170 °C for at least 10 min, the wafer is ready for the spinning on of a thin layer of resist. Targeting a thickness of 150 nm, a high molecular-weight positive electron beam resist (950 K poly-methyl-methacrylate (PMMA) in anisole solvent) is spun on to the wafer and baked on a hot plate kept at 170 °C for 30 min. Electron-beam lithography is then performed using a Vistec EBPG-5000+ 100 kV machine that is able to expose the device masks at a resolution of 2.5 nm. Employing a low beam current in the region of 800 pA accomplishes the proper exposure of the device masks. The exposed wafer is developed for 1 min in a solution of 1:3 = methyl-iso-butyl-ketone (MIBK):DI, followed by a 30 s rinse in IPA and a gentle N_2 blow dry. The developed devices are inspected in an SEM to confirm proper exposure and adequate development.

The developed devices are then dry etched in a CAIBE for 3 min. The etcher uses a Kaufman ion source that ionizes a 4 standard-cubic-centimetres-per-minute (sccm) flow of argon gas at a beam voltage and current of 600 V and 25 mA, respectively. Cl_2 gas is injected into the chamber just above the sample at a flow rate of 7 sccm. At the completion of the etch, the sample is immediately wet etched in a dilute solution of hydrofluoric acid (HF) (1:10 = HF:DI by volume) for 60 s, rinsed in DI and IPA for 60 s each and allowed to dry. The sample is then agitated in a solution of IPA, chloroform and acetone (1:1:1 by volume) for 10 min to strip the resist. This removes all of the resist, except for the regions around the devices. The sample is then exposed to a gentle oxygen plasma treatment for complete resist removal. An Oxford Instruments ICP-RIE 180 is used to perform this treatment for 90 s, employing an O_2 flow rate of 90 sccm in a chamber at 10 mTorr, a low RF field (1 W) and a very high ICP power (600 W) that results in a gentle O_2 plasma that keeps the DC bias below 20 V. This is important in minimizing any surface damage that can be caused by the procedure.

The fabricated devices are placed in an evacuated liquid helium cryostat, cooled down to approximately 10 K and excited by a non-resonant Ti:sapphire laser operating at 780 nm with an approximate power of 500 μW . Photoluminescence from excited cavities is collected by a (36 \times) microscope objective, passed through a spectrometer and recorded on either an Si detector (for wavelengths <1 μm) or an InGaAs detector (for wavelengths >1 μm). Figure 3(a) shows the photoluminescence observed from a high Q cavity. A Lorentzian fit is used to calculate the Q .

Through careful Q measurements on a large set of fabricated devices, it is found that the measured Q values are not as high as computed, even though fabricated devices look nearly perfect in all aspects: side-wall roughness, circularity of holes, etc (see figure 3(b)). The following sections will be devoted to discussions of possible factors limiting Q based on practical considerations.

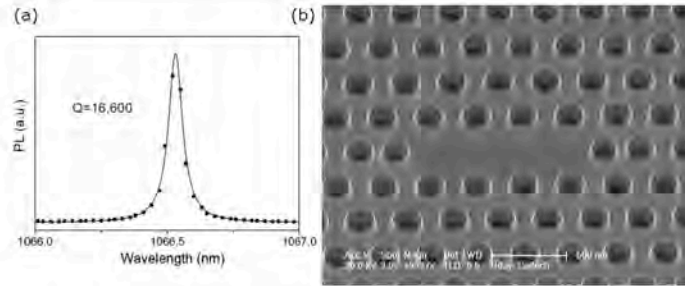


Figure 3. (a) Photoluminescence from a photonic-crystal cavity showing a Lorentzian fit to the data for the highest Q recorded. (b) Tilted SEM image of a fabricated L3 device.

4. Quality factor considerations

As has been discussed elsewhere [17], the Q of a device can be decomposed into the following factors:

$$Q^{-1} = Q_{\text{rad}}^{-1} + Q_{\text{mat}}^{-1},$$

where Q_{rad}^{-1} indicates the optical loss from the cavity by coupling to radiation modes in vacuum and Q_{mat}^{-1} represents a combination of the intrinsic loss in the material, the loss due to the formation of surface states that inevitably result from the oxygen termination of broken dangling GaAs bonds at the etched interfaces and any gain or loss [18] that might occur due to QD absorption in the cavity's spectral and spatial neighbourhood. The loss represented by Q_{mat}^{-1} is strongly wavelength-dependent. On the one hand, GaAs shows increased loss [17] due to (sub-bandgap) surface states as one approaches the GaAs band edge at ≈ 814 nm (at 10 K). Simultaneously, at wavelengths close to and lower than the QD ensemble peak (typically between 950 and 1100 nm), absorption by the QDs and the wetting layer further degrades Q from the 'empty' (no QD) cavity Q [18]. Q_{rad}^{-1} can be further divided into two terms, Q_0^{-1} and Q_{scat}^{-1} , where Q_0^{-1} indicates the intrinsic radiation loss in the absence of any fabrication-related error while Q_{scat}^{-1} is the loss due to (Rayleigh) scattering from surface imperfections introduced during MBE growth and device fabrication. To start with, fabrication-related failure modes that are fairly evident are presented, before moving on to Q -degrading factors that might not be obvious.

4.1. Factors related to the fabrication failure modes

4.1.1. Irregular shapes and positions of the air holes. Q_0 is optimized by a careful control of the cavity geometry and, in the case of L3 designs, can be theoretically as high as 67 000 in GaAs. (Higher Q s have been reported with photonic-crystal waveguide-type designs, but they are not considered here because of their higher mode volumes (calculated [19] as $V \equiv [\int_V \epsilon(\vec{r}) |\vec{E}(\vec{r})|^2 d^3r] / \max[\epsilon(\vec{r}) |\vec{E}(\vec{r})|^2]$). Any irregularities in the lithography or etching can severely degrade Q_{rad} . A poorly focused electron beam can be a major cause of lithographic irregularities, with the photonic-crystal holes deviating from

circular shapes, as well as exposing areas larger than intended. Unless carefully controlled, the lithography step can also lead to considerable lack of reproducibility. Figure 4(b) illustrates the above-mentioned effects featuring non-circular and larger-than-intended holes which lead to the merging of holes that are closer than the lattice constant.

4.1.2. Remnant PMMA and debris. A thin layer of resist, as seen in figure 4(c) (darker, wrinkled features), is often left behind even after chemical treatment for removal. In our experience, this last layer of resist can only be removed by an oxygen plasma treatment. Moreover [16], a fine layer of submicron-sized microcrystallites is sometimes left behind after the completion of resist removal. These particles were speculated to be a hydroxide of aluminium that formed during the HF wet etch and floated from the sacrificial layer and ultimately were deposited on the top of the remnant resist. A 150 s dip in a solution of potassium hydroxide (KOH) (25 g/100 ml DI) was effective in completely removing this debris to restore the top surface to near-atomic smoothness. In terms of device performance, Q s were found to increase [16] on average by 50% after this KOH treatment, indicating that the debris was a very significant source of scattering loss. In subsequent fabrication runs, this KOH step was incorporated in the fabrication sequence right after the HF wet etch. Figure 4(a) shows a tilted view of a surface with debris prior to the KOH treatment and figure 3(b) shows a fully fabricated device. Finally, roughness and ion-induced side-wall damage are introduced to the surfaces during the CAIBE etch which can further contribute to scattering. It is not possible to quantify the contribution of the latter source of scattering at this point, as the surfaces seem fairly smooth even in high resolution SEMs.

4.1.3. Non-vertical side-walls. Maintaining a vertical etch profile in the dry etch is also important [20]. As explained in section 2, the presence of mirror symmetry in the case of perfectly vertical side-walls allows one to classify slab modes into even and odd symmetry modes. However, non-verticality of etched air holes breaks this symmetry, which results in new forms of hybridized modes that can no longer be classified as

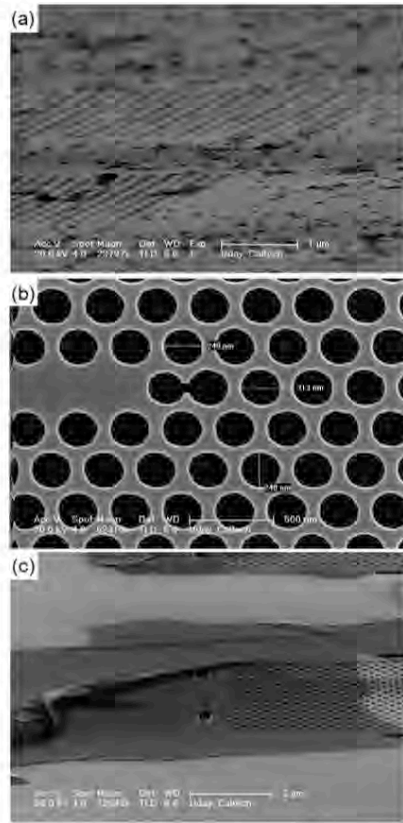


Figure 4. (a) SEM of a tilted slab showing the presence of fine debris after undercutting with HF. (b) SEM showing the effects of poor lithography on a photonic-crystal cavity. (c) SEM of a tilted L3 cavity showing remnant resist (dark, wrinkled features).

either even or odd. A deviation from a vertical etch by even 2° can cause Q_{rad} to drop by an order of magnitude and this is due to the well-known TE–TM coupling loss [21]. There are at least two factors that can cause non-vertical side-walls. Firstly, inadequate or excessive resist development can give rise to non-vertical resist side-walls, which in turn are transferred to non-vertical side-walls in the GaAs substrate. Secondly, a non-vertical flow of Cl_2 gas onto the substrate during the dry etch in the CAIBE can lead to asymmetric and non-vertical side-walls. Small-angle deviations ($\leq 2^\circ$) from the vertical are hard to measure with the available resolution in an SEM, making it difficult to precisely quantify this loss channel. In general, it is easier to control etch symmetry and verticality using a plasma etch, such as in an inductively coupled plasma-reactive ion etcher (ICP-RIE). Additionally, the use of photonic crystals with a complete photonic bandgap for both TE-like and TM-like modes can reduce the severity of a non-vertical

etch. Significant results have been achieved using reduced symmetry photonic crystals [22–24], although in general, the spectral extent of the TM-like bandgap is much less than that of the TE-like counterpart.

4.2. Effect of a bottom substrate

Removal of the AlGaAs sacrificial layer below the photonic-crystal slab creates an air gap, exposing an optically flat surface. It is important for this air gap to be at least greater than half the vacuum wavelength to reduce optical loss into the substrate. It should be noted that reflectivity at the GaAs substrate is $\sim 30\%$. Therefore, the effect of a bottom substrate is essentially that of a reflector below the photonic-crystal mode. For an air-gap size larger than half the vacuum wavelength, there can be multiple non-negligible reflections between the photonic-crystal slab and substrate. Thus, a fraction of the originally downward-emitted photons from the cavity are redirected upward by the bottom reflector to interfere with the originally upward-emitted photons. As a result, the far-field radiation pattern of the cavity mode is modified, changing the total emitted power [25, 26]. This is analogous to the well-known cQED example of a point dipole source in front of a mirror [27]. By changing the distance between the dipole source and the mirror, the original decay rate and radiation pattern are modified. Analogously, the Q of the cavity mode changes as a function of the air-gap size.

In figure 5 the Q of the L3 cavity mode is calculated by varying the air-gap size, t . Even when $t \geq 800$ nm, Q varies by about $\pm 5\%$ around Q_∞ (where $Q_\infty = 67\,315$ obtained in the absence of a bottom substrate). A larger variation in Q can be obtained by starting with a cavity mode that has a smaller Q_∞ , since more radiative power will contribute to far-field interference. Through additional FDTD simulations, it is found that a Q variation larger than $\pm 10\%$ is expected when $Q_\infty \sim 50\,000$. Therefore, the AlGaAs sacrificial layer thickness should be chosen carefully if Q is of primary concern in the design of photonic-crystal cavities.

4.3. Contour FDTD simulation

Although the theoretical cavity Q s can be as high as 67 000, less than half this number has been experimentally observed (see figure 3(a)). To investigate this discrepancy, the use of a 2D contour image extracted from the SEM image of a fabricated device for the purposes of Q estimation is proposed.

Let us consider the particular case of a fabricated L3 cavity whose resonant wavelength and Q are measured to be 1144.1 nm and 10050, respectively. First, all the structural parameters (r , r' , s and a) characterizing the cavity are extracted from the corresponding SEM image (It should be noted that there can be $\sim \pm 5\%$ error in the SEM scale.). 3D FDTD simulations based on these parameters reveal a resonant wavelength and Q of 1129.7 nm and 31418, respectively. Clearly, Q values estimated in this way differ significantly from the measured Q .

Instead, contour data that faithfully captures all the fabrication-related imperfections (instead of using averaged cavity parameters from the SEM image) can be employed in

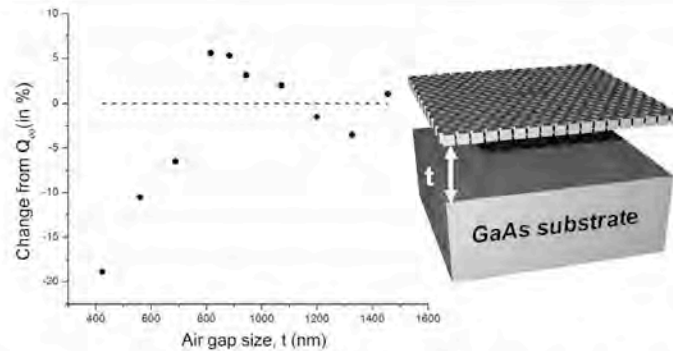


Figure 5. Variation of Q_{rad} with slab-to-substrate air gap for a slab of thickness 190 nm and a cavity mode at 1026 nm. (The other device parameters are the same as the L3 cavity shown in table 1.) The dashed line corresponds to $Q_{\infty} = 67\,315$ when there is no substrate in the vicinity of the slab. All data is obtained by 3D FDTD tools

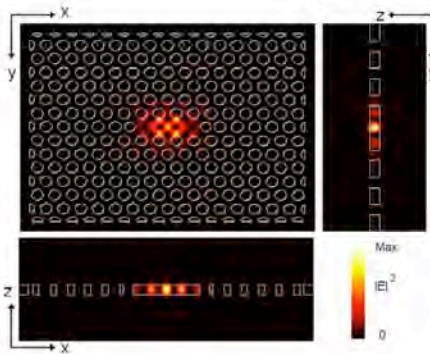


Figure 6. Electric-field intensity profiles from a contour FDTD simulation (contour data superimposed) for the three symmetry planes of the photonic-crystal cavity.

3D FDTD simulations [28]. As is evident from figure 1(c), the electric-field intensity distribution $(|\vec{E}(\vec{r})|^2)$ of the L3 mode reveals strongly localized patterns around the four air holes nearest to the cavity centre. Recalling the fact that the Q of the L3 mode is highly sensitive to the fine tuning of the nearest air holes [6], even minute deviations from the ideal geometry can severely degrade Q_{scat} and this can be quantified using contour FDTD.

The extracted contour plot and simulated $|\vec{E}(\vec{r})|^2$ for the structure mentioned above are shown in figure 6, in which a grid resolution of $\Delta x = \Delta y = \Delta z \approx 10$ nm is employed [10]. The Q obtained in this way drops to 21 283, which is still large but becomes closer to the measured value of 10 050. The remaining discrepancy can be attributed to non-vertical air holes, side-wall roughness and material losses that cannot be incorporated in a contour FDTD simulation. Finally, for a more realistic Q value, an air gap and GaAs substrate are included. The Q value in the presence of a 800 nm air gap is

23 576, showing about 10% improvement in comparison with the structure without the air gap.

4.4. Crystal-axis-dependent surface roughness

As we have recently reported [16], the underside of the GaAs slab can have wavy undulations that show an RMS roughness of the order of 25 nm, while maintaining an extremely smooth top surface. First by transmission electron microscopy, and then by atomic force microscopy (AFM), it was observed that the magnitude of the roughness was greater along the $[110]$ direction than the $[1\bar{1}0]$ direction. To test whether this crystal-axis-dependent roughness had any bearing on cavity Q s, several pairs of identical cavities were fabricated with the cavity long axis (the line joining the s -shifted holes in the case of the L3 designs) aligned along either of the directions mentioned above. It was found that, on average, cavities whose axis was aligned along the lower roughness direction had Q s that were 20–32% less (see figure 7(b)) than those aligned along the higher roughness direction. It must be noted that the overall Q s recorded in this experiment were low, on account of angled (non-vertical) walls of the photonic-crystal holes. Figure 7(a) shows the AFM scan of one such low Q cavity. Growth improvements [16] have been detailed to ensure top and bottom slab surfaces with atomic smoothness and minimal contribution to scattering loss.

5. Conclusion

Several factors contributing to photon loss from photonic-crystal cavities designed for cQED experiments are identified and addressed. Among them are irregularities with fabrication, crystal-axis-dependent losses and the presence of a bottom substrate. Lithography issues can be corrected by ensuring a properly focused electron beam; etched side-walls can be made vertical by careful control of the Cl_2 flow direction during dry etch; crystal-axis-dependent losses can be eliminated by optimized growth that leads to smooth slab interfaces; remnant

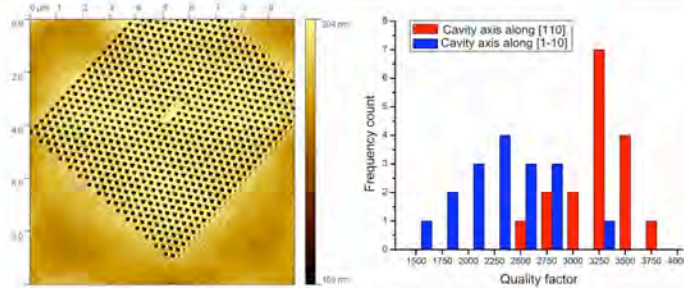


Figure 7. (a) Atomic force micrograph of a low Q L3 cavity whose axis is aligned along the low roughness crystal axis [110] (running from bottom left to top right in the image). (b) Histogram for Q values corresponding to the two different orientations of cavity and crystal axis.

resist can be removed by an oxygen plasma; debris left behind by the HF undercut can be removed by treating with KOH. Careful choice of sacrificial (AlGaAs) layer thickness can enhance cavity Q . The use of contour FDTD as a diagnostic tool for estimating cavity Q s is highlighted.

Acknowledgments

The authors gratefully acknowledge support (EEC-0812072) from the National Science Foundation (NSF) through the Engineering Research Center for Integrated Access Networks (CIAN). The Caltech authors acknowledge critical support and infrastructure provided for this work by the Kavli Nanoscience Institute at Caltech. The Tucson group also acknowledges support from NSF Atomic Molecular and Optical Physics (AMOP) and Electronics, Photonics and Device Technologies (EPDT), AFOSR, and Arizona Technology and Research Initiative Funding (TRIF). HMG thanks the Alexander von Humboldt Foundation for a Renewed Research Stay.

References

- [1] Yablonovitch E 1987 *Phys. Rev. Lett.* **58** 2059–62
- [2] John S 1987 *Phys. Rev. Lett.* **58** 2486–9
- [3] Englund D, Fattal D, Waks E, Solomon G, Zhang B, Nakaoka T, Arakawa Y, Yamamoto Y and Vuckovic J 2005 *Phys. Rev. Lett.* **95** 013904
- [4] Yoshie T, Scherer A, Hendrickson J, Khitrova G, Gibbs H M, Rupper G, Eli C, Shchekin O B and Deppe D G 2004 *Nature* **432** 200–3
- [5] Press D, Gotzinger S, Reitzenstein S, Hofmann C, Löffler A, Kamp M, Forchel A and Yamamoto Y 2007 *Phys. Rev. Lett.* **98** 117402
- [6] Akahane Y, Asano T, Song B-S and Noda S 2003 *Nature* **425** 944–7
- [7] Painter O, Vuckovic J and Scherer A 1999 *J. Opt. Soc. Am. B* **16** 275–85
- [8] Johnson S G and Joannopoulos J D 2001 *Opt. Express* **8** 173–90
- [9] Johnson S G, Fan S, Villeneuve P R, Joannopoulos J D and Kolodziejski L A 1999 *Phys. Rev. B* **60** 5751
- [10] Farjadpour A, Roundy D, Rodriguez A, Ibanescu M, Bermel P, Joannopoulos J D, Johnson S G and Burr G 2006 *Opt. Lett.* **31** 2972–4
- [11] Mandelstam V A and Taylor H S 1997 *J. Chem. Phys.* **107** 6756–69
- [12] Park H G, Hwang J K, Huh J, Ryu H Y, Kim S-H, Kim J S and Lee Y-H 2002 *IEEE J. Quantum Electron.* **38** 1553
- [13] Nozaki K and Baba T 2006 *Appl. Phys. Lett.* **88** 211101
- [14] Khitrova G, Gibbs H M, Kira M, Koch S W and Scherer A 2006 *Nat. Phys.* **2** 81–90
- [15] Strauf S, Hennessy K, Rakher M T, Choi Y S, Badolato A, Andreani L C, Hu E L, Petroff P M and Bouwmeester D 2006 *Phys. Rev. Lett.* **96** 127404
- [16] Sweet J et al 2009 *Photon. Nanostruct. Fundament. Appl.* doi:10.1016/j.photonics.2009.10.004
- [17] Michael C P, Srinivasan K, Johnson T J, Painter O, Lee K H, Hennessy K, Kim H and Hu E 2007 *Appl. Phys. Lett.* **90** 051108
- [18] Hendrickson J et al 2005 *Phys. Rev. B* **72** 193303
- [19] Villeneuve P R, Fan S, Johnson S G and Joannopoulos J D 1998 *IEEE Proc. Optoelectron.* **145** 384
- [20] Kim M-K, Yang J-K, Lee Y-H and Hwang I-K 2007 *J. Korean Phys. Soc.* **50** 1027–31
- [21] Tanaka Y, Asano T, Akahane Y, Song B-S and Noda S 2003 *Appl. Phys. Lett.* **82** 1661–3
- [22] Takayama S-T, Kitagawa H, Tanaka Y, Asano T and Noda S 2005 *Appl. Phys. Lett.* **87** 061107
- [23] Wen F, David S, Checoury X, Kurdi M E and Boucaud P 2008 *Opt. Express* **16** 12278–89
- [24] Ohlinger K, Lun Y and Qualls J S 2009 *J. Appl. Phys.* **106** 063520
- [25] Kim S-H, Kim S-K and Lee Y-H 2006 *Phys. Rev. B* **73** 235117
- [26] Vuckovic J, Englund D, Fattal D, Waks E and Yamamoto Y 2006 *Physica E* **32** 466–70
- [27] Hinds E A 1994 *Cavity Quantum Electrodynamics* ed P R Berman (New York: Academic)
- [28] Englund D and Vuckovic J 2006 *Opt. Express* **14** 3472–83



GaAs photonic crystal slab nanocavities: Growth, fabrication, and quality factor

J. Sweet^{a,*}, B.C. Richards^a, J.D. Olitzky^a, J. Hendrickson^a, G. Khitrova^a,
H.M. Gibbs^a, D. Litvinov^b, D. Gerthsen^b, D.Z. Hu^c, D.M. Schaadt^c,
M. Wegener^c, U. Khankhoje^d, A. Scherer^d

^a College of Optical Sciences, The University of Arizona, 1630 E. University Blvd., Tucson, AZ 85721, United States

^b Laboratorium für Elektronenmikroskopie, Universität Karlsruhe (TH), Wolfgang-Gaede-Strasse 1, D-76131 Karlsruhe, Germany

^c Institut für Angewandte Physik and DFG-Center for Functional Nanostructures (CFN), Universität Karlsruhe (TH),
Wolfgang-Gaede-Strasse 1, D-76131 Karlsruhe, Germany

^d Department of Electrical Engineering, California Institute of Technology, 1200 E California Blvd.,
Pasadena, CA 91125, United States

Received 29 July 2009; received in revised form 1 October 2009; accepted 23 October 2009

Available online 3 November 2009

Abstract

In an effort to understand why short wavelength (~ 1000 nm) GaAs-based photonic crystal slab nanocavities have much lower quality factors (Q) than predicted (and observed in Si), many samples were grown, fabricated into nanocavities, and studied by atomic force, transmission electron, and scanning electron microscopy as well as optical spectroscopy. The top surface of the AlGaAs sacrificial layer can be rough even when the top of the slab is smooth; growth conditions are reported that reduce the AlGaAs roughness by an order of magnitude, but this had little effect on Q . The removal of the sacrificial layer by hydrogen fluoride can leave behind a residue; potassium hydroxide completely removes the residue, resulting in higher Q s.

© 2009 Elsevier B.V. All rights reserved.

PACS: 81.07.b; 42.70.Qs

Keywords: Nanostructure fabrication; Microcavities; Photonic crystals; Integrated optics devices; Photonic integrated circuits

The small volume of a photonic crystal slab nanocavity makes it attractive for low-threshold lasing [1] and, with high-quality-factor designs [2], for semiconductor quantum optics, especially strong coupling between a single quantum dot and a single cavity mode [3–9]. The quality factor Q (cavity frequency ν divided by FWHM cavity linewidth) in a few cases has exceeded 15,000 [3,8,10,11] for fabrica-

tions on samples intended for strong coupling. More typically it is less than 10,000, particularly for the wavelength λ in the range 900–1000 nm where Si detectors greatly improve measurements. Very high- Q values have been computed for various cavity designs, but fabricated Q s are always much higher in silicon than in the GaAs system. In fact, a Q of 45,000 was already reported [2] in silicon for the L3 design used in [3] and throughout this article; optimization of that design has yielded 150,000 computationally [12] and 110,000 experimentally in Si (1.5 μm) [13]. This paper reports that whereas reducing the roughness of the top of the AlGaAs sacrificial layer did not improve Q noticeably,

* Corresponding author. Tel.: +1 520 548 4107;

fax: +1 866 705 9514.

E-mail address: jsweet@optics.arizona.edu (J. Sweet).

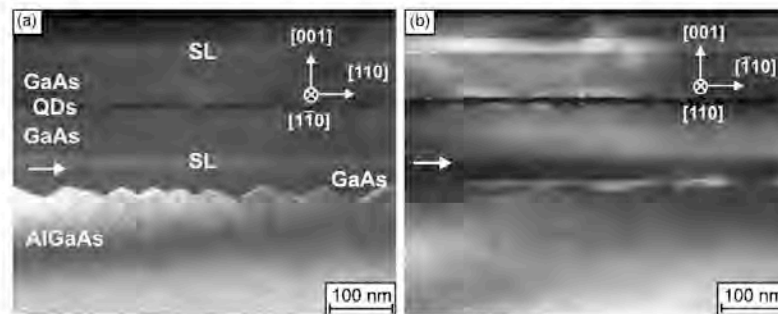


Fig. 1. (0 0 2) dark-field cross-section TEM images of PC sample showing that AlGaAs (light) roughness is greater along (a) [1 1 0] than (b) [−1 1 0]. The growth of GaAs (dark) almost flattens the surface by the time the first superlattice (SL) is grown (see arrows). The growth sequence of PC: GaAs buffer, ~700 nm $\text{Al}_{0.94}\text{Ga}_{0.06}\text{As}$ grown as a superlattice, 37.5 nm GaAs, 17.5 nm superlattice, 70 nm GaAs, 7.8 nm InGaAs quantum well with a layer of InAs quantum dots one-quarter in, 70 nm GaAs, 17.5 nm superlattice, and 37.5 nm GaAs.

using potassium hydroxide (KOH) to remove debris left behind in etching away the AlGaAs sacrificial layer did increase Q appreciably.

1. Reducing roughness at the top of the AlGaAs sacrificial layer

One of the diagnostics that can be used to evaluate a sample before fabrication is to scan the surface by atomic force microscopy (AFM). Scans ($40\ \mu\text{m} \times 40\ \mu\text{m}$) of our samples typically gave root mean square (r.m.s.) values around 1 nm, indicating smooth top surfaces consistent with scanning electron microscopy (SEM) images of the fabricated nanocavities. Cross-section transmission electron microscopy (TEM) images of the sample used for our initial observation of vacuum Rabi splitting [3] revealed that the AlGaAs/GaAs interface is rough; see Fig. 1. TEM images of three of our samples grown for fabrication in the 900–1000 nm wavelength range looked almost as rough. The smoothing accomplished by growth of the first few monolayers of GaAs helped to conceal this problem, as shown in Fig. 1 – which also shows that the roughness is much larger along [1 1 0] than along [1 −1 0].

What characteristics must the sacrificial layer have? The Al content x of the $\text{Al}_x\text{Ga}_{1-x}\text{As}$ needs to be in the range between 0.55 and 0.90 for etching with hydrofluoric (HF) acid. For $x > 0.90$ the etch rate is so fast that it is impractical to use an HF etch; steam oxidation of the AlGaAs in a furnace permits the use of a KOH wet etch, but it also introduces another step in fabrication which can be avoided by choosing a lower Al content. For $x < 0.55$ the etch rate is impractically slow. The AlGaAs needs to be thick enough to prevent light leakage to the substrate once the sacrificial layer

has been removed; a thickness of 800–1000 nm is often used for $900 < \lambda < 1200$ nm of interest here. The growth of smooth AlAs layers in Bragg mirror structures in vertical cavity surface emitting lasers (VCSELs) and planar microcavities is easier; the AlAs layer is typically only 70 nm thick and alternates with a similar thickness GaAs layer which smoothens any roughness at the top of the AlAs layer. The growth of smooth $\text{Al}_x\text{Ga}_{1-x}\text{As}$ in heterojunction lasers is also easier because x rarely exceeds 0.4.

Once the AlGaAs roughness was discovered, a quick and effective approach was taken to optimize the molecular beam epitaxy (MBE) growth: stop after growing $\text{Al}_x\text{Ga}_{1-x}\text{As}$, immediately remove the sample, and scan it by AFM. Growth parameters investigated included introducing a growth interruption to give time for smoothing under As, growing a thin layer of GaAs, and using a misoriented substrate. Most structures can be grown as well on a flat substrate as on one polished with the normal to the surface tilted a few degrees toward a particular crystal axis. However, it is known that the growth of AlGaAs is preferentially along step edges lying along [1−10]. If the surface is perfectly flat, then the surface diffusion may be inadequate to reach such an edge and island formation and 3D growth can result. This is consistent with Fig. 1 where it was found that the AlGaAs surface is rougher along [1 1 0] than along [1 −1 0]. Therefore, if one has not yet identified the ideal conditions for growth on a flat substrate, growth on a tilted substrate may be flatter. Consequently, growth on (0 0 1) GaAs substrates misoriented by 2° toward [1 1 0] was tried. As summarized in Table 1, several samples grown under approximately the same conditions showed that using a tilted substrate instead of a flat substrate and increasing the number of monolayers of GaAs always

Table 1
Summary of samples, growth parameters, and resulting surface.

Sample	x	Periods	AlGaAs (nm)	GaAs (ML)	GI (s)	Cut ($^{\circ}$)	r.m.s. (nm)
QD24	0.7	1	1000	0	0	0	1.27*
QD29	0.7	12	100	7	120	0	0.83*
QD30	0.7	10	100	0.5	120	2	3.5
QD31	0.7	1	1000	0	0	0	27
QD33	0.5	1	10	0	0	0	0.69
QD35	0.52	100	10	2	21	0	1.86
QD37	0.51	100	10	2	21	2	1.14
QD38	0.8	81	10	0.5	21	0	3.8
QD39	0.75	80	10	0.7	21	2	2.0
QD41	0.75	80	10	0.5	21	2	1.14*
A0947	0.55	80	10	0.85	21	0	1.3
A0950	0.75	5	160	0	60	0	0.41
A0961	0.75	2	400	0.5	120	0	0.4*

Notation: “ x ” is Al concentration in AlGaAs; “Periods” is the number of times the sequence AlGaAs, GaAs, growth interruption was repeated; “AlGaAs” is the thickness of AlGaAs grown before the growth of GaAs of thickness “GaAs” (“ML” is monolayer = 0.283 nm) followed by a growth interruption of duration “GI”; “Cut” is the substrate misorientation angle; the root mean square AFM surface roughness is “r.m.s.”, and values marked with an asterisk (*) indicate the top of the GaAs slab, not grown on the other samples. QD31, grown like the AlGaAs in QD24, is representative of our AlGaAs before the present study.

decreased the r.m.s. value. However, the GaAs thickness needs to be less than one monolayer (ML) for good etching of the sacrificial layer. It was also found that decreasing the ratio of the As flux to the sum of the Al and Ga fluxes from 26 to 13 decreased the roughness. The results discussed so far were for samples grown in Tucson using a Riber 32 MBE machine. The substrate temperature was 570–580 $^{\circ}$ C. The Al concentration x was changed by varying the Ga flux, holding the Al flux constant; the AlGaAs growth rate was about 0.63 (0.86) ML/s for $x = 0.75$ (0.55). Even flatter AlGaAs was grown on a Riber Compact 21 MBE machine at the University of Karlsruhe (samples beginning with “A” in Table 1). There the growth rate was about 0.858 ML/s calibrated by reflection high energy electron diffraction (RHEED) oscillations, and the As_4 pressure was typically

8×10^{-4} Pa, roughly half that used in Tucson ($(1.5\text{--}2.1) \times 10^{-4}$ Pa). RHEED patterns were observed several times during each growth to monitor flatness and to keep the V/III flux ratio close to but above the transition to Ga-stabilized surface structure, leading to flatter growth.

2. Q values of nanocavities with smoother AlGaAs

Having determined growth conditions for AlGaAs flatter by an order of magnitude, we began growing complete structures, i.e., slabs on top of the $\text{Al}_x\text{Ga}_{1-x}\text{As}$. For examples, see QD41 and A0961 in Table 1, where the r.m.s. values are now for the top of the GaAs slab. The TEM images in Fig. 2 verify that the AlGaAs is much flatter than in Fig. 1. The nanocavity Q

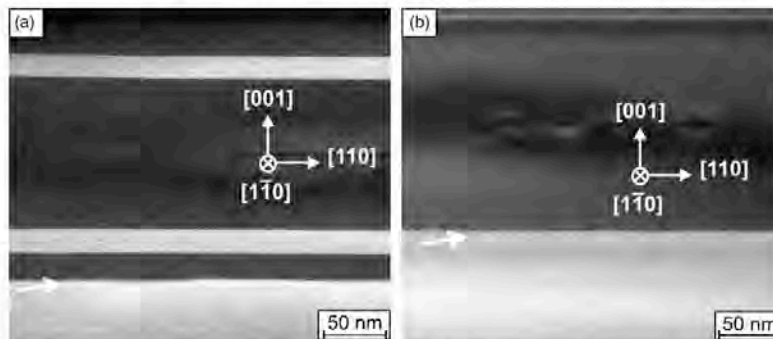


Fig. 2. (002) dark-field cross-section TEM images of (a) QD41 and (b) A0961 showing successful growth of flatter AlGaAs sacrificial layers (marked by arrows).

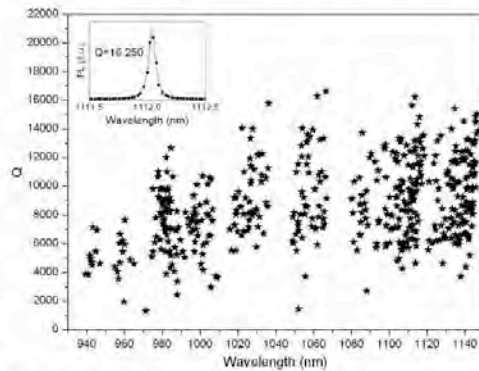


Fig. 3. Quality factors versus wavelength for A0961-3; cavities with $Q < 4000$ were not measured usually. The inset shows the photoluminescence spectrum for one of the highest Q s, and the blue curve is a Lorentzian fit to the data.

values of these samples were measured via their photoluminescence spectra with cw nonresonant excitation at 780 nm. The fabrication run A0961-3 yielded the Q values plotted in Fig. 3; a Q of 16,250, one of the highest Q s found, is shown in the inset. For comparison, the highest Q value obtained on rough-AlGaAs samples for $\lambda < 1000$ nm was 9000, whereas it reached 20,000 at $\lambda \cong 1200$ nm [10]. Therefore the data in Fig. 3 spanning 200 nm are consistent with the disjoint rough-AlGaAs data. This agreement means that taking the trouble to grow smoother AlGaAs did not improve the Q with our present fabrication quality. Fig. 3 shows little change in Q for wavelengths longer than 1020 nm, suggesting that Q may be limited by

non-vertical holes or fluctuations of hole shapes rather than Rayleigh scattering from imperfections which should increase as λ^4 . QD ensemble absorption and surface state absorption may cause the reduction in Q for short wavelengths.

3. KOH dip

The results just described for A0961-3 were obtained after the fabricated sample was dipped in a KOH solution (25 g/100 ml of deionized water) for 140 s just before it was placed in the cryostat and evacuated. This last step was added after an inspection of the SEM micrographs (Fig. 4a) revealed the presence of a semi-transparent object partially covering two holes in the upper left of the micrograph. AFM scans (Fig. 5) revealed the density and height variation of the debris and confirmed the hypothesis that this debris had floated and settled on the top of the slab after a successful dry etch. Speculating that this debris originated during the wet etch in the HF acid solution (1:10 = HF:H₂O by volume) and was probably a hydroxide of aluminum, we dipped the sample in a KOH solution. As is evident from the AFM scans, this process removed the debris completely. The effect of the KOH cleaning of surface debris on 10 different cavities was pronounced, showing an average improvement of 50%. One particular nanocavity from fabrication run A0961-3 showed a 73% improvement in Q from 4500 to 7800. Photoluminescence intensity also increased substantially, and the cavity modes shifted to higher energy on average 11 meV for all KOH treated cavities; see Fig. 4b for typical data.

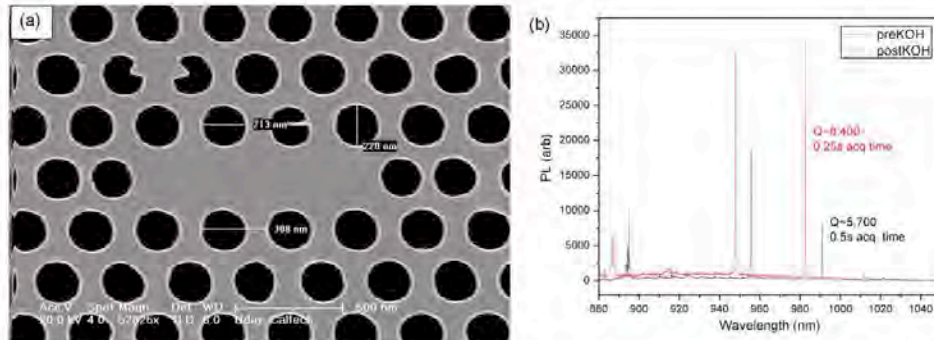


Fig. 4. (a) SEM image of part of one nanocavity in the fabrication run A0961-3 after O₂ plasma cleaning but before KOH cleaning. The lighter colored debris can be seen partially covering holes two and three in the second row and in several other locations. (b) Microphotoluminescence from a particular nanocavity of the fabrication run A0961-3 before and after KOH cleaning.

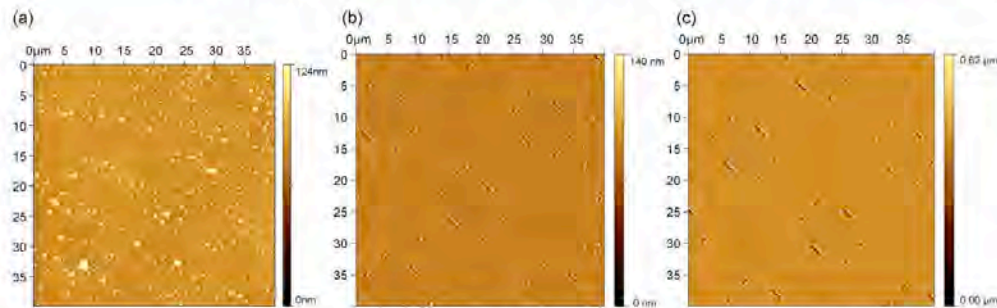


Fig. 5. AFM images of a few nanocavities of the fabrication run A0961-2 after O_2 plasma cleaning and (a) before swishing in a KOH solution (1.25 g KOH in 10 ml H_2O), (b) after 60 s, and (c) after 140 s. The bright yellow spots in (a) and (b) are debris that exceed 50 nm in height; the one in the bottom left corner of (a) exceeds 600 nm.

4. Summary

It was discovered by TEM that the top of the high-Al AlGaAs sacrificial layer in many of our MBE samples grown for fabrication of photonic crystal slab nanocavities is rough – even though the top surface of the sample (the top of the GaAs slab) is relatively flat, as had already been determined by AFM. MBE growth conditions were found that decrease the AlGaAs roughness by more than an order of magnitude. The improved smoothness will eventually be important for fabrication of high- Q nanocavities although its contribution at present is small. In addition, the efficacy of KOH in removing residue left behind in etching away the sacrificial layer is demonstrated.

Acknowledgements

HMG and GK would particularly like to thank Art Gossard and Mark Wistey for very helpful comments and suggestions on MBE growth of AlGaAs and L.C. Andreani for useful discussions on disorder. The USA authors would like to acknowledge support (EEC-0812072) from the National Science Foundation (NSF) through the Engineering Research Center for Integrated Access Networks (CIAN). The Tucson group also acknowledges support from NSF Atomic Molecular and Optical Physics (AMOP) and Electronics, Photonics and Device Technologies (EPDT), AFOSR, and Arizona Technology & Research Initiative Funding (TRIF). HMG thanks the Alexander von Humboldt Foundation for a Renewed Research Stay. The Caltech authors gratefully acknowledge critical support and infrastructure provided for this work by the Kavli

Nanoscience Institute at Caltech. The Karlsruhe researchers acknowledge financial support from the Deutsche Forschungsgemeinschaft (DFG) and the State of Baden-Württemberg through the DFG-Center for Functional Nanostructures (CFN) within subprojects A1.4 and A2.6.

References

- [1] O. Painter, R.K. Lee, A. Scherer, A. Yariv, J.D. O'Brien, P.D. Dapkus, I. Kim, Two-dimensional photonic band-gap defect mode laser, *Science* 284 (1999) 1819–1821.
- [2] Y. Akahane, T. Asano, B.S. Song, S. Noda, High- Q photonic nanocavity in a two-dimensional photonic crystal, *Nature* 425 (2003) 944–947.
- [3] T. Yoshie, A. Scherer, J. Hendrickson, G. Khitrova, H.M. Gibbs, G. Rupper, C. Ell, O.B. Shchekin, D.G. Deppe, Vacuum Rabi splitting with a single quantum dot in a photonic crystal nanocavity, *Nature* 432 (2004) 200–203.
- [4] J.P. Reithmaier, G. Sek, A. Löffler, C. Hofmann, S. Kuhn, S. Reitzenstein, L.V. Keldysh, V.D. Kulakovskii, T.L. Reinecke, A. Forchel, Strong coupling in a single quantum dot-semiconductor microcavity system, *Nature* 432 (2004) 197–200.
- [5] G. Khitrova, H.M. Gibbs, M. Kira, S.W. Koch, A. Scherer, Vacuum Rabi splitting in semiconductors, *Nat. Phys.* 2 (2006) 81–90.
- [6] K. Hennessy, A. Badolato, M. Winger, D. Gerace, M. Atature, S. Gulde, S. Falt, E.L. Hu, A. Imamoglu, Quantum nature of a strongly coupled single quantum dot-cavity system, *Nature* 445 (2007) 896–899.
- [7] D. Englund, A. Faraon, I. Fushman, N. Stoltz, P. Petroff, J. Vučković, Controlling cavity reflectivity with a single quantum dot, *Nature* 450 (2007) 857–861.
- [8] M. Winger, A. Badolato, K.J. Hennessy, E.L. Hu, A. Imamoglu, Quantum dot spectroscopy using cavity quantum electrodynamics, *Phys. Rev. Lett.* 101 (2008) 226808.
- [9] S.M. Thon, M.T. Rakher, H. Kim, J. Gadat, W.T.M. Irvine, P.M. Petroff, D. Bouwmeester, Strong coupling through optical positioning of a quantum dot in a photonic crystal cavity, *Appl. Phys. Lett.* 94 (2009) 111115.

- [10] J. Hendrickson, B.C. Richards, J. Sweet, S. Mosor, C. Christenson, D. Lam, G. Khitrova, H.M. Gibbs, T. Yoshie, A. Scherer, O.B. Shchekin, D.G. Deppe, Quantum dot photonic-crystal-slab nanocavities: quality factors and lasing, *Phys. Rev. B* 72 (2005) 193303.
- [11] J. Fushman, D. Englund, A. Faraon, J. Vučković, Probing the interaction between a single quantum dot and a photonic crystal cavity, *Phys. Status Solidi (c)* 5 (2008) 2808–2815.
- [12] L.C. Andreani, D. Gerace, A. Agio, Gap maps, diffraction losses, and exciton-polaritons in photonic crystal slabs, *Photon. Nanostruct.* 2 (2004) 103–110.
- [13] M. Galli, S.L. Portalupi, M. Belotti, L.C. Andreani, L. O'Faolain, T.F. Krauss, Light scattering and Fano resonances in high- Q photonic crystal nanocavities, *Appl. Phys. Lett.* 94 (2009) 071101.

Characterization of 1D photonic crystal nanobeam cavities using curved microfiber

B. C. Richards,^{1,†} J. Hendrickson,¹ J. D. Olitzky,¹ R. Gibson,¹ M. Gehl,¹ K. Kieu,¹
U. K. Khankhoje,² A. Homyk,² A. Scherer,² J.-Y. Kim,³ Y.-H. Lee,³ G. Khitrova,¹
H. M. Gibbs,¹

¹College of Optical Sciences, The University of Arizona, Tucson, AZ 85721, USA

²Electrical Engineering, California Institute of Technology, Pasadena, CA 91125, USA

³Department of Physics, Korea Advanced Institute of Science and Technology, Daejeon 305-701, Korea
brichards@optics.arizona.edu

Abstract: We investigate high- Q , small mode volume photonic crystal nanobeam cavities using a curved, tapered optical microfiber loop. The strength of the coupling between the cavity and the microfiber loop is shown to depend on the contact position on the nanobeam, angle between the nanobeam and the microfiber, and polarization of the light in the fiber. The results are compared to a resonant scattering measurement.

©2010 Optical Society of America

OCIS codes: (350.4238) Nanophotonics and photonic crystals; (140.3948) Microcavity devices

References and links

1. T. Yoshie, A. Scherer, J. Hendrickson, G. Khitrova, H. M. Gibbs, G. Rupper, C. Ell, O. B. Shchekin, and D. G. Deppe, "Vacuum Rabi splitting with a single quantum dot in a photonic crystal nanocavity," *Nature* **432**, 200-203 (2004).
2. D. Englund, D. Fattal, E. Waks, G. Solomon, B. Zhang, T. Nakaoka, Y. Arakawa, Y. Yamamoto, and J. Vučković, "Controlling the spontaneous emission rate of a single quantum dot in a two dimensional photonic crystal," *Phys. Rev. Lett.* **95**, 013904 (2005).
3. D. Press, S. Gotzinger, S. Reitzenstein, C. Hofman, A. Löffler, M. Kamp, A. Forchel, and Y. Yamamoto, "Photon antibunching from a single quantum-dot-microcavity system in the strong coupling regime," *Phys. Rev. Lett.* **98**, 117402 (2007).
4. G. Khitrova, H. M. Gibbs, M. Kira, S. W. Koch, and A. Scherer, "Vacuum Rabi splitting in semiconductors," *Nat. Phys.* **2**, 81-90 (2006).
5. U. K. Khankhoje, S.-H. Kim, B. C. Richards, J. Hendrickson, J. Sweet, J. D. Olitzky, G. Khitrova, H. M. Gibbs, and A. Scherer, "Modelling and fabrication of GaAs photonic-crystal cavities for cavity quantum electrodynamics," *Nanotechnology* **21**, 065202 (2010).
6. J. Sweet, B. C. Richards, J. D. Olitzky, J. Hendrickson, G. Khitrova, H. M. Gibbs, D. Litvinov, D. Gerthsen, D. Z. Hu, D. M. Schaadt, M. Wegener, U. Khankhoje, and A. Scherer, "GaAs photonic crystal slab nanocavities: Growth, fabrication, and quality factor," *Photonics and Nanostructures - Fundamentals and Applications* **8**, 1-6 (2010).
7. M. W. McCutcheon, G. W. Rieger, I. W. Cheung, J. F. Young, D. Dalacu, S. Frédrick, P. J. Poole, G. C. Aers, and R. L. Williams, "Resonant scattering and second-harmonic spectroscopy of planar photonic crystal microcavities," *Appl. Phys. Lett.* **87**, 221110 (2005).
8. D. Englund, A. Faraon, I. Fushman, N. Stoltz, P. Petroff, and J. Vučković, "Controlling cavity reflectivity with a single quantum dot," *Nature* **450**, 857-861 (2007).
9. K. Srinivasan, P. E. Barclay, M. Borselli, and G. Painter, "Optical-fiber-based measurement of an ultrasmall volume high-Q photonic crystal microcavity," *Phys. Rev. B* **70**, 081306(R) (2004).
10. I.-K. Hwang, G.-H. Kim, and Y.-H. Lee, "Optimization of coupling between photonic crystal resonator and curved microfiber," *IEEE J. of Quantum Electron.* **42**, 131-6 (2006).
11. P. Dootare, M. McCutcheon, I. Frank, M. Khan, and M. Lončar, "High quality factor photonic crystal nanobeam cavities," *Appl. Phys. Lett.* **94**, 121106 (2009).
12. C. Sauvan, P. Lalanne, and J. Hugonin, "Slow-wave effect and mode-profile matching in photonic crystal microcavities," *Phys. Rev. B* **71**, 1-4 (2005).
13. A. Oskooi, D. Roundy, M. Ibanescu, P. Bermel, J. Joannopoulos, and S. Johnson, "MEEP: A flexible free-software package for electromagnetic simulations by the FDTD method," *Comput. Phys. Commun.* **181**, 687702 (2010).

#131274 - \$15.00 USD
(C) 2010 OSA

Received 7 Jul 2010; revised 3 Sep 2010; accepted 4 Sep 2010; published 13 Sep 2010
27 September 2010 / Vol. 18, No. 20 / OPTICS EXPRESS 20558

14. A. R. M. Zain, N. P. Johnson, M. Sorel, and R. M. De La Rue, "Ultra high quality factor one dimensional photonic crystal/photonic wire micro-cavities in silicon-on-insulator (SOI)," *Opt. Express* **16**, 12084-12089 (2008).
15. M. Galli, S. L. Portalupi, M. Belotti, L. C. Andreani, L. O'Faolain, and T. F. Krauss, "Light scattering and Fano resonances in high-Q photonic crystal nanocavities," *Appl. Phys. Lett.* **94**, 071101 (2009).
16. S. Mosor, J. Hendrickson, B. C. Richards, J. Sweet, G. Khitrova, H. M. Gibbs, T. Yoshie, A. Scherer, O. B. Shchekin, and D. G. Deppe, "Scanning a photonic crystal slab nanocavity by condensation of xenon," *Appl. Phys. Lett.* **87**, 141105 (2005).

1. Introduction

The use of photonic crystal nanocavities as a means of confining light has led to an active field of cavity quantum electrodynamics research in the solid state. Specifically, the interaction between such confined fields and matter has led to the observation of a number of fundamental quantum optics results in semiconductors [1-3]. The primary way of enhancing such interactions between light and matter is to increase the ratio of quality factor Q to effective mode volume V . Increasing Q provides longer photon storage times, which leads to a greater chance of interaction between the light and the matter. Decreasing V leads to higher field intensities in the cavity, and hence stronger interactions between the light and the matter. High Q and small V are pursued by the semiconductor cavity QED community because they are essential for large Purcell enhancement ($F_p \propto Q/V$) of spontaneous emission and for a large vacuum Rabi splitting ($VRS \propto Q\sqrt{V}$) [1, 2, 4-6].

Cavity QED experiments with quantum dots (QDs) as the active emitters are usually performed at cryogenic temperatures. In this temperature regime, radiative recombination of excited carriers is the dominant decay mechanism, and hence the dots are easily studied by optical spectroscopic techniques. As a result, the standard technique of measuring cavity Q s using QD photoluminescence usually requires expensive helium cryostats. Since characterizing cavity Q s is a time consuming task for researchers in this field, techniques have been developed to enable measuring Q s independently of the active emitters, and hence at room temperatures. Measuring a probe signal in a cross-polarized resonant scattering configuration [7-8] and using a tapered microfiber probe [9-10] are two such techniques that have been developed and employed specifically for semiconductor cavity QED.

We report the results of our investigations of 1D photonic crystal nanobeam cavities by means of a microfiber tapered loop. Using this method to investigate silicon nanobeams on a silica substrate, we have measured the highest Q/V ratio reported for such devices. We present the results of these experiments, as well as a comparison between the two methods of cross-polarized resonant scattering and tapered fiber transmission. We observe an asymmetric lineshape of the cavity modes using both approaches, and show that the asymmetry can be varied in the case of the tapered fiber by varying the input polarization of the probe field.

2. Photonic crystal design and fabrication

The cavity considered here is a nanobeam cavity, which is essentially a wavelength-scale Fabry-Perot etalon formed by sandwiching a 1D photonic crystal waveguide between 1D photonic crystal Bloch mirrors, as shown in Figure 1. In the transverse directions, the light is confined in the nanobeam by total internal reflection. By smoothly tapering the air hole radius and the corresponding lattice constants in the mirror sections, the scattering loss is minimized and a high Q is achieved [11-12]. 3D finite-difference time-domain (FDTD) simulations [13] reveal that the cavity exhibits a reasonably high Q in excess of 500,000 with very low mode volumes, even though it is placed on a low index substrate. The region of tapered holes in the center of the nanobeam effectively confines the light, analogous to a Fabry-Perot spacer.

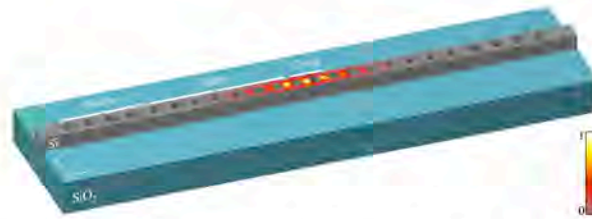


Figure 1. Schematic of cavity geometry with normalized electric field energy density $|E|^2$ through mid-plane of Si slab showing maximum concentration in cavity region. With the lattice constant in the mirror section as "a", the tapered section lattice constant ranges from 0.98a to 0.86a in 0.02a decrements, ending in the cavity section with 0.84a. Hole radius is 0.3 times the local lattice constant. For a 220 nm Si slab on bulk SiO₂ with a = 410 nm, the computed Q is 519,083 at $\lambda = 1490$ nm and mode volume $V = 0.27(\lambda/n)^3$ with $n = 3.53$.

The nanobeams are fabricated using electronics grade silicon-on-insulator with a 220 nm silicon device layer and 2 μm buried oxide. To prepare the samples for electron-beam lithography, the wafers are manually cleaved, cleaned with acetone and isopropanol, and the native oxide is removed by a short dip in 10:1 buffered hydrofluoric acid. The samples are then baked at 180 °C, spin-coated with 2 percent PMMA 950K in chlorobenzene, and baked again at 180 °C for 5 minutes. Electron-beam lithography is performed in a Leica EBPG 5000+ at 100kV. Following electron-beam exposure, the samples are developed in 1:3 MIBK:IPA for 60 seconds, rinsed in IPA, and dried with nitrogen. After development, the wafers are etched using an Oxford Instruments Plasmalab System100 ICP380 with a mixed-mode gas chemistry consisting of SF₆ and C₄F₈. Figure 2 shows SEM images of one of our nanobeam cavities.

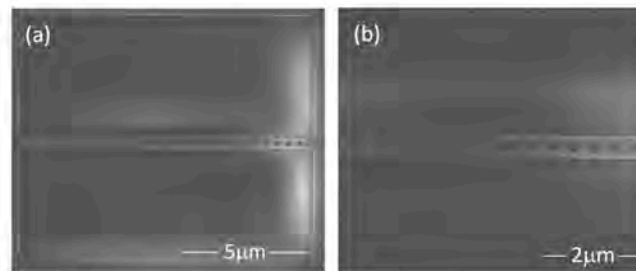


Figure 2. (a) SEM image of a nanobeam cavity. (b) SEM image of the center of a nanobeam, showing region of tapered holes.

3. Fiber transmission measurement

We investigate the spectral response of our nanobeam cavities by means of a curved, tapered optical fiber. The taper is fabricated in two stages. In the first stage, a Corning SMF-28 optical fiber is heated and stretched to a diameter of 1 μm , in which the tapered region operates in a single mode at 1.55 μm . In the second stage, mechanical translation stages are used to form the taper into a highly curved loop with typically 90 μm radius of curvature. The fiber taper loop is mounted onto a motorized xyz stage and brought into contact with the nanobeam cavity. The loop has proven very robust, as we have used the same loop for ten months so far.

without any problems. An Agilent 8164A mainframe with an Agilent 81682A tunable laser with 0.2 pm wavelength resolution is input into the fiber equipped with an inline polarization compensator before propagating through the tapered region. The transmitted light is detected at the output end of the fiber by an InGaAs photodiode. The laser is tuned across the cavity resonance, and the interaction of the light with the cavity mode can be observed as a change in the transmitted intensity of the propagating field. The laser needs to have resolution better than the FWHM of the cavity mode and amplitude fluctuations must be slower than the time to scan across a mode. The Q is the transition energy of the mode divided by the FWHM energy width of the cavity mode. The nanobeam sample is mounted on a stage rotating about an axis normal to the sample, so that the angle between the tapered fiber and the axis of the nanobeam cavity can be varied. Figure 3 (a) shows a typical fiber loop transmission spectrum of a nanobeam cavity, with two cavity modes visible.

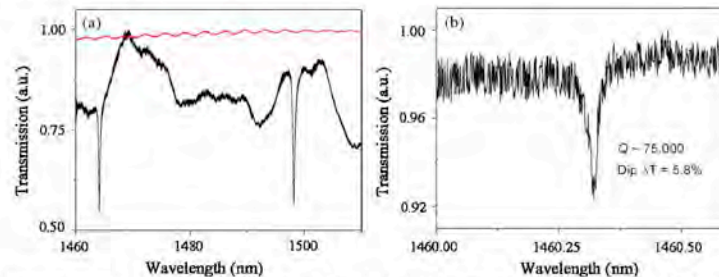


Figure 3. (a) Fiber loop transmission spectrum of a typical nanobeam cavity at 45° center contact (black) and spectrum directly from laser (red). (b) Fiber loop transmission spectrum of a high- Q nanobeam cavity mode, at 45° edge contact, with $Q = 75,000$.

4. Fiber coupling to a nanobeam

By nature of the physical interaction between the field in the fiber taper and the nanobeam, a degradation of the cavity Q is expected. This is due to an additional source of losses contributed by the fiber taper, as the measurement is now of the coupled fiber-cavity system. However, the losses introduced by the presence of the fiber taper can be mitigated by careful selection of the contact parameters. The first parameter we adjust is the contact length of the fiber loop on the nanobeam. The presence of the fiber on the nanobeam introduces a loss channel. Hence, longer contact length between the fiber loop and the nanobeam reduces the Q . The fiber taper loop is brought in toward the nanobeam using small steps on a motorized actuator. At some critical distance from the sample surface, Van der Waals and electrostatic forces pull the fiber taper in, causing it to stick to the surface. Once the loop is in contact with the nanobeam, the actuator can still be advanced, increasing pressure and the contact length between the fiber taper and the nanobeam. The actuator can also be pulled away slowly while the loop is still stuck to the surface, decreasing the contact length. After sufficient force is applied to pull the loop away by overcoming the sticking force, it pops off the surface of the sample.

The second parameter we adjust is the contact position along the length of the nanobeam. We have confirmed that the weakest coupling, and therefore the highest Q , is observed when contact is made as close as possible to the edge of the nanobeam, whereas contact in the center of the nanobeam produces the strongest coupling and hence the lowest Q . Contact in the center of the nanobeam also modifies the local index of refraction in the vicinity of the cavity, which changes the effective index of the cavity mode and leads to a shift in the resonance frequency. The extra loss due to the presence of the fiber taper in the center of the nanobeam and subsequent degradation of the Q is dramatic. Figure 4 shows a plot of cavity

mode resonant wavelength and Q as a function of position on a high- Q nanobeam. Clearly one wants to avoid contact with the center of the nanobeam for measuring high Q s. Because the coupling between fiber and nanobeam decreases away from the center of the nanobeam, we found that on very high Q nanocavities it is not possible to take Q measurements all the way to the edge of the nanobeam. This is the case with the nanobeam studied in Figure 4, where the measurements extend between $\pm 4 \mu\text{m}$, whereas the nanobeam extends to $\pm 6 \mu\text{m}$. Measurements more than $4 \mu\text{m}$ from the center of this nanobeam yielded no perceptible dip in transmission. On lower Q nanocavities the measurements can usually be taken up to the very edge of the nanobeam. This observation is consistent with the fact that on high Q nanocavities the electric field is more tightly confined toward the center of the nanobeam.

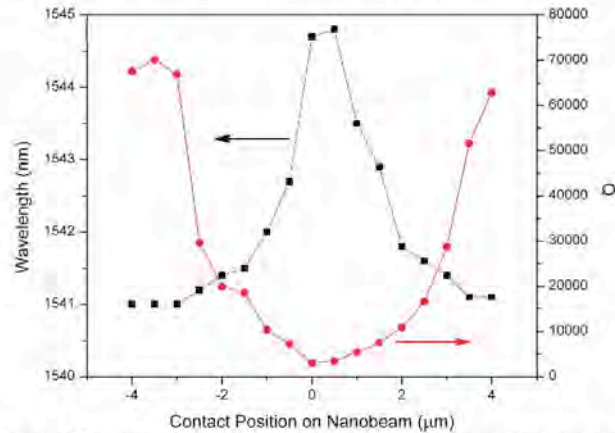


Figure 4. Fiber loop transmission measurements as a function of position on a typical nanobeam cavity at 45° (center of nanobeam corresponds to $0 \mu\text{m}$ and the attached edges to $\pm 6 \mu\text{m}$), cavity mode resonant wavelength (black squares) and Q (red circles).

The third parameter we adjust is the angle between the fiber taper and the axis of the nanobeam cavity. Because the polarization of the input field is always perpendicular to the axis of the fiber, the angle between the fiber and the nanobeam will affect the coupling to the mode of the nanobeam, which is linearly polarized perpendicular to the axis of the nanobeam. One would expect that the best polarization matching would occur when the nanobeam is aligned parallel to fiber. However, this configuration also produces the strongest coupling between the field in the fiber and the nanocavity, as well as the largest index modification in the vicinity of the cavity. Even when the contact is made at the edge of the nanobeam, the length of the contact region between the fiber and the nanobeam extends over a large fraction of the nanobeam. Hence, this configuration produces a deep dip in the transmitted signal, but does not yield the highest measured Q s. One might think that the perpendicular configuration between the fiber and the nanobeam would yield the highest Q s because of minimized contact between them as well as minimal coupling into the nanobeam. However, because of the drastically reduced coupling in the perpendicular configuration due to orthogonal polarizations, we were not able to observe any cavity modes in that configuration at the edge of the nanobeam. The highest Q s result with an angle ranging from 20° to 60° between the fiber taper and the nanobeam, and contact made at the edge of the nanobeam. This configuration reduces the physical contact between the fiber and the nanobeam compared to the parallel configuration, but still supports a polarization component that is matched to the

nanobeam mode. The highest Q we measured was 75,000 with a computed mode volume of $0.27(\lambda/n)^3$ in the 45° , edge configuration, yielding $Q/V = 278,000$. As far as we know, this yields the highest Q/V ratio that has been achieved on nanobeam cavities on substrate. The group of De La Rue [14] reported a Q of 147,000 with a computed mode volume of $0.85(\lambda/n)^3$, yielding $Q/V = 173,000$. Figure 3 (b) shows the spectrum of the highest Q nanobeam cavity mode.

5. Comparison to resonant scattering

As mentioned earlier, the presence of a fiber taper in contact with a nanobeam cavity provides an additional loss mechanism for light in the cavity. While this allows us to probe the Q of the system by measuring the transmission through the fiber, it also reduces the Q compared to the inherent Q that the cavity would have by itself. In order to investigate this loss mechanism, we have compared the results of measurements with the fiber taper loop to measurements performed by cross-polarized resonant scattering, as shown in Figure 5. [7-8, 11].

Cavity modes measured using resonant scattering are known to exhibit asymmetric lineshapes [15]. These lineshapes are attributed to a Fano interference between the resonantly scattered light and the coherent background. In order to extract a linewidth from such an asymmetric profile, we fit the signal to a Fano lineshape:

$$F(\omega) = A_0 + F_0 \frac{[q + 2(\omega - \omega_0)/\Gamma]^2}{1 + [2(\omega - \omega_0)/\Gamma]^2} \quad (1)$$

where ω_0 is the frequency of the cavity mode transition, Γ is the resonance linewidth, A_0 and F_0 are offset and scaling factors, respectively, and q is the Fano parameter that quantifies the asymmetry of the lineshape. Adjusting these parameters to fit a curve to our resonant scattering data, we are able to extract the underlying linewidth, and hence Q of the cavity mode. Such a fit is shown in Figure 5 (b), using Equation (1) with fit parameters $A_0 = 0.658$, $F_0 = 0.054$, $q = 0.6$, $\omega_0 = 30.9$ THz and $\Gamma = 0.7$ GHz. Galli, et al have reported [15] that the asymmetry of the lineshape from resonant scattering data can be varied by changing the spot size of the laser beam on the sample.

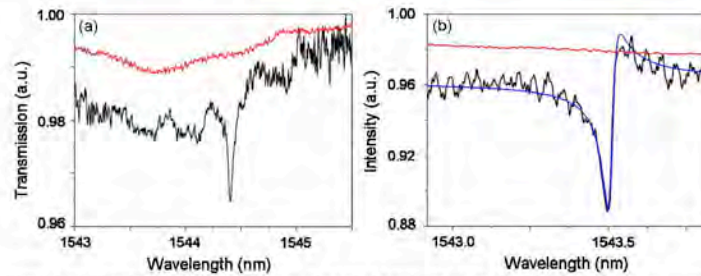


Figure 5. (a) Fiber loop transmission spectrum of a typical nanobeam cavity, $Q = 29,000$ (black) and spectrum directly from laser (red). (b) Cross-polarized resonant scattering signal of the same nanobeam cavity as (a), $Q = 44,100$ (black); fitted Fano lineshape (blue); spectrum directly from laser (red).

Cavity modes measured using the fiber taper also displayed asymmetric lineshapes, which we attribute to interference between two pathways: light interacting with the cavity mode and emitted back into the fiber and light coupled into the 2D slab. However, unlike the case with the resonant scattering technique, the asymmetry of the lineshape with the fiber taper

technique is strongly dependent on polarization. Hence, it was always possible to tune the polarization such that the resulting lineshape was symmetric, and this allowed us to directly fit a Lorentzian lineshape in order to extract the Q , without resorting to the more complicated fitting associated with the Fano Equation (1). The Q s measured using the resonant scattering technique were higher than those measured for the same cavity using the 45° fiber configuration at the edge of the nanobeam, consistent with the idea that the presence of the fiber loop lowers the Q by introducing an additional loss mechanism. The loss induced by the presence of the fiber taper is typically substantial, as the difference in Q s that we observed using the two methods showed the fiber loop measurement to be 38% lower on average than the resonant scattering measurement.

How do the two systems compare in other ways? The fiber taper loop measurement is more difficult to set up than the resonant scattering measurement, primarily because of the equipment and experience needed to successfully taper and curve the microfibers. Once the measurement is set up, the fiber taper loop measurement is quite robust and does not suffer from the extreme sensitivity to variations in alignment of the resonant scattering technique. Both measurements can be performed at room temperature or at cryogenic temperatures; however, the fiber taper measurement would require extensive modifications to most cryostats in order to insert the fiber taper and control its motion. In contrast, the resonant scattering technique can be performed with all of the optics outside of the cryostat. The fiber taper measurement is performed in an all-fiber configuration, whereas the resonant scattering method is performed in free space. We found that absorption lines due to atmospheric nitrogen in the spectral region of our nanobeam cavity modes also appear as dips in the measured resonant scattering spectrum. In order to accurately measure the Q of a cavity mode coincident with an absorption dip, as was unfortunately the case for the $Q = 75,000$ cavity in Fig. 3 (b), the mode would need to be spectrally shifted away from the absorption dip by a technique such as heating or condensation of xenon or nitrogen gas [16].

6. Conclusion

In conclusion, we have measured the Q s of 1D photonic crystal nanobeam cavities on substrate using the transmitted signal through a fiber taper loop. Using this technique, we have measured a Q as high as 75,000 with a computed mode volume of $0.27(\lambda/n)^3$, representing the highest Q/V ratio reported in this system. We have observed dependence of the measured Q on contact position and length between the nanobeam and the fiber taper, angle between the nanobeam and the fiber taper, and polarization of the light in the fiber. We have observed that higher Q s are measured when the fiber loop is contacted at the edge of the nanobeam and with a 20° to 60° angle between the fiber loop and the nanobeam. We have shown that the fiber taper loop technique is capable of measuring high Q s, and that by tuning the polarization in the fiber it is possible to eliminate the asymmetric lineshapes.

Acknowledgments

The USA authors would like to acknowledge support (EEC-0812072) from the National Science Foundation (NSF) through the Engineering Research Center for Integrated Access Networks (CIAN). The Tucson group also acknowledges support from NSF Atomic Molecular and Optical Physics (AMOP) and Electronics, Photonics and Device Technologies (EPDT), AFOSR, and Arizona Technology & Research Initiative Funding (TRIF). The Caltech authors gratefully acknowledge critical support and infrastructure provided for this work by the Kavli Nanoscience Institute at Caltech. HMG thanks the Alexander von Humboldt Foundation for a Renewed Research Stay. AH appreciates the generous support of the ARCS Foundation. The Tucson group thanks the groups of Prof. Jelena Vučković and Prof. Edo Waks for helpful discussions regarding the resonant scattering technique. The authors thank Pavel Polynkin for the use of his Agilent mainframe and tunable laser.

Effect of atomic layer deposition on the quality factor of silicon nanobeam cavities

Michael Gehl,^{1,*} Ricky Gibson,¹ Joshua Hendrickson,² Andrew Homyk,³ Antti Säynätjoki,⁴ Tapani Alasaarela,⁴ Lasse Karvonen,⁴ Ari Tervonen,⁴ Seppo Honkanen,⁴ Sander Zandbergen,⁵ Benjamin C. Richards,⁶ J. D. Olitzky,¹ Axel Scherer,³ Galina Khitrova,¹ Hyatt M. Gibbs,¹ Ju-Young Kim,⁸ and Yong-Hee Lee⁶

¹College of Optical Sciences, University of Arizona, 1630 East University Boulevard, Tucson, Arizona 85721, USA

²Air Force Research Laboratory, Sensors Directorate, 2241 Avionics Circle, Building 600, Wright Patterson Air Force Base, Ohio 45433, USA

³Electrical Engineering and Kavli Nanoscience Institute, California Institute of Technology, MC 200-36, 1200 East California Boulevard, Pasadena, California 91125, USA

⁴Department of Micro- and Nanosciences, Aalto University School of Electrical Engineering, P.O. Box 13500, 00076 Aalto, Finland

⁵Advanced Concepts Team, Emcore Corporation, 10420 Research Road, Albuquerque, New Mexico 87123, USA

⁶Department of Physics, Korea Advanced Institute of Science and Technology, Daejeon 305-701, Korea

*Corresponding author: mgehl@optics.arizona.edu

Received October 4, 2011; revised December 12, 2011; accepted December 12, 2011; posted December 12, 2011 (Doc. ID 155915); published January 25, 2012

In this work we study the effect of thin-film deposition on the quality factor (Q) of silicon nanobeam cavities. We observe an average increase in the Q of $38 \pm 31\%$ in one sample and investigate the dependence of this increase on the initial nanobeam hole sizes. We note that this process can be used to modify cavities that have larger than optimal hole sizes following fabrication. Additionally, the technique allows the tuning of the cavity mode wavelength and the incorporation of new materials, without significantly degrading Q . © 2012 Optical Society of America

OCIS codes: 350.4238, 310.1860, 310.6860.

1. MOTIVATION

Photonic crystal (PC) cavities provide exciting platforms for photonics applications in addition to fundamental cavity quantum electrodynamics (c-QED) experiments. The ability to fabricate cavities with small mode volumes (V) and large Q s leads to large enhancements in light-matter interactions. By placing active emitters such as quantum dots (QDs) into the cavity, it is easy to observe Purcell enhancement of spontaneous emission with only modest Q s. Increasing the Q further leads to the quantum regime of strong coupling, in which energy is able to coherently transfer between the emitter and cavity multiple times before decaying. This regime leads to exciting new physics, such as the Jaynes-Cummings ladder, deterministic single-photon sources, and photon blockades [1–3].

In addition to a high Q and low V , it is important that the cavity and emitter be near resonance with each other. Previous work has shown the ability to reversibly tune cavity resonances by 5 nm using the condensation of gases at low temperatures [4]. Additionally, tuning of 2D photonic crystal systems has been shown using atomic layer deposition (ALD) of hafnium oxide [5] and titanium oxide [6] and plasma-enhanced chemical vapor deposition of silicon nitride [7]. In this work, we observe a shift in cavity resonance of 20 to 29 nm, with a high tuning precision as a result of the multiple-cycle deposition process.

Finally, it is important that one can incorporate an active medium with the cavity. While this can be achieved with

QDs and quantum wells in III–V systems, it presents more of a challenge for silicon photonics. In this work, we show the ability to deposit new material on top of a silicon PC cavity with a minimal effect on the Q . This opens up the possibility of incorporating active materials through similar methods. For example, one can dope Al_2O_3 with layers of erbium during the deposition process [8].

2. NANOBEAM CAVITIES

One PC cavity geometry that is becoming popular is the 1D nanobeam, shown in Fig. 1. This design consists of a strip waveguide with an array of etched holes. The holes begin with uniform radius and spacing, creating a Bragg mirror region. The hole radius and spacing are then tapered down to a cavity region where the mode is confined, before tapering back up to another mirror region. The holes confine the light along one dimension, while it is confined by index guiding along the other two. The substrate can be etched from underneath the cavity, leaving it suspended, or in the case of this work, the cavity can remain on the substrate for increased durability. Simulations of unsuspended cavities predict Q s as high as 366,000 with a mode volume of $0.552(\lambda/n)^3$. Experimentally, unsuspended silicon nanobeam cavities have already been measured with Q s of 360,000 [9].

In this work, nanobeams are fabricated on silicon-on-insulator wafers, consisting of a 220 nm silicon layer on top of a $2\ \mu\text{m}$ SiO_2 layer. The structure is defined using electron beam lithography and formed using inductively coupled



Fig. 1. (Color online) Schematic of the 1D nanobeam cavity with overlay of normalized electric field energy density.

plasma etching. Each nanobeam is characterized by a lattice constant " a ," which is the distance between the center of the holes in the mirror region. The value of a varies from 390 to 455 nm in 5 nm steps, shifting the cavity mode through the range of our measurement ability. In the taper region, the lattice constant varies from $0.98a$ to $0.86a$, while in the cavity region, the lattice constant is $0.84a$. The nominal hole radius is 0.3 times the local lattice constant.

3. CHARACTERIZATION BY MEASUREMENT OF THE CAVITY QUALITY FACTOR Q

In order to characterize the Q of silicon nanobeam cavities, we use the tapered microfiber probe technique [10,11]. In this technique, an optical fiber is heated and stretched, such that it adiabatically tapers to a region with a diameter on the order of $1\ \mu\text{m}$. This region of the fiber is then carefully positioned across the nanobeam cavity. A tunable narrowband laser source is coupled into one end of the fiber, and the transmitted power is detected at the other end. As the laser source is tuned into resonance with the cavity, some of the power is coupled into the cavity mode, resulting in a measurable dip in transmission through the fiber.

As a result of the tapered microfiber probe, the cavity experiences an additional amount of loss. This causes an increase in the measured resonance linewidth and thus a decrease in the measured Q compared to the intrinsic Q of the cavity. This effect was studied in [10], which found that by positioning the probe near the edge of the nanobeam, coupling to the cavity is minimized, leading to a measured Q closer to the intrinsic Q . For this study, all Q s are measured at the edge of the nanobeam cavity. Because of the positioning uncertainty of the probe, which leads to slight changes in the coupling and hence the measured Q , five measurements are taken of each cavity; the maximum value is used for all comparisons.

To determine the intrinsic Q of a cavity, we use the crossed polarizer resonant scattering technique [10,12]. This is a free space method in which a tunable laser source is focused onto the cavity with a microscope objective. The incident light is polarized at 45° with respect to the polarization of the cavity mode. The reflected light is passed through a polarizer at 90° relative to the incident light. Light that simply reflects from the substrate will be blocked by the crossed polarizer. Light that couples into the cavity will scatter out with the polarization of the cavity mode, a portion of which will be able to pass through the final polarizer and be detected. Because of the increased difficulty and low signal-to-noise ratio of this measurement, this technique is used only to determine the intrinsic Q of the best cavities.

4. ATOMIC LAYER DEPOSITION

Atomic layer deposition is a thin-film deposition process that works through the sequential application of two or more gas phase chemicals. The growth takes place as a chemical reaction at the sample surfaces. The reaction is self-limiting, allowing accurate control of film thickness simply by counting the number of cycles.

Because of the nature of this deposition technique, the resulting film is conformal and grows along the surface normal [13]. This effect has already been utilized to grow microlens arrays [14] and planarized optical gratings [15] and to tune photonic crystal waveguides [7,16]. The conformal film also reduces surface roughness, and ALD-grown Al_2O_3 and TiO_2 films have been found to significantly reduce propagation losses in silicon strip and slot waveguides [13,17]. Because the geometry of the silicon nanobeam cavity is a modified silicon strip waveguide, we believe that this process could lead to decreased losses and higher Q s in these structures.

For this work, we investigated the thin-film growth of both TiO_2 and Al_2O_3 on nanobeam cavities by ALD. TiO_2 is deposited at 120°C using a process with titanium tetrachloride (TiCl_4) and water as precursors [18]. Al_2O_3 is deposited at 200°C using a process with trimethylaluminum ($\text{Al}_2(\text{CH}_3)_6$) and water as precursors [19]. Figure 2 shows scanning electron micrograph (SEM) images of a cavity before and after the deposition of 20 nm of Al_2O_3 , showing a clear reduction in hole size due to the thin film.

5. EXPERIMENTAL RESULTS

For initial tests, two nanobeam samples were fabricated using the same design parameters. They were first characterized using the tapered microfiber technique. While imaging the

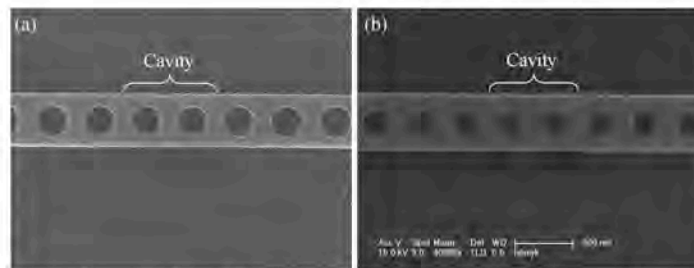


Fig. 2. SEM images of the cavity region of a silicon nanobeam (a) before and (b) after deposition of 20 nm Al_2O_3 by ALD.

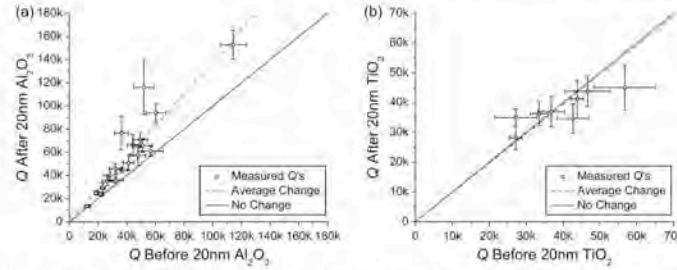


Fig. 3. (Color online) Q of several cavities after ALD plotted against the Q measured before ALD, for 20 nm of (a) Al_2O_3 and (b) TiO_2 . The solid line has a slope of 1 and represents no change in the Q , while the dotted line represents the average change of 38% for Al_2O_3 and -1.3% for TiO_2 .

cavities, it was noticed that there was residual mask material remaining from fabrication. This material was removed using a 10 min O_2 plasma etch. The cavities were recharacterized, and it was noted that the cavity wavelength decreased by 6.5 nm on average, but there was no significant change in cavity Q . One sample was then coated with 20 nm of TiO_2 (index 2.27 at $\lambda = 1.55 \mu\text{m}$), while the other was coated with 20 nm of Al_2O_3 (index 1.62 at $\lambda = 1.55 \mu\text{m}$). The samples were characterized again, following the same procedure. The TiO_2 (Al_2O_3) coated sample showed a shift in cavity mode of 59.2 ± 0.7 (30.3 ± 0.8) nm on average. The results of the Q measurements are plotted in Fig. 3. While one TiO_2 coated cavity showed an increase in Q of 29%, the average change in Q over all cavities was $-1.3 \pm 16\%$. Every Al_2O_3 coated cavity showed an increase in Q , with an average increase of $38 \pm 31\%$ and a maximum increase of 124%. The large standard deviation for this sample mostly results from 2 of the 19 cavities, which showed an increase of more than 100%. Figure 4 shows a measurement of a cavity from the Al_2O_3 -coated sample before and after deposition. This measurement was performed using the crossed polarizer resonant scattering technique, so the measured Q is that of the intrinsic Q . This shows the cavity Q to have increased from 107,000 to 212,000.

While the deposition of 20 nm of Al_2O_3 on that particular sample resulted in a clear increase in the cavity Q , from these initial tests it is not clear what factors contributed to this increase. The fact that the sample coated with TiO_2 did not show the same increases suggests that the effect is not exclusively due to a decrease in surface roughness. Finite-difference time-domain (FDTD) simulations of the silicon

nanobeam Q [Fig. 5(a)] indicate that the Q is highly dependent on the hole radius, with a peak Q near a radius of 0.3 times the lattice constant. To account for the decrease in hole radius as a result of the ALD coating, a third sample was fabricated with an added offset to the hole radius. For each lattice constant, 13 cavities were defined with offsets ranging from -30 to $+30$ nm in 5 nm steps. Four arrays of these cavities were fabricated with varying electron beam dosage, but only two arrays provided useful cavities.

This sample was characterized, coated with 20 nm of Al_2O_3 , and then recharacterized. Fifty-three of the 60 cavities that were characterized on this third sample showed increases in the Q , with the average increase being $20 \pm 19\%$. Figure 5(b) shows a plot of the measured Q prior to ALD coating as a function of hole radius offset. There is a trend toward higher Q s for cavities with smaller holes. Unlike the simulation, there is not a clear peak in the Q . This suggests that our range of hole sizes did not cover the designed range. Looking at the percent increase in the Q as a function of the hole radius offset (Fig. 6), there is also a clear trend toward a greater increase for cavities with larger holes. Following ALD, these cavities have hole sizes closer to those of the cavities that showed the highest Q s prior to ALD. This is consistent with the idea that the increase in Q is due to the shift of hole size closer to the optimal (highest Q) design.

Figure 7 shows a plot of the shift in the cavity mode wavelength as a result of the deposition of 20 nm of Al_2O_3 , along with FDTD simulation results. While the wavelength shift showed very little dependence on the lattice constant, it showed a strong dependence on the initial hole radius offset.

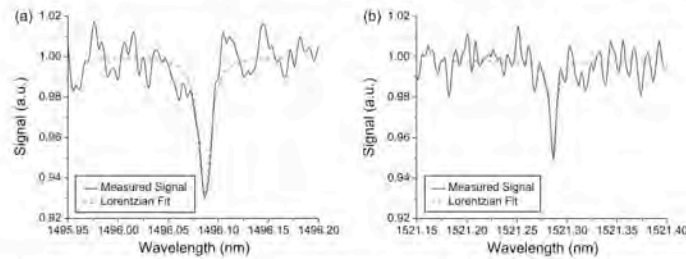


Fig. 4. (Color online) Crossed polarizer resonant scattering measurement of a cavity (a) before and (b) after being coated with 20 nm of Al_2O_3 , yielding a measured Q of 107,000 before and 212,000 after. The before data were collected prior to the O_2 plasma etch, which removed the mask residue and shifted the cavity peak to shorter wavelength by 6.5 nm.

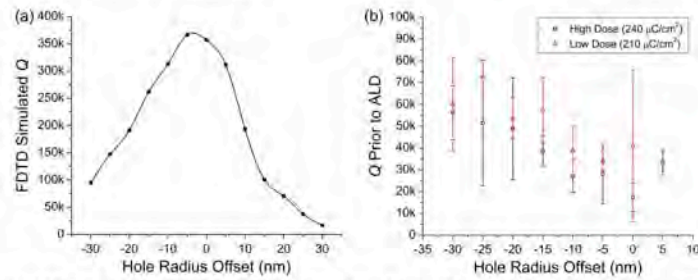


Fig. 5. (Color online) (a) FDTD simulation of the Q prior to ALD coating, showing the expected peak around 0 nm offset. The 0 nm offset corresponds to a hole radius of 0.3 times the lattice constant. (b) Plot of the average measured Q of several cavities prior to ALD coating versus the hole radius offset, showing a trend of higher Q for cavities with smaller holes (more negative offset). Dose refers to the dosage used during electron beam lithography.

The shift also showed some dependence on the dosage used during electron beam lithography. This is likely due to the dependence of the hole size and beam width on electron beam dose. The higher dose array, which should have larger holes due to the increased exposure of the mask, showed wavelength shifts in the range of 21.6 ± 0.2 nm for the smallest holes to 28.0 ± 0.1 nm for the largest holes. The lower dose array showed wavelength shifts in the range of 20.2 ± 0.2 nm for the smallest holes to 27.1 ± 0.4 nm for the largest. The FDTD simulations predict a similar range of wavelength shift. The tuning precision is very high because it is

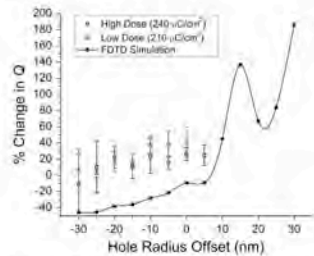


Fig. 6. (Color online) Plot of the average percent change in the Q of the cavities from Fig. 1 versus the initial hole radius offset, showing a trend of greater increase for cavities that began with larger holes (more positive offset). The FDTD results are plotted for comparison.

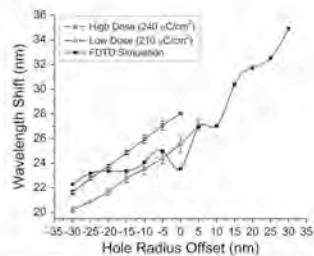


Fig. 7. (Color online) Plot of the average shift in wavelength of the cavity mode following ALD versus the hole radius offset, along with the FDTD simulation results.

determined by the growth rate of the thin film, which can be very slow. For the ALD technique used in this work, the growth rate was around 0.1 nm/cycle, with a cycle time of 3.45 s. This results in a wavelength shift on the order of 0.1–0.15 nm/cycle.

In order to investigate the effect of the Al_2O_3 coating on the mode volume, we use numerical methods. FDTD simulations reveal a nearly linear relationship between the mode volume and hole radius offset. The mode volume increases from $0.410(\lambda/n)^3$ for a +30 nm offset, to $0.658(\lambda/n)^3$ for a -30 nm offset. At the same time, the increase in mode volume as a result of depositing 20 nm of Al_2O_3 shows little dependence on the hole radius offset, fluctuating in the range of a 2.00% to 6.45% increase.

6. CONCLUSIONS

We have shown that ALD can be a valuable tool for tuning the resonant wavelength and Q of 1D silicon nanobeam cavities postfabrication. The low index and low deposition rate of Al_2O_3 allows for very precise control of the wavelength shift. The initial size of the cavity holes also plays an important role in the resonance shift. Cavities with smaller holes to begin with will have modes that are more confined to the silicon and therefore will see less of an effect from the additional dielectric material.

Initial results show that a 20 nm coating of Al_2O_3 can increase the Q of 1D silicon nanobeam cavities by $38 \pm 31\%$. While the exact nature of this change in the Q is not fully understood, both simulation and experiment show that the Q is significantly affected by the size of the cavity holes. Therefore, it is likely that the changing hole size resulting from the Al_2O_3 deposition is responsible for much of the change in the Q observed in this work. There still remains much to be done to determine the contribution of other effects to the change in the Q . The conformal nature of the ALD film will lead to decreased surface roughness and decreased scattering losses at the Al_2O_3 -air interface; however, the large index mismatch of Al_2O_3 and silicon means that scattering at this interface will still be significant. Additionally, the thin film could be causing surface passivation, leading to decreased absorption by surface states. Finally, the film may be affecting the mode profile, pulling the field away from the oxide layer and decreasing losses into the substrate. Repeating these experiments with

various materials and film thicknesses will reveal more detail on these separate effects.

In summary, the ability to deposit Al_2O_3 onto silicon nanobeams without significantly degrading the Q or increasing V is important for the field of silicon photonics and cQED. In addition to being able to tune the cavity resonance, the ability to incorporate new materials, such as erbium, will allow the fabrication of active devices from silicon PC cavities.

ACKNOWLEDGMENTS

M. Gehl acknowledges support by the Department of Defense (DoD) through the National Defense Science & Engineering Graduate Fellowship (NDSEG) program. S. Zandbergen acknowledges partial support from Arizona Technology & Research Initiative Funding (TRIF). J. Hendrickson acknowledges support from the Air Force Office of Scientific Research (AFOSR)—LRIR 10RY04COR (Gernot Pomrenke, program manager). A. Homyk appreciates the generous support of the ARCS Foundation. A. Säynätjöld was supported by Academy of Finland grant 134087 and a travel grant by the Finnish Foundation for Technology Promotion. The Caltech and UofA groups thank NSF ERC CIAN (EEC-0812072) for support. The UofA group acknowledges support from the AFOSR (FA9550-10-1-0003) and NSF EPMD (ECCS-1101341).

REFERENCES

1. P. R. Berman, *Cavity Quantum Electrodynamics* (Academic, 1994).
2. K. Vahala, *Optical Microcavities* (World Scientific, 2004).
3. G. Khitrova, H. M. Gibbs, M. Kira, S. W. Koch, and A. Scherer, "Vacuum Rabi splitting in semiconductors," *Nat. Phys.* **2**, 81–90 (2006).
4. S. Moser, J. Hendrickson, B. C. Richards, J. Sweet, G. Khitrova, H. M. Gibbs, T. Yoshie, A. Scherer, O. B. Shchekin, and D. G. Deppe, "Scanning a photonic crystal slab nanocavity by condensation of xenon," *Appl. Phys. Lett.* **87**, 052101 (2005).
5. X. Yang, C. J. Chen, C. A. Husko, and C. W. Wong, "Digital resonance tuning of high- Q/V_{∞} silicon photonic crystal nanocavities by atomic layer deposition," *Appl. Phys. Lett.* **91**, 161114 (2007).
6. S. Scharfner, S. Kalchauer, A. M. Andrews, P. Klang, W. Schrenk, and G. Strasser, "Post-fabrication fine-tuning of photonic crystal quantum well infrared photodetectors," *Appl. Phys. Lett.* **94**, 231117 (2009).
7. E. Graugnard, D. F. Gaillot, S. N. Dunham, C. W. Neff, T. Yamashita, and C. J. Summers, "Photonic band tuning in two-dimensional photonic crystal slab waveguides by atomic layer deposition," *Appl. Phys. Lett.* **89**, 181109 (2006).
8. K. Sohlmainen, M. Kapulainen, P. Heinola, and K. Polamo, "Erbium-doped waveguides fabricated with atomic layer deposition method," *IEEE Photon. Technol. Lett.* **16**, 194–196 (2004).
9. E. Kuramochi, H. Taniyama, T. Tanabe, K. Kawasaki, Y.-G. Roh, and M. Notomi, "Ultra-high- Q one-dimensional photonic crystal nanocavities with modulated mode-gap barriers on SiO_2 claddings and on air claddings," *Opt. Express* **18**, 15859–15869 (2010).
10. B. C. Richards, J. Hendrickson, J. D. Oltzky, R. Gibson, M. Gehl, K. Kieu, U. K. Khanikhoje, A. Homyk, A. Scherer, J.-Y. Kim, Y.-H. Lee, G. Khitrova, and H. M. Gibbs, "Characterization of 1D photonic crystal nanobeam cavities using curved microfiber," *Opt. Express* **18**, 20558–20564 (2010).
11. L.-K. Hwang, S.-K. Kim, J.-K. Yang, S.-H. Kim, S.-H. Lee, and Y.-H. Lee, "Curved-microfiber photon coupling for photonic crystal light emitter," *Appl. Phys. Lett.* **87**, 131107 (2005).
12. M. W. McCutcheon, G. W. Rieger, J. W. Cheung, J. F. Young, D. Dalacu, S. Frédéricik, P. J. Poole, G. C. Aers, and R. L. Williams, "Resonant scattering and second-harmonic spectroscopy of planar photonic crystal microcavities," *Appl. Phys. Lett.* **87**, 221110 (2005).
13. T. Alasaarela, D. Kom, L. Alloati, A. Säynätjöld, A. Tervonen, R. Palmer, J. Lenthold, W. Freude, and S. Honkanen, "Reduced propagation loss in silicon strip and slot waveguides coated by atomic layer deposition," *Opt. Express* **19**, 11529–11538 (2011).
14. J. J. Wang, A. Nikolov, and Q. Wu, "Nano- and microlens arrays grown using atomic-layer deposition," *IEEE Photon. Technol. Lett.* **18**, 2650–2652 (2006).
15. J. J. Wang, X. Deng, R. Varghese, and A. Nikolov, "Filling high aspect-ratio nano-structures by atomic layer deposition and its applications in nano-optic devices and integrations," *J. Vac. Sci. Technol.* **23**, 3209–3213 (2005).
16. D. Gaillot, E. Graugnard, J. Blair, and C. Summers, "Dispersion control in two-dimensional superlattice photonic crystal slab waveguides by atomic layer deposition," *Appl. Phys. Lett.* **91**, 181123 (2007).
17. A. Säynätjöld, L. Karvonen, T. Alasaarela, X. Tu, T. Y. Liow, M. Hiltunen, A. Tervonen, G. Q. Lo, and S. Honkanen, "Low-loss silicon slot waveguides and couplers fabricated with optical lithography and atomic layer deposition," *Opt. Express* **19**, 26275–26282 (2011).
18. T. Alasaarela, T. Saastamoinen, J. Hiltunen, A. Säynätjöld, A. Tervonen, P. Stenberg, M. Kuitinen, and S. Honkanen, "Atomic layer deposited titanium dioxide and its application in resonant waveguide grating," *Appl. Opt.* **49**, 4321–4325 (2010).
19. R. L. Paturmen, "Surface chemistry of atomic layer deposition: A case study for the trimethylaluminum/water process," *J. Appl. Phys.* **97**, 121301 (2005).

One dimensional resonant Fibonacci quasicrystals: noncanonical linear and canonical nonlinear effects

M. Werchner^{1*}, M. Schafer¹, M. Kira¹, S. W. Koch¹, J. Sweet²,
J. D. Oltzky², J. Hendrickson², B. C. Richards², G. Khitrova²,
H. M. Gibbs², A. N. Poddubny³, E. L. Ivchenko³,
M. Voronov³, and M. Wegener⁴

¹Department of Physics and Material Sciences Centre, Philipps-Universität, Renthof 5,
D-35032 Marburg, Germany

²College of Optical Sciences, The University of Arizona, Tucson, AZ 85721

³A. F. Ioffe Physico-Technical Institute, 194021 St. Petersburg, Russia

⁴Institut für Angewandte Physik and DFG-Center for Functional Nanostructures (CFN),
Universität Karlsruhe (TH), Wolfgang-Gaede-Strasse 1, D-76131 Karlsruhe, Germany

*Corresponding author: marco.werchner@physik.uni-marburg.de

Abstract: A detailed experimental and theoretical study of the linear and nonlinear optical properties of different Fibonacci-spaced multiple-quantum-well structures is presented. Systematic numerical studies are performed for different average spacing and geometrical arrangement of the quantum wells. Measurements of the linear and nonlinear (carrier density dependent) reflectivity are shown to be in good agreement with the computational results. As the pump pulse energy increases, the excitation-induced dephasing broadens the exciton resonances resulting in a disappearance of sharp features and reduction in peak reflectivity.

© 2009 Optical Society of America

OCIS codes: (190.5970) Semiconductor nonlinear optics including MQW; (160.5293) Photonic bandgap materials; (230.5590) Quantum-well, -wire and -dot devices.

References and links

1. D. Levine and B. J. Steinhardt, "Quasicrystals: A New Class of Ordered Structures," *Phys. Rev. Lett.* **53**, 2477–2480 (1984).
2. C. Janot, *Quasicrystals. A Primer* (Clarendon Press, Oxford, UK, 1994).
3. A. Ledermann, L. Cademartini, M. Hermatschweiler, C. Tonielli, G. A. Ozin, D. S. Wiersma, M. Wegener, and G. von Freymann, "Three-dimensional silicon inverse photonic quasicrystals for infrared wavelengths," *Nature Mater.* **5**, 942–945 (2006).
4. T. Matsui, A. Agrawal, A. Nahata, and Z. V. Vardeny, "Transmission resonances through aperiodic arrays of subwavelength apertures," *Nature* **446**, 517–521 (2007).
5. E. Yablonovitch, "Inhibited Spontaneous Emission in Solid-State Physics and Electronics," *Phys. Rev. Lett.* **58**, 2059–2062 (1987).
6. S. John, "Strong localization of photons in certain disordered dielectric superlattices," *Phys. Rev. Lett.* **58**, 2486–2489 (1987).
7. M. Kohmoto, B. Sutherland, and K. Iguchi, "Localization of optics: Quasiperiodic media," *Phys. Rev. Lett.* **58**, 2436–2438 (1987).
8. L. D. Negro, M. Stolfi, Y. Yi, J. Michel, X. Duan, L. C. Kimerling, J. LeBlanc, and J. Haavisto, "Photon band gap properties and omnidirectional reflectance in Si/SiO₂ Thue-Morse quasicrystals," *Appl. Phys. Lett.* **84**, 5186–5188 (2004).
9. A. N. Poddubny, L. Pilozzi, M. M. Voronov, and E. L. Ivchenko, "Resonant Fibonacci quantum well structures in one dimension," *Phys. Rev. B* **77**, 113306 (2008).

#107840 - \$15.00 USD Received 23 Feb 2009; revised 30 Mar 2009; accepted 1 Apr 2009; published 9 Apr 2009
(C) 2009 OSA 13 April 2009 / Vol. 17, No. 8 / OPTICS EXPRESS 6813

10. J. Hendrickson, B. C. Richards, J. Sweet, G. Khitrova, A. N. Poddubny, E. L. Ivchenko, M. Wegener, and H. M. Gibbs, "Excitonic polaritons in Fibonacci quasicrystals," *Opt. Express* **16**, 15382–15387 (2008).
11. R. Merlin, K. Bajema, R. Clarke, F. Y. Juang, and P. K. Bhattacharya, "Quasiperiodic GaAs-AlAs Heterostructures," *Phys. Rev. Lett.* **55**, 1768–1770 (1985).
12. M. Kohmoto and J. R. Banavar, "Quasiperiodic lattice: Electronic properties, phonon properties, and diffusion," *Phys. Rev. B* **34**, 563–566 (1986).
13. E. L. Albuquerque and M. G. Cottam, "Theory of elementary excitations in quasiperiodic structures," *Phys. Rep.* **376**, 225–337 (2003).
14. E. L. Ivchenko, *Optical spectroscopy of semiconductor nanostructures* (Alpha Science International, Harrow, UK, 2005).
15. M. Y. Azbel, "Energy spectrum of a conduction electron in a magnetic field," *Sov. Phys. JETP* **19**, 634–645 (1964).
16. M. Y. Azbel, "Quantum Particles in One-Dimensional Potentials with Incommensurate Periods," *Phys. Rev. Lett.* **43**, 1954–1957 (1979).
17. Z. Liu, M. Goda, and H. Kubo, "A family of generalized Fibonacci lattices: self-similarity and scaling of the wavefunction," *J. Phys. A* **28**, 853–866 (1995).
18. J. M. Luck, C. Godreche, A. Janner, and T. Janssen, "The nature of the atomic surfaces of quasiperiodic self-similar structures," *J. Phys. A* **26**, 1951–1999 (1993).
19. X. Fu, Y. Liu, P. Zhou, and W. Sitrakool, "Perfect self-similarity of energy spectra and gap-labeling properties in one-dimensional Fibonacci-class quasilattices," *Phys. Rev. B* **55**, 2882–2889 (1997).
20. M. Kofár, "New class of one-dimensional quasicrystals," *Phys. Rev. B* **47**, 5489–5492 (1993).
21. M. C. Valsakumar and V. Kumar, "Diffraction from a quasi-crystalline chain," *Pramana* **26**, 215–221 (1986).
22. Z. Liu, H. Kubo, and M. Goda, "Self-similarity and scaling of wave function for binary quasiperiodic chains associated with quadratic irrationals," *Z. Phys. B: Condensed Matter* **98**, 111–118 (1995).
23. D. Levine and P. J. Steinhardt, "Quasicrystals. I. Definition and structure," *Phys. Rev. B* **34**, 596–616 (1986).
24. E. L. Ivchenko, A. I. Nesvizhskii, and S. Jorda, "Bragg reflection of light from quantum-well structures," *Phys. Solid State* **36**, 1156–1161 (1994).
25. E. L. Ivchenko, M. M. Voronov, M. V. Eremenchouk, I. I. Deych, and A. A. Lisiansky, "Multiple quantum-well-based photonic crystals with simple and compound elementary supercells," *Phys. Rev. B* **70**, 195106 (2004).
26. M. Hübner, J. Kuhl, T. Stroucken, A. Knorr, S. W. Koch, R. Hey, and K. Ploog, "Collective Effects of Excitons in Multiple-Quantum-Well Bragg and Anti-Bragg Structures," *Phys. Rev. Lett.* **76**, 4199–4202 (1996).
27. M. Lindberg and S. W. Koch, "Effective Bloch Equations for Semiconductors," *Phys. Rev. B* **38**, 3342 (1988).
28. H. Haug and S. W. Koch, *Quantum Theory of the Optical and Electronic Properties of Semiconductors* (5th ed., World Scientific Publishing, Singapore, 2009).
29. M. Kira and S. W. Koch, "Many-body correlations and excitonic effects in semiconductor spectroscopy," *Prog. Quantum Elec.* **30**, 155–296 (2006).
30. E. Merzbacher, *Quantum Mechanics* (first ed., Wiley, New York, 1961).
31. M. Kira, E. Jalnik, W. Hoyer, and S. W. Koch, "Quantum theory of spontaneous emission and coherent effects in semiconductor microstructures," *Prog. Quantum Elec.* **23**, 189–279 (1999).
32. D. Hudin, A. Mysyrowicz, A. Antonetti, A. Migus, W. T. Masselink, H. Morkoc, H. M. Gibbs, and N. Peyghambarian, "An ultrafast all optical gate with subpicosecond on and off response time," *Appl. Phys. Lett.* **49**, 749–751 (1986).
33. Z. S. Yang, N. H. Kwong, R. Binder, and A. L. Smirl, "Stopping, storing, and releasing light in quantum-well Bragg structures," *J. Opt. Soc. Am. B* **22**, 2144–2156 (2005).
34. J. P. Prineas, W. J. Jobstun, M. Yildirim, J. Zhao, and A. L. Smirl, "Tunable slow light in Bragg-spaced quantum wells," *Appl. Phys. Lett.* **89**, 241106 (2006).
35. M. F. Yanik, W. Suh, Z. Wang, and S. Fan, "Stopping light in a waveguide with an all-optical analog of electromagnetically induced transparency," *Phys. Rev. Lett.* **93**, 233903 (2004).
36. P. Chak, S. Pereira, and J. E. Sipe, "Coupled-mode theory for periodic side-coupled microcavity and photonic crystal structures," *Phys. Rev. B* **73**, 035105 (2006).

1. Introduction

Quasicrystals form a class of solid materials characterized by an aperiodic but deterministic structural arrangement of elements that is intermediate between the ordered crystal and the amorphous structure [1, 2]. Light propagation in such systems is now extensively studied [3, 4]. Aperiodic deterministic structures can possess rotational symmetry of higher order than traditional photonic crystals [5, 6] and also allow for localized states of the light [7, 8]. Most of the previous studies of photonic quasicrystals were focused on passive structures.

In our works [9, 10], the study of the optical properties of the aperiodic lattices was extended

to resonant systems based on multiple quantum well (MQW) structures with two different inter-well distances satisfying the Fibonacci-chain rule with the golden ratio between the long and short inter-well distances. We focused on the linear light propagation in such a medium around the frequency ω_0 corresponding to the excitonic resonance of a quantum well (QW). The widths of the inter-well barriers were determined from the resonant Bragg condition [9], specifying the constructive interference of the waves reflected from the MQWs at the excitonic resonance. We chose to study the Fibonacci sequence because it is the most well-known example of 1D quasiperiodic structures; its distinctive features are a dense quasi-continuous pure point Fourier spectrum and a direct connection with the 2D and 3D quasicrystals, the Penrose lattices.

Since the inter-well barriers are of the order of half of the wavelength of the exciting light, the QWs are coupled only via the electromagnetic field. This is a strong qualitative difference between the considered system and short period semiconductor Fibonacci superlattices [11, 12], where the neighboring QWs are coupled by tunneling. When plasmon-polaritons are studied in aperiodic lattices [13], they are coupled through an evanescent electromagnetic field [14].

In our investigations, the QWs couple resonantly to the propagating light such that the excitonic resonance strongly modifies the optical response yielding the so-called excitonic polaritons. In the MQW Fibonacci structures the quasicrystalline long range order results in an excitonic polariton stopband similar to that of photonic crystals while the lack of periodicity in the quasicrystal results in efficient photoluminescence emission in the direction normal to the layer planes [10]. Due to these polariton features, our systems fundamentally differ from the light-emitting Thue-Morse structures based on non-resonant dielectrics studied before [8]. In those systems, the light-matter interaction is enhanced due to the formation of the localized states of light.

In this paper, we present a detailed study of the linear and nonlinear optical properties of different MQW Fibonacci structures. The detailed comparison between the theoretical results and the experiment for the molecular-beam-epitaxy-grown samples based on GaAs/AlGaAs Fibonacci MQWs is performed.

The Fibonacci chain $LSSLSSL\dots$ is the textbook example of a one-dimensional quasicrystalline structure sharing the name with the Fibonacci numbers due to the construction rule that the next complete sequence is the present sequence plus the previous sequence, labeling the first sequence as S and the second as L (corresponding below to short and long separations between quantum wells) [2]. Nevertheless, almost all previous studies were focused on the case when the ratio between the widths of long and short segments in the chain was equal to the golden mean. In this work, we bring into consideration the "noncanonical" Fibonacci structures where such a ratio is arbitrary. We present a general equation for the structure factor of the one-dimensional quasicrystalline chains, including "noncanonical" Fibonacci lattices, and formulate the generalized resonant Bragg condition for these systems.

The rest of the paper is organized as follows. In Sec. 2, we briefly discuss the general definitions of different one-dimensional quasicrystals and present the resonant Bragg condition. Section 3 is devoted to the description of the experimental setup and theoretical approaches used to study the Fibonacci MQW structures. Experimental and theoretical nonlinear reflectivity of the canonical Fibonacci structures is discussed in Sec. 4. In Sec. 5, we analyze the linear reflection spectra of different noncanonical Fibonacci structures tuned to and slightly detuned from the Bragg resonance. The brief summary of the main results is given in Conclusions.

2. One-dimensional quasicrystals and the structure factor

In this section, we present three equivalent definitions of quasicrystalline chains and find their general diffractive properties. The structure under consideration consists of N semiconductor QWs with their centers positioned at the points $z = z_m$ ($m = 1, \dots, N$) arranged in an aperiodic

lattice. Different approaches to introduce the concept of a one-dimensional quasicrystal go back to (i) the incommensurate chains, (ii) the substitution rules and (iii) the cut-and-project method.

The incommensurate chains and related structures [15, 16] are studied since the 1960s, even before the term "quasicrystal" was introduced in [1]. The coordinates of the QW centers are written in the form

$$z_m = z_0 + m\bar{d} + r(m), \quad (1)$$

where \bar{d} is the mean period of the lattice, z_0 is an arbitrary shift of the lattice as a whole, and the modulation $r(m)$ is the periodic function

$$r(m) = \Delta \left\{ \frac{m}{t} + \varphi \right\}, \quad (2)$$

where $\{x\}$ stands for the fractional part of x . Here Δ , t , and φ are the structure parameters, with t being irrational and φ being noninteger. At vanishing Δ , Eqs. (1) and (2) specify a simple periodic lattice with the period \bar{d} (without loss of generality we assume hereafter that $t > 1$). In the case of rational t , the structure is still periodic but has a compound supercell, whereas for irrational values of t Eq. (1) leads to a deterministic aperiodic chain termed also as "modulated crystal" [2]. The parameter Δ describes the modulation strength and the value of φ specifies the initial phase of the function $r(m)$. For z_m defined according to Eqs. (1) and (2), the physical spacings $z_{m+1} - z_m$ take one of the two values,

$$S_0 = \bar{d} + \Delta/t \quad \text{and} \quad L_p = \bar{d} + \Delta(1/t - 1). \quad (3)$$

In the following, we generally denote the large (small) QW spacing by L (S). In particular, we introduce the subscript "p" for the physical lengths of the spacings, L_p and S_p , while the optical pathlengths of these spacers are denoted as L_o and S_o . The value of Δ should not be too large so that the spacings L_p and S_p remain positive. Excluding Δ in Eqs. (3), one can find the relation

$$\bar{d} = S_p + (L_p - S_p)/t. \quad (4)$$

Moreover, the ratio N_S/N_L of numbers of the spacings L and S in an infinite lattice is related with t by

$$\frac{N_S}{N_L} = t - 1. \quad (5)$$

Under certain conditions imposed upon the values t and φ [17, 18], the QW arrangement can also be obtained by the substitution rules acting on the segments L and S as follows

$$\begin{aligned} L &\rightarrow \sigma(L) = \mathcal{A}_1 \mathcal{A}_2 \dots \mathcal{A}_{\alpha+\beta}, \\ S &\rightarrow \sigma(S) = \mathcal{A}_1 \mathcal{A}_2 \dots \mathcal{A}_{\gamma+\delta}. \end{aligned} \quad (6)$$

Each of the symbols \mathcal{A}_k and \mathcal{A}_k in the right-hand side of Eq. (6) stands for L or S , α and β denote the numbers of letters L and S in the sequence $\sigma(L)$, and γ and δ are the numbers of L and S in $\sigma(S)$, respectively [19]. The correspondence between the two definitions is established by the relation $t = 1 + (\lambda_1 - \alpha)/\gamma$ between a value of t and indices $\alpha, \beta, \gamma, \delta$, where $\lambda_1 = (v + \sqrt{v^2 + 4w})/2$, $v = \alpha + \delta$ and $w = \beta\gamma - \alpha\delta$. For the quasicrystals, w must be equal to ± 1 [20].

The structure described by Eqs. (1) and (2) can be equivalently defined by the cut-and-project method based on a projection from the two-dimensional space upon a straight line [21]. Sizes of the unit cell of the two-dimensional lattice (rectangular or oblique) are determined by the

ratio L_p/S_p of spacings Eq. (3). However, the order of the segments L and S is determined only by t and φ and can be obtained by the projection of the square lattice [22].

The optical properties of the chain, Eqs. (1) and (2), are described by its structure factor $f(q)$

$$f(q) = \lim_{N \rightarrow \infty} f(q, N), \quad f(q, N) = \frac{1}{N} \sum_{m=1}^N e^{2iqz_m}. \quad (7)$$

In the limit $N \rightarrow \infty$, the structure factor of a quasicrystal [23] consists of δ -peaks corresponding to the Bragg diffraction and characterized by two integer numbers h and h' , see [2, 18],

$$f(q) = \sum_{h, h' \rightarrow \infty} \delta_{2q, G_{hh'}} f_{hh'}, \quad (8)$$

with the diffraction vectors

$$G_{hh'} = \frac{2\pi}{d} \left(h + \frac{h'}{t} \right), \quad (9)$$

filling the wavevector axis in a dense quasicontinuous way. We point out that in the periodic lattice ($\Delta = 0$), the structure factor has non-zero peaks at the single-integer diffraction vectors $G_h = 2\pi h/d$ with $|f_h| = 1$. One can show that, for irrational values of t and $\Delta \neq 0$, the structure factor coefficients are given by

$$\begin{aligned} f_{hh'} &= \frac{\sin S_{hh'}}{S_{hh'}} e^{i\theta_{hh'}}, \quad \theta_{hh'} = (z_0 + \Delta(\varphi)) G_{hh'} + S_{hh'}, \\ S_{hh'} &= \frac{\pi \Delta h}{d} + \pi h' \left(1 + \frac{\Delta}{td} \right) = \pi h' + \frac{\Delta}{2} G_{hh'}. \end{aligned} \quad (10)$$

The above equations for the structure factor are valid for arbitrary values of the phase φ in Eq. (2) and are original to the best of our knowledge. For the specific case when $\varphi = 0$, they can be obtained by a straightforward transformation of the result presented in [21]. Although the absolute value of the structure factor is independent of φ , the order of segments L and S between the QWs determined by Eq. (1) does depend on this phase. On the other hand, Eq. (10) generalizes the results of [23], derived for the Fibonacci lattice shifted by the phase $\varphi < 1$, to the quasicrystal with arbitrary d , Δ and t .

The one-dimensional Fibonacci lattice, being one of the most studied quasicrystals, is determined by the substitution rule [2]

$$L \rightarrow LS, \quad S \rightarrow L. \quad (11)$$

The parameters of this structure are given by

$$\begin{aligned} t &= \tau \equiv (\sqrt{5} + 1)/2 \approx 1.618, \\ \Delta &= S_p - L_p, \quad \varphi = 0, \quad d = S_p + (L_p - S_p)/\tau. \end{aligned} \quad (12)$$

If the center of the first QW is chosen at the plane $z = 0$ then $z_0 = -S_p$. Here, the ratio L_p/S_p is arbitrary, so that for $L_p = S_p$ the structure becomes periodic [24] and, for L_p/S_p equal to the golden mean τ , it becomes the canonical Fibonacci chain [9]. In the noncanonical Fibonacci structures, this ratio is different from 1 and τ .

The resonant Bragg condition [9] is obtained by equalizing the double light wavevector at the exciton resonance frequency ω_0 to one of the diffraction vectors $G_{hh'}$ with a large value of the coefficient $|f_{hh'}|$. This condition is equivalent to

$$q(\omega_0)d = \pi \left(h + \frac{h'}{\tau} \right), \quad (13)$$

where $q(\omega_0)$ is the light wavevector at the excitonic resonance frequency.

It is important to notice that the Bragg condition Eq. (13) is written for the structure without the nontrivial QW dispersion and without the structured dielectric QW environment that will modify the Bragg condition, in analogy with the case of the periodic QWs [25]. In realistic samples, several different layers are grown in between the active QW material layers such as, e.g., barrier layers, adjuster layers, and spacer layers. According to the different refractive indices of the respective materials, it is impossible to present a rigorous analytical generalization of Eq. (13), taking into account the effects of various layers and the QW dispersion. Instead, we use the concept of optical pathlength of layers defined as the products of the physical layer widths and their indices of refraction. Hence, we will always refer to the vacuum wavelength λ and treat the quantity $q(\omega_0)d$ in Eq. (13) as the product of the vacuum light wavevector at the excitation resonance frequency $q(\omega_0) = \omega_0/c \equiv 2\pi/\lambda$ and the average optical path D . The value of D is determined similar to Eq. (12), so that $D = S_0 + (L_0 - S_0)/\tau$. Now, S_0 and L_0 are determined as the optical path lengths from the center of one QW to the center of the next-neighboring one. In Sec. 5, we will demonstrate that the exact Bragg condition can be slightly different from that given by Eq. (13) due to the effects of the QW dispersion.

We stress that the set of the diffraction vectors is independent of the ratio $\rho = L_0/S_0$, see Eq. (9), and is the same both for canonical and noncanonical Fibonacci MQWs with the equal mean period D . In the case when $\rho = 1$, Eq. (13) reproduces the well-known Bragg condition for periodic structures. For the periodic resonant Bragg spacings, there is a series of spacer thicknesses which fulfill the Bragg condition, namely integer multiples of half the resonance wavelength [24, 26]. For the canonical Fibonacci structures, the $f(q)$ resonances, see Eq. (8), have largest values of $|f_{hh}| \approx 1$, which corresponds to h and h' equal to the subsequent Fibonacci numbers: $(h, h') = (F_j, F_{j-1})$. For the noncanonical structures, the coefficients $|f_{hh}|$ are maximal when the ratio of h'/h is close to $L_0/S_0 = 1$, as one can see from the analysis of Eqs. (10) and (12). For comparison, the first three sets of spacers are shown in Table 1 for the resonant periodic Bragg spacing ($\rho = 1$) and for the resonant canonical Fibonacci spacing ($\rho = \tau$).

Table 1. Comparison of spacers for periodic Bragg spacing ($\rho = 1$) and canonical Fibonacci spacing ($\rho = \tau$) for the first three Bragg resonances, $j = 1, 2, 3$.

overview of spacers for first 3 Bragg resonances						
	periodic Bragg, $\rho = 1$			Fibonacci, $\rho = \tau$		
j	D/λ	S_0/λ	L_0/λ	D/λ	S_0/λ	L_0/λ
1	0.5000	0.5000	0.5000	0.5000	0.3618	0.5854
2	1.0000	1.0000	1.0000	0.8090	0.5854	0.9472
3	1.5000	1.5000	1.5000	1.3090	0.9472	1.5326

3. Experimental and theoretical approaches

The samples FIB10, containing a single GaAs/AlGaAs QW, and FIB13, containing 54 Fibonacci-spaced GaAs/AlGaAs QWs, were grown by MBE on a (001) GaAs substrate [10]. The sample FIB13 corresponds to the canonical Fibonacci spacing with $\rho = \tau$ and $j = 1$, see Table 1. A schematic of the experimental apparatus is shown in Fig. 1. What is referred to as Fibonacci-spaced sequence of QWs can have any number N of QWs. Computations show that nothing special occurs for N equal to a Fibonacci number, i.e., all measurable quantities vary

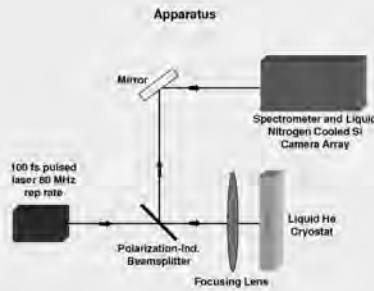


Fig. 1. Experimental setup

slowly as N passes through a Fibonacci number. FIB13 with $N = 54$ is, of course, one short of a Fibonacci number of QWs. The data are taken in a single-beam reflection geometry using the 100fs output pulse from an 80-MHz modelocked Ti:sapphire laser. The sample is mounted in a liquid-helium cryostat and maintained close to 4K. The use of a polarization-independent beam splitter sends the entire reflected signal to a spectrometer and CCD camera. The illuminated spot on the sample is approximately 7 microns in diameter. Typical integration times for the data presented below are 0.1 second. Even though a single beam is employed, when the pulse spectrum is centered above the continuum band-edge the experiment is equivalent to an above-band pump and resonant-probe experiment, as shown below.

To explain the experimental observations with a microscopic theory, we solve the self-consistent coupling between the macroscopic QW polarization P and the wave equation. More specifically, we evaluate the linear optical response from the semiconductor Bloch equations [27, 28] in steady state with constant carrier densities. The approach fully describes the microscopic polarization $P_{\mathbf{k}_i}$, for all relevant carrier momenta \mathbf{k}_i , and its dynamics influenced by the phase-space filling, the Coulomb renormalizations to the Rabi as well as to the single-particle energies, and the Coulomb-induced two-particle correlations. These correlations are systematically treated with the so-called cluster-expansion approach up to the two-particle scattering level [29]. As a result, our analysis also includes a microscopic description of screening effects as well as the Coulomb-induced scattering of polarization that yields excitation-induced dephasing and energy renormalizations to the excitonic resonances.

The semiconductor Bloch equations produce the linear QW response, i.e., the QW susceptibility

$$\chi(\omega) = \frac{P(\omega)}{\epsilon_0 E(\omega)}, \quad P(\omega) = \frac{d_{cv}}{\mathcal{V}} \sum_{\mathbf{k}_i} P_{\mathbf{k}_i}(\omega), \quad (14)$$

where $E(\omega)$ is the Fourier transform of the field that excites the QW. The macroscopic polarization is a sum over $P_{\mathbf{k}_i}$, scaled by the dipole-matrix element d_{cv} and the quantization area \mathcal{V} . In general, $\chi(\omega)$ is defined completely by the internal properties of the QW, i.e., $\chi(\omega)$ is the same for each QW and it is not influenced by other QWs or by the radiative environment.

The self-consistent coupling between the QWs and the light follows after we solve the semiconductor Bloch equations together with the Maxwell's equations. Thus, one needs to propagate light through the experimental structure where each dielectric layer and each QW is accounted for. For the linear response, this can be performed using the so-called transfer-matrix approach

[30, 31] where the optical response of each layer is included via its refractive index while each QW is described through $\chi(\omega)$. As a result of the self-consistent coupling, also the radiative dephasing of the QW polarization is described microscopically. Altogether, the SQW sample contains ten and the 54 QW sample contains 275 dielectric layers which are all included in the analysis; see Table 2 for the layer thicknesses and refractive indices used in the transfer matrix computations.

Table 2. Layer widths and refractive indices used in the analysis of the samples. The sample FIB10 contains only “cap” and “buffer and substrate” layers while the sample FIB13 contains additional “large spacer” and “small spacer” layers, producing a Fibonacci-spaced chain of QWs. The layers in both samples can be categorized into seven types. The refractive indices of only four layer types (indicated by a *) out of these seven were changed to match theory with experiment. The barriers are $\text{Al}_{0.5}\text{Ga}_{0.7}\text{As}$, the spacers are $\text{Al}_{0.04}\text{Ga}_{0.96}\text{As}$, the QWs and adjuster are GaAs; and the AlAs/GaAs SL is a six times repetition of 2 nm AlAs followed by 2 nm GaAs.

type	layer	width [nm]		refractive index n	group
		FIB10	FIB13		
	vacuum	∞	∞	1.000	
7*	GaAs cap	6.357	7.713	3.634	cap
3	spacer	90.823	89.537	3.589	
5	barrier	4.874	4.805	3.406	
6*	QW	22.490	22.174	3.642	
5	barrier	—	4.805	3.406	large spacer
4*	adjuster	—	1.928	3.271	
3	spacer	—	100.07	3.589	
5	barrier	—	4.805	3.406	
6*	QW	—	22.174	3.642	
5	barrier	—	4.805	3.406	small spacer
4*	adjuster	—	2.410	3.271	
3	spacer	—	47.402	3.589	
5	barrier	—	4.805	3.406	
6*	QW	—	22.174	3.642	
5	barrier	4.874	4.805	3.406	buffer and substrate
4*	adjuster	2.445	2.410	3.271	
3	spacer	90.823	47.402	3.589	
1*	GaAs	296.31	292.11	$3.634 + i0.07$	
2	AlAs/GaAs SL	22.62	22.32	3.310	
1*	GaAs substrate and buffer	∞	∞	$3.634 + i0.07$	

Besides the excitation induced dephasing effects, the excitonic resonances in the experimen-

ally realized samples are additionally broadened via excitation-level-independent disorder as well as phonon scattering. These are modeled by adding a frequency-dependent dephasing

$$\gamma_{\text{bg}}(\omega) = \frac{\gamma_{\text{bg}}}{\exp(-(\hbar\omega - E_x + \Delta E_{\text{cut}})/C) + 1} \quad (15)$$

that enters as the background dephasing constant to the semiconductor Bloch equations. The appearing constants are matched by comparing the full computation with the single-QW experiment. Figure 2(a) shows that the experimental (shaded area) and the theory (solid line) reflection spectra agree when we use $\gamma_{\text{bg}} = 0.163\text{meV}$ (0.110meV) for the heavy hole (light-hole) $1s$ resonance, positioned at E_x . The cut-off energy is set to $\Delta E_{\text{cut}} = 0.25\text{meV}$ and the constant is chosen to be $C = 0.1\text{meV}$. In addition, the heavy-hole and the light-hole dipole matrix elements are defined from a separate bandstructure calculation giving $d_{vc} = 0.78e\text{nm}$ and $d_{vc} = 0.5e\text{nm}$, respectively. The refractive indices are fitted using a single small set of parameters such that the calculations match the measured linear SQW and 54QW reflectance, respectively.

To check the quality of the parameter choices, we use exactly the same material inputs to compute the optical properties of the complicated sample. Figure 2(b) presents the calculated (solid line) and the measured (shaded area) reflection for the 54 Fibonacci-spaced QWs. Due to the Fibonacci spacing, the spectrum displays multiple features which all are very well reproduced by the theory. The best match between the experiment and theory is found using an average QW spacing of $D_0 = 0.5016\lambda$ and a ratio of large spacing to small spacing of $\rho_0 = 1.643$. In our further analysis, we are particularly interested in the deep dip below the hh $1s$ resonance (vertical dashed line).

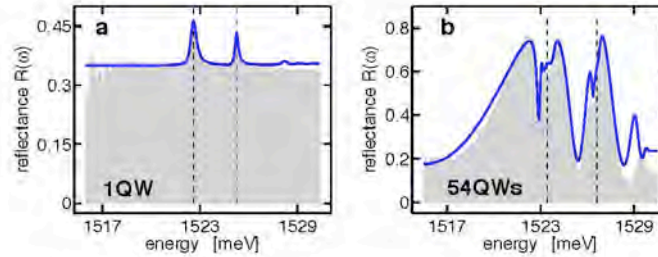


Fig. 2. Linear fits (blue line) to measured data (shaded area) for (a) a single QW (FIB10) and (b) for 54 Fibonacci-spaced QWs (FIB13) using a frequency-dependent dephasing $\gamma(\omega)$ and identical fit parameters. For both samples, theory and experiment agree excellently.

4. Nonlinear reflectivity of canonical Fibonacci quantum wells

Based on the parameter assignment of the linear evaluations, we proceed to analyze nonlinear experiments. Assuming 40K carrier distributions in thermodynamic quasi-equilibrium, we obtain the experiment-theory comparison shown in Fig. 3. For densities $n = 1 \times 10^9\text{cm}^{-2}$ (shaded area), $n = 5 \times 10^9\text{cm}^{-2}$ (red line), $n = 2 \times 10^{10}\text{cm}^{-2}$ (blue line), and $n = 5 \times 10^{10}\text{cm}^{-2}$ (black line), the computed nonlinear reflectance $R(\omega)$ of the 54QW sample is shown (a) which is in very good agreement with the nonlinear experimental results (b) obtained with pump powers of $76.6\mu\text{W}$ (shaded area), $871\mu\text{W}$ (red line), 3.7mW (blue line), and 11.1mW (black line). The real part (c) and the imaginary part (d) of the computed QW susceptibility are shown for the

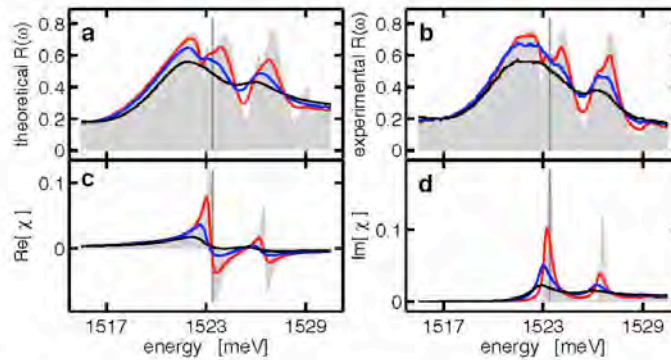


Fig. 3. Very good agreement between (a) computed and (b) experimental nonlinear reflectance is obtained for FIB13. Theory used densities $n = 1 \times 10^9 \text{ cm}^{-2}$ (shaded area), $n = 5 \times 10^9 \text{ cm}^{-2}$ (red line), $n = 2 \times 10^{10} \text{ cm}^{-2}$ (blue line), and $n = 5 \times 10^{10} \text{ cm}^{-2}$ (black line) while in the experiment the pump power was $P = 76.6 \mu\text{W}$ (shaded area), $P = 871 \mu\text{W}$ (red line), $P = 3.7 \text{ mW}$ (blue line), $P = 11.1 \text{ mW}$ (black line). An average spacing of $D_0 = 0.5016\lambda$ is deduced from the fit parameters. The real part (c) and the imaginary part of the corresponding computed susceptibilities (d) show broadening and bleaching with elevated carrier densities.

different densities. The excitation-induced dephasing leads to a bleaching and broadening of the susceptibility with increasing carrier density.

In particular, the pronounced dip below the hh 1s resonance (vertical line) gradually disappears from $R(\omega)$ (frames (a) and (b)) for elevated excitations. We also see that the reflection stopband becomes smeared out for the largest excitations. The corresponding computed nonlinear true absorption probabilities $A(\omega)$ are plotted in Fig. 4(a) (solid lines) together with the experimentally applied pulses (shaded areas, scaled). The actual true absorption, Fig. 4(b), is gained by multiplication of the pulse spectrum with the respective absorption probability. The resonant excitation as well as the above-band excitation shows considerable absorption in a wide spectral range. Accordingly, the nonlinear reflectance obtained with on-resonance or with above-resonance excitation look very much the same, compare Fig. 3(b) with Fig. 4(c), which explains the match of experimental resonant-pump data and pump-probe-like calculated spectra, c.f. Fig. 3(a) and (b).

Why is there such good agreement between experimental data and the theoretical computations? The analysis of many pulsed nonlinear experiments of quantum wells in the past have led to the conclusion that near band edge absorption of a 100 fs pulse results in carriers that can be quite adequately described by an equilibrium carrier distribution with temperature of 40-50K with negligible cooling or redistribution occurring within 100 fs. The nonresonant excitation can thus be characterized by a single parameter (the carrier density); it does not introduce any coherent polarizations in the quantum well. The density-dependent quantum-well nonlinearities are computed fully microscopically [27, 28, 29]. Using these individual quantum-well results, the reflection or transmission of a resonant probe incident normal to the multiple-quantum-well structure is then computed by the well known transfer matrix technique giving the effects of propagation through the complete structure. As the carrier density is increased the dominant

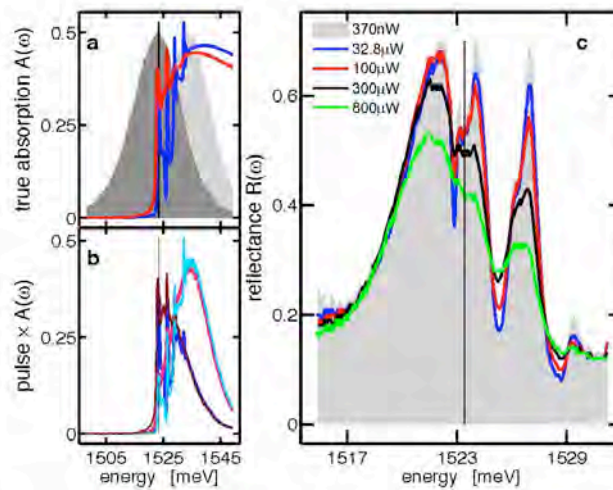


Fig. 4. The spectra of the experimentally applied pulses (shaded areas) are shown together with the computed absorption probability in frame (a) for low (blue line) and high (red line) excitation. The corresponding true absorption (b) is plotted for on-resonance and above-resonance excitation, showing that in both cases most of the absorption generates free carriers. Nonlinear reflectances obtained by above-band pumps are shown in frame (c). The spectra look very similar to those obtained by pumping resonantly.

carrier dependent nonlinearity is the so called excitation dependent dephasing, basically the increased relaxation of the probe induced polarization due to carrier collisions. As a result any narrow spectral features, such as the sharp dip here, are broadened and disappear as the carrier density is increased. In the experiment just described with the peak of the pulse centered in the quantum well continuum, carriers are generated incoherently; their effect on narrow spectral features is monitored by the weak resonant part of the pulse, corresponding to the probe of the theory. Since the entire reflected beam is detected, there is an averaging over carrier densities; this is not much of a problem either since the broadening changes relatively slowly with density. Clearly the qualitative behavior with increased excitation power is reproduced by the theory, and a detailed comparison of exact carrier densities seems unwarranted.

5. Linear reflectivity: origin of sharp dip and sensitivity to D and ρ

Based on the very good agreement of linear and nonlinear theoretical and experimental results, we now use our theory to investigate the origin of different spectral properties in more detail. Figure 5 shows results obtained from a switch-off analysis where spectra calculated with the same QW susceptibility as used in the previous investigations (shaded area) are compared to identical simulations except that either the real part of the QW susceptibility (blue line), or its imaginary part (red line), or the whole QW susceptibility χ (black line) is set to zero. It can clearly be seen that the main spectral features, such as the narrow deep dip close to the hh-resonance position (vertical line) as well as the valley between the hh- and the lh-resonance

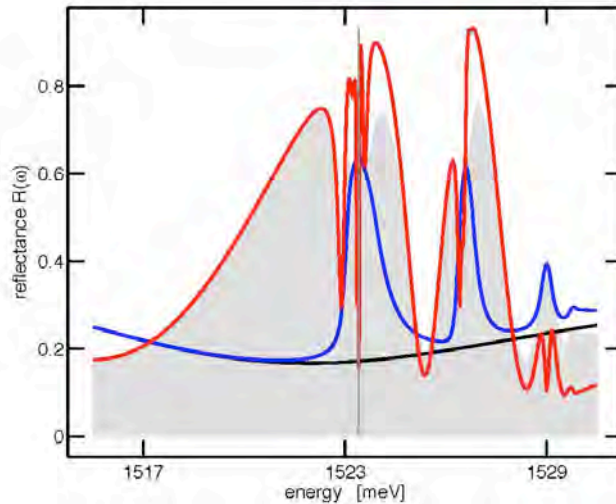


Fig. 5. Calculated reflectance spectra using the full QW susceptibility (shaded area) and with the real part (blue line), imaginary part (red line), or total susceptibility (black line) set to zero. Fine structures are introduced by the real part of the susceptibility while the imaginary part makes them partially vanish again.

position, result from $\text{Re}[\chi]$. Thus, they stem from cavity-like effects. While $\text{Re}[\chi]$ alone produces almost the correct spectral shape as well as a number of additional sharp peaks and dips, $\text{Im}[\chi]$ alone simply leads to absorption peaks at the respective $1s$ -resonance positions. In the full computation, $\text{Im}[\chi]$ leads to a smearing out of some of the sharp features.

A sharp spectral feature is a possible candidate for a high-speed optical switch because the reflectivity could be changed from a low to a high value in a very short time by shifting the entire spectrum, for example by the optical Stark effect [32]. It also has potential applications to slow light as explored for the interference fringes that occur within the spectral stopband of a very large number of slightly detuned excitonic Bragg periodic quantum wells [33, 34]. Similar slow light studies have also been made in a waveguide with periodic side coupling to resonators [35, 36].

To address the influence of the Fibonacci spacing on the spectral features, we vary either the average spacing D while the ratio of the two spacers, $\rho = L_a/S_a$, is kept constant, or we vary ρ while D is kept constant. The dependence of the spectrum on a variation of D or ρ is investigated in Fig. 6 for 54 QWs using the lowest density $n = 1 \times 10^9 \text{ cm}^{-2}$. To quantify the deviation between the computed reflection spectrum $R(\omega)$ and the original Fibonacci $R_0(\omega)$ in Fig. 3(a), we evaluate

$$\varepsilon = \frac{\int_{\omega_{1,99}-\Delta}^{\omega_{1,100}+\Delta} |R(\omega) - R_0(\omega)| d\omega}{\int_{\omega_{1,99}-\Delta}^{\omega_{1,100}+\Delta} R_0(\omega) d\omega} \quad (16)$$

where $\hbar\omega_{1,100} = 1523.4 \text{ meV}$ and $\hbar\Delta = 1.5 \text{ meV}$. The computed ε is shown in Fig. 6(a) as a

function of D when ρ is fixed to be $\rho_0 = 1.643$. We observe that the spectrum is very sensitive to the average spacing because varying D within $\pm 1\%$ already results in 25% changes. The strong dependence of the spectral shape on the average spacing can easily be understood based on the generalized Bragg condition, Eq. (13). Since the resonant Bragg condition defines a corresponding average spacing, it is obvious that the spectrum should have this strong dependence on D . In particular, the deep dip is present in the spectra within a narrow range from $D = 0.500\lambda$ ($D = 0.501\lambda$) up to $D = 0.503\lambda$ ($D = 0.503\lambda$) for the Fibonacci (periodic) spacing. We also have investigated the ε deviation when the ratio of the spacer widths is changed while the average spacing $D_0 = 0.5016\lambda$ is kept constant. Figure 6(b) shows that ε changes only very little as a function of ρ . In particular, we have changed ρ/ρ_0 almost an order of magnitude more than D/D_0 in Fig. 6(a) and get an ε deviation of only few percents, in contrast to the strong D dependence. Thus the Fibonacci features present a certain robustness of the spectrum to variations in ρ .

The effect of stronger variations of ρ can be seen in Fig. 7(a) which shows the reflectance of a sweep of ρ for the first Bragg resonance, i.e. $j = 1$ with $(h, h') = (F_1, F_0) = (1, 0)$. The ratio $\rho = L_o/S_o$ is tuned from the well-known [14] periodic case, $\rho = 1$, towards the canonical Fibonacci spacing, $\rho = \tau$, as well as to even larger values of ρ while the average spacing $D_0 = 0.5016\lambda$ is kept constant. The reflection maximum is observed for the periodic case, $\rho = 1$, which is due to the best constructive interference, $D_0 = S_o = L_o$. Accordingly, the reflection gets lower and lower the further the large and small spacers differ from each other. This is in agreement with the behavior of the corresponding structure factor $f(q)$, presented in Fig. 8. The strongest (narrowest and deepest) dip is found for $\rho = \tau$.

In contrast to the first Bragg resonance, the structure factor of the second Bragg resonance, i.e. $j = 2$ with $(h, h') = (F_2, F_1)$, has an average spacing of $D_{j=2} = \tau\lambda/2 = 0.8090\lambda$. Thus, the fully periodic situation, $\rho = 1$, yields equal $L_o = S_o = D_{j=2} = 0.8090\lambda$, which produces a destructive interference in reflection because the coupled QWs are separated by irrational fractions of λ , unlike for the first Bragg condition. According to Fig. 8, the structure factor f vanishes at $\rho = 1$, which shows that the destructive interference is complete. When ρ is increased to two, the short intervals have a distance $S_o = D/\tau = \lambda/2$ such that the large interval

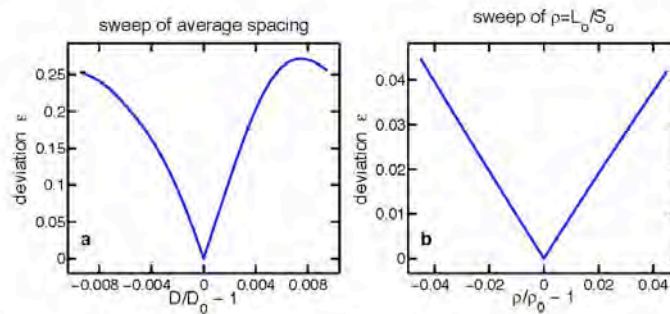


Fig. 6. Deviations of 54QW reflectance spectra from the fit spectrum ($D_0 = 0.5016\lambda$ and $\rho_0 = 1.643$) are shown in dependence of (a) the average distance D and (b) the ratio of layer thicknesses $\rho = L_o/S_o$. A strong dependence on D is found while a certain robustness against changes in ρ is observed.

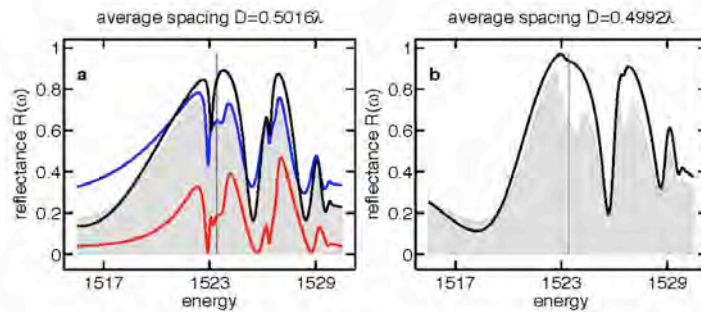


Fig. 9 Reflectance for 54QWs: (a) computations with parameters according to FIB13 (shaded area), FIB13 with ARC (red line), constant refractive index everywhere but same optical lengths as FIB13 (blue line), and optical-length periodic spacing (black line) with same average spacing $D = 0.5016\lambda$ as FIB13. Obtaining the dip in all spectra suggests the dip to be caused by the uniform average spacing. (b) For $D = 0.4992\lambda$, there is no dip in the spectrum of periodically spaced 54QWs (black line) while there is one for Fibonacci-spaced QWs (area).

structure much. Consequently, the dip must be caused by the QW arrangement, not by interference effects due to the dielectric environment of the QWs. We have additionally studied 54 periodically spaced QWs in Fig. 9(a) (black line). Even this case displays a strong dip below the 1s hh resonance (vertical line). That dip follows from the non-ideal average spacing detuned slightly away from $\lambda/2$.

To check the effect of negative detuning, we compute $R(\omega)$ using $D = 0.4992\lambda$ that is tuned slightly below $\lambda/2$. In case of periodic spacing (black line), $R(\omega)$ does not have any dip in contrast to the Fibonacci spacing (shaded area), as shown in Fig. 9(b). In particular, the difference of the reflectivity in the dip minimum and the reflectivity maximum next to the dip became only slightly smaller due to the different average spacing. Therefore, one may conclude that the dip in Fig. 9(a) is primarily caused by the average spacing differing from the ideal $\lambda/2$ value. Nonetheless, the Fibonacci spacing leads to the formation of a dip as well due to the quasi-periodic nature. As a result of the interplay of these two effects, the Fibonacci spacing produces a narrower and deeper dip than the one obtained in the periodic structure, c.f. Figs. 7 and 9.

As a last point, we investigate how the QW number influences the dip and the resonance structures. Otherwise, we use the parameters corresponding to the sample FIB13 in our computations and present $R(\omega)$ as a function of the QW number in Fig. 10. We observe that the spectrum yields only a peak for small QW numbers. With increasing QW number, the dip emerges at an energetic position slightly below the 1s heavy-hole resonance (vertical line). With further increasing QW number, this peak shifts to lower energies and gets broader while additional dips emerge from the wiggles which one can observe near the hh resonance. These additional dips behave analogously to the first dip. This behavior is found for all Fibonacci-spaced sample types treated in Fig. 9(a) such that it has to be attributed to the QW spacing as well.

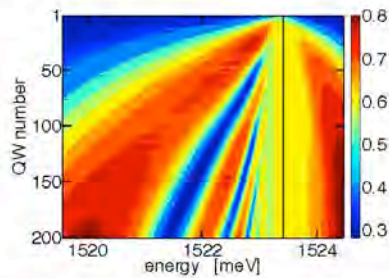


Fig. 10. Reflectance close to the 1s-bh-resonance position as a function of QW number and energy for parameters according to FIB13.

6. Conclusion

In conclusion, we have presented reflectance measurements on one-dimensional quasicrystals realized in the form of Fibonacci-spaced QWs and applied our microscopic theory to reproduce and understand these spectra. The linear spectra exhibit a pronounced dip in the center of the Bragg-resonance reflectivity stopband. The analysis shows this dip to be a consequence of the real part of the excitonic resonance susceptibility (index effects), it is not caused by interference effects due to the dielectric environment of the QWs. For elevated carrier densities, the dip bleaches due to excitation-induced dephasing. Moreover, the dip is very sensitive to the average QW spacing, D , and shows a certain robustness for variations of the ratio of the spacer widths around the golden mean while it disappears if that ratio is changed too much. With increasing QW number, the dip gets broader and shifts to lower energies. At the same time, additional dips with similar behavior emerge close to the Bragg resonance position.

Acknowledgments

The Marburg group acknowledges support from the Deutsche Forschungsgemeinschaft and AFOSR grant FA9550-07-1-0010 sponsoring the visits of SWK in Tucson/AZ. The Tucson group thanks AFOSR, NSF AMOP and EPDT, NSF ERC CIAN, and JOSP for support. The St. Petersburg work was supported by RFBR and the "Dynasty" Foundation – ICFPM. M. Wegener acknowledges financial support provided by the Deutsche Forschungsgemeinschaft (DFG) and the State of Baden-Württemberg through the DFG-Center for Functional Nanostructures (CFN) within subproject A1.4.

7 References

1. Peyghambarian, Nasser, 1954, S. W. (Stephan W.). Koch, and Andre Mysyrowicz. Introduction to Semiconductor Optics. Englewood Cliffs, N.J: Prentice Hall, 1993.
2. Haug, Hartmut, and S. W. (Stephan W.). Koch. Quantum Theory of the Optical and Electronic Properties of Semiconductors. 4th ed. River Edge, NJ; Singapore: World Scientific, 2004.
3. Cohen-Tannoudji, Claude, 1933, Bernard Diu, and Franck Laloë 1940. Quantum Mechanics. New York; Paris: Wiley, 2005.
4. Griffiths, David J. 1942- (David Jeffery). Introduction to Quantum Mechanics. 2nd ed. Upper Saddle River, N.J: Pearson Prentice Hall, 2005.
5. Kuo, C. P., et al. "Effect of Mismatch Strain on Band Gap in III-V Semiconductors." *Journal of Applied Physics* 58.12 (1985): 5428-32.
6. Meinzer, Nina, et al. "Arrays of Ag Split-Ring Resonators Coupled to InGaAs Single-Quantum-Well Gain." *Optics Express* 18.23 (2010): 24140-51.
7. Wakefield, B., et al. "Direct Energy Gap of Al_{1-x}In_xAs Lattice Matched to InP." *Applied Physics Letters* 75.3 (1984): 341-3.
8. Oertel, D., et al. "High-Precision Band-Gap Determination of Al_{0.48}In_{0.52}As with Optical and Structural Methods." *Applied Physics Letters* 75.2 (1989): 140-1.
9. Roura, P., et al. "Determination of the Direct Band-Gap Energy of InAlAs Matched to InP by Photoluminescence Excitation Spectroscopy." *Journal of Applied Physics* 104.10 (1997): 6916-20.
10. Richards, B. C., et al. "Progress in Growth, Fabrication, and Characterization of Semiconductor Photonic Crystal Nanocavities." *Physica Status Solidi (B) Basic Research* 248.4 (2011): 892-6..
11. Veselago, Viktor G. "the Electrodynamics of Substances with Simultaneously Negative Values of ϵ and μ ." *Soviet Physics Uspekhi* 10 (1968): 509..
12. Soukoulis, C. M., M. Kafesaki, and E. N. Economou. "Negative-Index Materials: New Frontiers in Optics." *Advanced Materials* 18.15 (2006): 1941-52..
13. Smith, D. R. Padilla, Willie J, et al. "Composite Medium with Simultaneously Negative Permeability and Permittivity." *Physical Review Letters* 84.18 (2000): 4184-7.
14. Pendry, J. B. "Negative Refraction Makes a Perfect Lens." *Physical Review Letters* 85.18 (2000): 3966-9.
15. Linden, Stefan, et al. "Magnetic Response of Metamaterials at 100 Terahertz." *Science* 306.5700 (2004): 1351-3.
16. Enkrich, C., et al. "Magnetic Metamaterials at Telecommunication and Visible Frequencies." *Physical Review Letters* 95.20 (2005): 203901.

17. Linden, S., et al. "Photonic Metamaterials: Magnetism at Optical Frequencies." *IEEE Journal of Selected Topics in Quantum Electronics* 12.6 (2006): 1097-105.
18. E. M. Purcell "Spontaneous emission probabilities at radio frequencies" *Phys. Rev.* 69, 681 (1946)
19. Yablonovitch, Eli. "Inhibited Spontaneous Emission in Solid-State Physics and Electronics." *Physical Review Letters* 58.20 (1987): 2059-62.
20. McCray, W. Patrick. "MBE Deserves a Place in the History Books." *Nature Nanotechnology* 2.5 (2007): 259-61.
21. König, M., et al. "Distance-Dependence of the Coupling between Split-Ring Resonators and Single-Quantum-Well Gain." *Applied Physics Letters* 99.11 (2011): 111104,111104-3.
22. Enzmann, Roland, et al. "Design and Realization of Low Density InAs Quantum Dots on AlGaInAs Lattice Matched to InP(0 0 1)." *Journal of Crystal Growth* 312.16 (2010): 2300-4.
23. Franssila, Sami, and Inc ebrary. *Introduction to Microfabrication*. 2nd ed. Hoboken, NJ;Chichester, West Sussex, England,; John Wiley & Sons, 2010.
24. Mohammad, Mohammad Ali, et al. "Fundamentals of Electron Beam Exposure and Development." , 2014. 11-41.
25. Nina Meinzer. Coupling Plasmonic Metamaterials to Single Quantum Well Gain. Karlsruhe Germany, Karlsruhe Institute of Technology.
26. Milonni, Peter W., and J. H. Eberly 1935. *Laser Physics*. Hoboken, N.J: John Wiley & Sons, 2010.
27. Richards, Benjamin Colby. *1D and 2D Photonic Crystal Nanocavities for Semiconductor Cavity QED*. Tucson, Arizona: University of Arizona, 2011.
28. Khitrova, G., et al. "Vacuum Rabi Splitting with a Single Quantum Dot in a Photonic Crystal Nanocavity." *Nature* 432.7014 (2004): 200-3.
29. Khitrova, G., et al. "Nonlinear Optics of Normal-Mode-Coupling Semiconductor Microcavities." *Reviews of Modern Physics* 71.5 (1999): 1591-639.
30. Gérard, J. M., and B. Gayral. "InAs Quantum Dots: Artificial Atoms for Solid-State Cavity-Quantum Electrodynamics." *Physica E: Low-dimensional Systems and Nanostructures* 9.1 (2001): 131-9.
31. Sweet, J., et al. "GaAs Photonic Crystal Slab Nanocavities: Growth, Fabrication, and Quality Factor." *Photonics and Nanostructures - Fundamentals and Applications* 8.1 (2010): 1-6.
32. Khankhoje, U. K., et al. "Modelling and Fabrication of GaAs Photonic-Crystal Cavities for Cavity Quantum Electrodynamics." *Nanotechnology* 21.6 (2010): 065202.
33. Richards, B. C., et al. "Progress in Growth, Fabrication, and Characterization of Semiconductor Photonic Crystal Nanocavities." *Physica Status Solidi (B) Basic Research* 248.4 (2011): 892-6.

34. Hendrickson, J., et al. "Quantum Dot Photonic-Crystal-Slab Nanocavities: Quality Factors and Lasing." *Physical Review B - Condensed Matter and Materials Physics* 72.19 (2005).
35. Hendrickson, Joshua, et al. "InAs Quantum Dot Site-Selective Growth on GaAs Substrates." *Physica Status Solidi (C) Current Topics in Solid State Physics* 8.4 (2011): 1242-5.
36. Corrigan, T. D., et al. "Optical Plasmonic Resonances in Split-Ring Resonator Structures: An Improved LC Model." *Optics Express* 16.24 (2008): 19850-64.
37. Biagioni, Paolo, Jer-Shing Huang, and Bert Hecht. "Nanoantennas for Visible and Infrared Radiation." *Reports on Progress in Physics* 75.2 (2012;2011;).
38. Ploog, Klaus, and L. 1956- (Leander) Tapfer. *Physics and Technology of Semiconductor Quantum Devices: Proceedings of the International School Held in Mesagne (Brindisi), Italy, 21-26 September 1992*. 419;419.; Vol. New York;Berlin;: Springer-Verlag, 1993.
39. Wegener, Martin, et al. "Toy Model for Plasmonic Metamaterial Resonances Coupled to Two-Level System Gain." *Optics Express* 16.24 (2008): 19785-98.
40. Busch, K., et al. "Periodic Nanostructures for Photonics." *Physics Reports* 444.3 (2007): 101-202.